Wave physics in a tidal inlet

Part I:

On the time scales of wave processes

&

Part II:

Depth-induced breaking:

A comparison on the performance of three models

Paul van der Ham
1243896

Delft, July 2009

Prof. Dr. Ir. G.S. Stelling
Dr. Ir. L.H. Holthuijsen
Dr. Ir. G. Ph. Van Vledder
Ir. T.J. Zitman
Dr. A.J. Van der Westhuysen

Author:
Paul van der Ham
Waterhoenstraat 44
3312 RS Dordrecht

Graduation committee:
Prof. Dr. Ir. G. S. Stelling
Section Environmental Fluid Mechanics
Dr. Ir. L. H. Holthuijsen
Section Environmental Fluid Mechanics
Dr. Ir. G. Ph. Van Vledder
Section Environmental Fluid Mechanics
Ir. T. J. Zitman
Section Hydraulic Engineering
Dr. A.J. Van der Westhuysen
Deltares

'Die Veränderung ist eine Kraft die viel bewegt, doch in der Beständigkeit erreichen wir wahre Größe!'

(Menhir, Thüringen 2007)

Preface

Before you lies the result of my Master thesis. During my research I encountered, for me, major setbacks. These considerably prolonged the time I needed to finish this thesis. I started out my research on the subject of wave processes in the Amelander Zeegat. About halfway this study my supervisor Leo Holthuijsen, Marcel Zijlema and Nico Booij found errors in the source code of the SWAN version used for this study. Because of these errors all the results obtained so far were useless. However, new results were obtained shortly after the source code of the SWAN model had been corrected. The results of this research have been presented by my supervisor at the ICCE 2008 and have been published

After finishing this part my supervisor and I decided to enhance the first part with a study on depth-induced breaking in the Amelander Zeegat area. The goal of this study was to find a model that would give the best overall results for various test cases. However, about two months later during a meeting with my graduation committee, it became clear that this goal was already achieved by one of the members of my committee. This, however, gave us the opportunity to compare his model and various other models on other cases than the Waddenzee area.

The period after the meeting was a dark one for me, for I was seriously considering quitting my studies all together. It was very difficult to find the motivation to go on. Thankfully, after approximately two months, with a lot of help from my girlfriend, supervisor and fellow students, I pulled through and the result is part II of this thesis.

I would like to thank the section Environmental Fluid Mechanics for giving me my own place to work and for the support everyone gave

me. In particular my daily supervisor Leo Holthuijsen who has helped me a lot during the course of time. Also, I would like to thank Gerbrant van Vledder for his participation in my project and for his advice and critics. Furthermore, I would like to thank my fellow students Pieter Smit, Sijbrand Balkema, Matthijs Benit, Daniël Dusseljee, Anna Kroon, Jules Schmedding and Robin van Buchem, for their input, support and encouragement. Also, I would like to thank my family for their support. Especially, I would like to thank my girlfriend Renske who helped me a lot to find motivation to go on. Lastly, I want to thank my two pet cats Elbie and Tweeg who, somehow, always knew to cheer me up, no matter how dark my mood was.

Part I:

On the time scales of wave processes

Contents

Abstract

To systematically improve the SWAN model a study on the wave physics in a tidal inlet was carried out. The third-generation SWAN model was used to compute the wave processes in a tidal inlet for storm conditions. The computed wave processes are propagation (shoaling, refraction and frequency shifting), generation (wind input), non-linear wave-wave interactions (quadruplet wave-wave interactions and triad wave-wave interactions), dissipation (white capping, depth induced breaking and bottom friction), and the work done by the currents against the radiation stresses. The results were normalised, which resulted in the time scales of all wave processes. The time scales were of the order 100s – 1,000s, except for the work done by the currents against the radiation stresses, which is of the order of 1,000s – 10,000s. This research has been published in the *Proceedings of the 31st International Conference on Coastal Engineering*. Also, see appendix A.

List of symbols

Symbol	Description	Units
C_{bfr}	Bottom friction coefficient	$m^{2/}s^{3}$
C_{nl3}	Triad wave-wave interaction coefficient	
C_{nl4}	Quadruplet wave-wave interaction constant $\left(=3\cdot10^{7}\right)$	-
$C_{sh,i}$	Constants in scaling factor for quadruplet wave-wave interactions for $i=1,\ 2,\ 3$ $\left(C_{sh,1}=5.5;C_{sh,2}=6/7;C_{sh,3}=-1.25\right)$	-
C_{wc}	Tuneable white capping coefficient	-
c	Wave celerity or phase speed	m/s
c_{g}	Group velocity	m/s
$c_{g,x}$	Group velocity in x-direction	m/s
$c_{g,y}$	Group velocity in y-direction	m/s
c_{σ}	Rate of change of the relative frequency	$1/s^{2}$
c_{θ}	Refraction- or diffraction-induced turning rate of the individual wave components	rad/s
$\overline{D}_{surf}$	Average dissipation of all waves	m^{2}/s
d	Water depth	m
E	Wave energy density	J/m^{2}
F	Spectral wave energy density	m^{2}/Hz
f	Wave frequency $\left(=1/T\right)$	Hz
$\overline{f}_{0}$	Mean zero crossing frequency	Hz
g	Gravitational acceleration (= 9.81)	m/s^{2}
H_{m0}	Significant wave height; determined with wave spectrum	m
$H_{\max}$	Maximum wave height	m
k	Wave number	$1/m$

$\tilde{k}$	Mean wave number	$1/m$
k_p	Peak wave number	$1/m$
L	Wave length	m
L_0	Deep water wave length	m
m_0	Zeroth order moment of the wave spectrum	m^2
m_n	n-th order moment of the wave spectrum	$m^2 s^{-n}$
N	Spectral wave action	$m^2 s$
N_{Ursell}	Ursell number	-
n	Ratio between group velocity and phase speed	-
p	Tuneable coefficient in white capping description	-
Q_b	Fraction of broken waves	-
R	Scaling factor for quadruplet wave-wave interaction $\left(R_{\max} = 4.43\right)$	-
S_{tot}	Sum of all source terms	$m^2/Hz/s$
S_{bfr}	Bottom friction source term	$m^2/Hz/s$
S_{diss}	Sum of all dissipative source terms	$m^2/Hz/s$
S_{in}	Wind input source term	$m^2/Hz/s$
S_{nl}	Sum of all non-linear wave-wave interaction terms	$m^2/Hz/s$
S_{nl3}	Triad wave-wave interaction source term	$m^2/Hz/s$
S_{nl4}	Quadruplet wave-wave interaction source term	$m^2/Hz/s$
S_{surf}	Depth induced wave breaking source term	$m^2/Hz/s$
S_{wc}	White capping source term	$m^2/Hz/s$
s	Wave steepness	-
$\tilde{s}$	Overall wave steepness	-
$\tilde{s}_{PM}$	Overall wave steepness Pierson-Moskowitz spectrum $\left(=\sqrt{3.02\cdot 10^{-3}}\right)$	-
T_1, T_2	Complex transfer coefficients in Boltzmann	-

	integral	
T_{m01}	Mean wave period	s
T_p	Peak wave period	s
U	Current velocity	m/s
U_{10}	Wind speed at 10m altitude	m/s
U_r	Ursell-number	-
U_α	Velocity in α-direction	m/s
U_β	Velocity in β-direction	m/s
$u_{rms,bottom}$	Root-mean-squared value of the orbital velocity at the bottom	m/s
u_*	Friction velocity of the wind	m/s
x	Distance along the horizontal axis	m
y	Distance along the vertical axis	m
α_{BJ}	Tuneable coefficient in the Battjes and Janssen bore-based model (= 1)	-
β	biphase	-
δ_{nl3}	Tuneable coefficient	-
δ_{wc}	Tuneable coefficient	-
$\delta_{\alpha\beta}$	Kronecker delta	-
Γ	Steepness coefficient	-
γ	Breaker index	-
γ_s	Ratio between the significant wave height and the water depth	-
λ	Constant coefficient (= 0.25)	-
ρ_{air}	Density of air	kg/m^3
ρ_{water}	Density of water	kg/m^3
σ	Radian frequency	$1/s$
$\tilde{\sigma}$	Mean frequency	$1/s$
σ^*_{PM}	Peak frequency of Pierson-Moskowitz spectrum reformulated in terms of friction velocity	$1/s$
τ_t	Timescale for the rate of change of spectral	s

	wave energy	
τ_x	Timescale for the rate of change of spectral wave energy in x-direction in the shoaling term	s
τ_y	Timescale for the rate of change of spectral wave energy in x-direction in the shoaling term	s
τ_σ	Timescale for the rate of change of spectral wave energy in frequency space	s
τ_θ	Timescale for the rate of change of spectral wave energy in directional space (refraction term)	s
θ	Wave direction	rad
θ_{wind}	Wind direction	rad
Φ_{xx}	Radiation stress component indicating transport of x-momentum in the x-direction per unit width per unit time	J/m^2
Φ_{xy}	Radiation stress component indicating transport of x-momentum in the y-direction per unit width per unit time	J/m^2
Φ_{yx}	Radiation stress component indicating transport of y-momentum in the x-direction per unit width per unit time	J/m^2
Φ_{yy}	Radiation stress component indicating transport of y-momentum in the y-direction per unit width per unit time	J/m^2
$\Phi_{\alpha\beta}$	Radiation stress component indicating transport of α-momentum in the β-direction per unit width per unit time	J/m^2

1 Introduction

Every five years the level of the present dikes of Friesland and Groningen needs to be assessed. In this assessment, based on the Hydraulic Boundary Conditions (HBC) and the Safety Assessment Regulation, water levels and several wave field parameters during a normative storm are used to determine the hydraulic loading on the dikes. In the calculation of the hydraulic loading, the significant wave height (H_{m0}) and the mean wave period (T_{m01}) are of great importance.

The prediction of the significant wave height is generally good but that of the wave period and of the spectrum is rather poor. Known problems in the SWAN model are the under prediction of the wave height in depth limited conditions, the over prediction of the wave height in opposing currents and the under estimation of the penetration of low-frequency wave (e.g. swell).

To improve the predictions, we want to know more about the wave conditions and development behind the barrier islands in storm conditions. Therefore, it is useful to better understand the different wave processes and their geographical distribution. With these geographical distributions it can be seen where each of the wave processes is strong or weak.

The method used to acquire the understanding of the wave processes contains calculations with the SWAN model, effectively working from a large coarse computational grid to an optimal, denser grid (see Chapter 4).

The aim of this study is to gain insight in the wave processes as well as their geographical distribution over the area of interest.

In this study the Amelander Zeegat is the area of interest. A description of this area, including an overview of the bathymetry and currents in the Amelander Zeegat for a particular storm will be given in Chapter 2. Chapter 3 deals with the governing equations used in this study and the derivation of the term that represents the work done by the ambient currents against the radiation stresses. Chapter 4 gives the outline of the model setup. In Chapter 5 the normalisation and the dimensions of the output data of the results are discussed. In Chapter 6 a selection of wave characteristics, which are useful for explaining the results in the discussion, is presented. The results and discussion are both presented in Chapter 7. Chapter 8 presents an overview of the conclusions of this study.

2 The Amelander Zeegat

2.1 Introduction

The Waddenzee is a very shallow shelf sea in the north of the Netherlands. Six islands of which five are inhabited enclose the Dutch part of the sea (the names of the islands are given in Figure 2-1). In between the islands are tidal inlets. Tidal inlets consist of the following major parts: tidal flats (behind the barrier islands), flood and ebb channels and the ebb tidal delta.
The depth varies greatly in these tidal inlets. The ebb channels are the deepest and the tidal flats are the shallowest. In the Amelander Zeegat these depths vary from approximately 25 m in the deepest channel to less than 1 m on the mud flats (see Figure 2-3).
The Amelander Zeegat is situated between the islands Terschelling and Ameland.

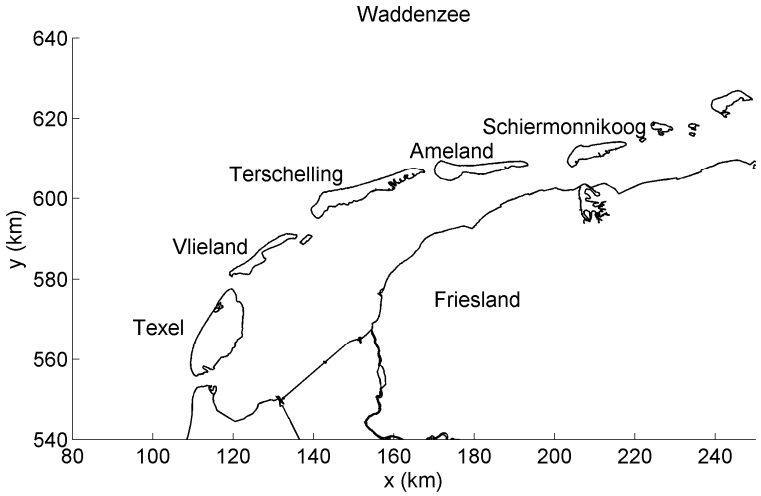

Figure 2-1 Waddenzee area

2.2 Bottom level characteristics

An overview of the bathymetry of the Waddenzee area is given in Figure 2-2. The Amelander Zeegat is encircled in Figure 2-2. The Amelander Zeegat, with its channels, and some of the channels of the tidal inlet in between Vlieland and Terschelling is given in Figure 2-3. The reference level for both figures is NAP.

Figure 2-2 Bathymetry of the Waddenzee. The Amelander Zeegat is encircled

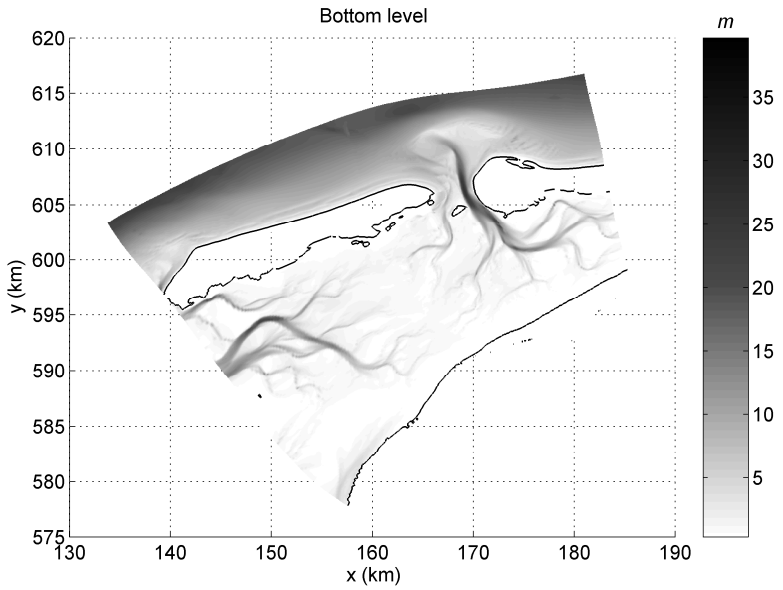

Figure 2-3 Bathymetry of the Amelander Zeegat

The orientation of the main channel is from north to south and bends to the east further into the Waddenzee. Interesting features of the bathymetry are the existence of sand waves at the eastern side of the ebb tidal delta and the long bars in front of Terschelling, shown in Figure 2-4. These features might significantly affect the wave processes in the Amelander Zeegat, which will be discussed later.

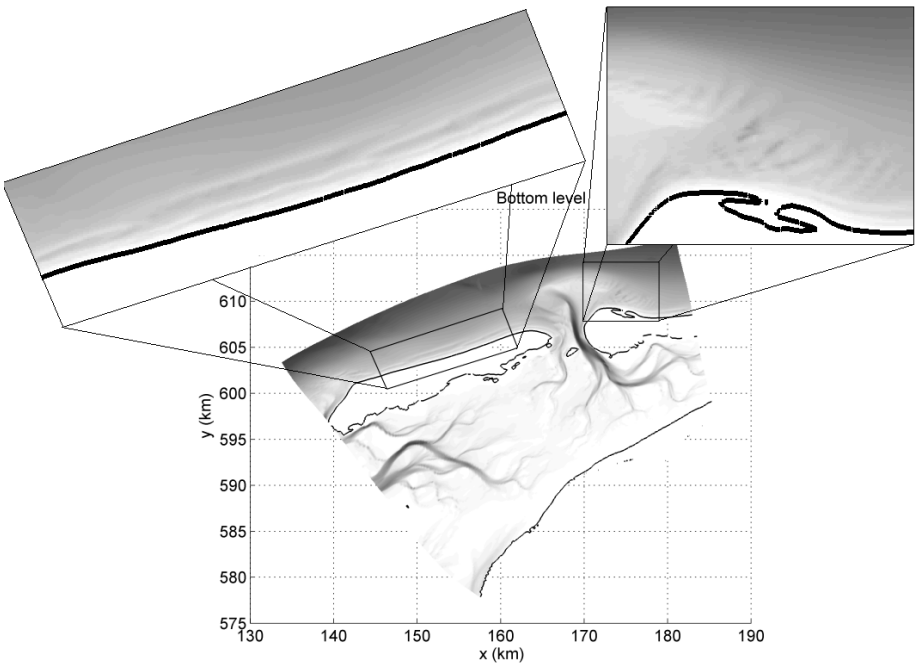

Figure 2-4 Sand waves (Ameland) and sand bars (Terschelling)

2.3 Currents

As mentioned above, the local tidal currents give the inlet its characteristic shape. Figure 2-5 shows the situation during flood tide (the arrows indicate the flow direction and flow velocity) for a specific storm situation with wave field parameters $H_{m0} = 6\,\mathrm{m}$, $T_p = 12\,\mathrm{s}$, $U_{10} = 15\,\mathrm{m/s}$ from the north. In which the significant wave height is defined as:

$$H_{m0} \approx 4\sqrt{m_0} \tag{2.1}$$

The situation presented in Figure 2-5 illustrates the current velocities in a storm, observed at 8 February 2004 at 20h00. This normative storm has a return period of about a year. The highest flow velocity

is approximately 2.2 m/s in the main channel. The lowest velocities are on the flats. The wantij-area (where there are no currents) stretches out from Terschelling to the mainland, in the map from approximately halfway along the southern coastline of Terschelling to Frisian mainland.

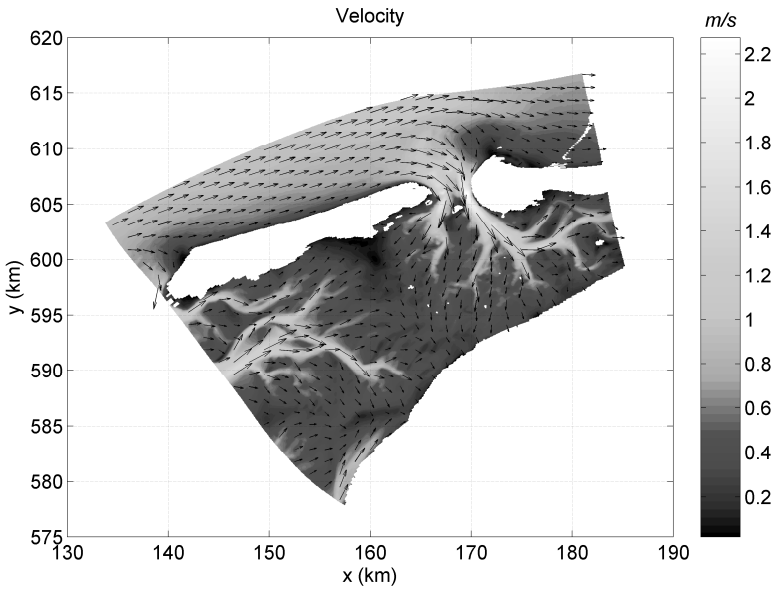

Figure 2-5 Current velocities during flood tide during normative storm at 8 February 2004 20h00. The arrows indicate the current direction and velocity.

3 Wave Physics

3.1 Introduction

3.1.1 First-, second- and third-generation wave models[1]

Wave modelling and prediction were well known at the beginning of the 1960s. However, none of the models developed in the 1960s and 1970s used a full energy balance equation to compute the wave spectrum. In these models assumptions on the shape of the spectrum and its development were made. One of these assumptions was the one-dimensional saturation spectrum (Phillips, 1958). The reasons for these assumptions were the lack of computer power and the underestimation of the importance of the non-linear wave-wave interactions in wave evolution. Wave models that are based on these assumptions are called first-generation wave models.

The relative importance of nonlinear transfer and wind input became more apparent after numerous wave growth experiments and direct measurements of the wind input to the waves. This resulted in the development of the second-generation wave models. Taken into account in these second-generation models are the non-linear wave-wave interactions, the 'overshoot' phenomenon and the dependence of the high-frequency region of the spectrum on the low frequencies. However, the spectral shape still has to be imposed (i.e. for wind-sea), which results in computing the parameters of this spectrum only, whereas the rest of the spectrum (i.e. swell) only needs to propagate in the model.

[1] See also Janssen 2003, and for additional historical perspective on SWAMP, see Komen 2004.

In the SWAMP (1985) Sea WAve Model intercomparison Project a distinction was made between first generation models and second generation models. From SWAMP it was also concluded that the knowledge of the spectral behaviour was lacking. The observed wave spectra showed much more variability than was originally assumed in parametric models and two-dimensional aspects were found to be more important than expected. For this reason a third-generation model was developed. A third-generation model is a full spectral model in which the physical processes were represented explicitly. Also a full two-dimensional description of the sea state is given. The most important difference between second- and third-generation wave models is that the latter have an explicit description of the non-linear wave-wave interactions. In the third-generation models the wave spectrum is computed by integration of the energy balance equation, without any spectral shape imposed a priori. Examples of third-generation wave models are the WAM model and the SWAN model.

3.1.2 The WAM model

The WAM (WAve Modelling) model was developed by the WAMDI (WAve Modelling Development and Implementation) group in the 1980s. The WAM model calculates the wave field by solving the spectral energy balance equation for the two-dimensional wave spectrum. The WAM model has had several updates, called cycles. The original version was called WAM cycle 1 and was updated to WAM cycle 2, 3 and 4.

3.1.3 The SWAN model

The SWAN model (Booij et al.,1999), Simulating WAves Nearshore, calculates short-crested, wind-generated waves in oceanic waters, coastal regions and inland waters. It is especially designed for shallow

water regions. It can therefore be linked to models that compute deep water regions, for example the WAM model. The SWAN model philosophy is very similar to that of the WAM cycle 3 model. The descriptions for the deep water wave processes (wind input, white capping and nonlinear wave-wave interactions) are identical to that of the WAM model. In addition the SWAN model describes the shallow water wave processes (bottom friction, depth-induced breaking and triad wave-wave interactions).
The SWAN model also had several updates, the version used here is SWAN cycle III 40.72.

Both the WAM and SWAN model are third-generation models, but they do have differences. The WAM model does not have a source term for the triad wave-wave interaction and for the depth-induced breaking, whereas the SWAN model does.
Another difference is in the numeric solving of the energy balance equation. The WAM model solves the energy balance equation explicitly, which means there is a stability condition. The SWAN model on the other hand solves the energy balance equation implicitly and therefore is unbound by the stability condition. For this reason the WAM model is not very useful in coastal regions.

3.2 The energy balance equation

An important concept in wave modelling is the spectral energy balance equation (Gelci, Cazalé and Vassal, 1957). This concept is based on an Eulerian approach involving numerous calculations at a large number of locations, all with a local energy balance. For

application to shallow water, the spectral energy balance equation is given by:

$$\frac{\partial F(f,\theta;x,y,t)}{\partial t} + \frac{\partial c_{g,x} F(f,\theta;x,y,t)}{\partial x} + \frac{\partial c_{g,y} F(f,\theta;x,y,t)}{\partial y} + \ldots \\ \ldots \frac{\partial c_{\theta} F(f,\theta;x,y,t)}{\partial \theta} = S(f,\theta;x,y,t) \tag{3.1}$$

When ambient currents are taken into account, terms representing the energy transfer between the waves and currents and the effects on the propagation of waves have to be added. This can be achieved by considering action density $\left(N(\sigma,\theta) = F(\sigma,\theta)/\sigma\right)$. The resulting spectral action density balance equation is given by:

$$\frac{\partial N(\sigma,\theta;x,y,t)}{\partial t} + \frac{\partial c_{g,x} N(\sigma,\theta;x,y,t)}{\partial x} + \frac{\partial c_{g,y} N(\sigma,\theta;x,y,t)}{\partial y} + \ldots \\ \ldots \frac{\partial c_{\theta} N(\sigma,\theta;x,y,t)}{\partial \theta} + \frac{\partial c_{\sigma} N(\sigma,\theta;x,y,t)}{\partial \sigma} = \frac{S(\sigma,\theta;x,y,t)}{\sigma} \tag{3.2}$$

In which:

$$c_{g,x} = c_g \cos\theta \tag{3.3}$$

$$c_{g,y} = c_g \sin\theta \tag{3.4}$$

$$c_{\theta} = -\frac{1}{k}\left(\frac{\partial \sigma}{\partial d}\frac{\partial d}{\partial m} + k\frac{\partial U}{\partial m}\right) \tag{3.5}$$

$$c_{\sigma} = \frac{\partial \sigma}{\partial d}\left(\frac{\partial d}{\partial t} + U\nabla d\right) - c_g k\frac{\partial U}{\partial s} \tag{3.6}$$

The first term in equation 3.2 represents the change of wave action over time. This term will be equal to zero when the situation is

considered stationary. The second and third terms represent the shoaling of the waves. This is accounted for in the depth-dependent group velocities. The fourth term is the refraction/diffraction term. The waves that pass through the coastal region change direction. Hence it propagates through x, y and θ-space. The fifth term represents the frequency shifting of the waves. The term that represents the work done by the ambient currents against the radiation stresses is not included in the action balance equation presented with equation 3.2.

Equation 3.5 represents the refraction-induced turning rate of the individual wave components in the wave field. The turning rate depends on a velocity gradient perpendicular to the wave propagation direction and on a gradient in the water depth perpendicular to the wave propagation direction. It can also be seen as the propagation speed in directional space.

Equation 3.6 represents the rate of change of the relative frequency. The first term in the brackets represents the effect of the time variation of the depth whereas the second term in the brackets represents the effect of the current bodily moving the wave over a horizontally varying depth. The second term on the right hand side represents the effect of the moving with a horizontally varying current along the direction of the waves. It can also be seen as the propagation speed in frequency space.

The source term S consists of three different processes: generation by wind, wave-wave interactions and energy dissipation. The deep-water wave processes are wind input (S_{in}), quadruplet wave-wave interactions (S_{nl4}) and white-capping (S_{wc}) and the shallow-water wave processes are triad wave-wave interactions (S_{nl3}), bottom friction (S_{bfr}) and depth-induced wave breaking (S_{surf}). The shallow

water wave processes are only active in shallow water, whereas the deep water wave processes are active in both deep water and shallow water.

$$\begin{aligned} S_{tot}(\sigma,\theta) &= S_{in}(\sigma,\theta) + S_{nl}(\sigma,\theta) + S_{diss}(\sigma,\theta) = \\ &= S_{in} + S_{nl4} + S_{wc} + S_{nl3} + S_{bfr} + S_{surf} \end{aligned} \tag{3.7}$$

3.3 The source terms

In this section a short description of the source terms is given.

3.3.1 Wind input

Wind input is a deep water generation source term. It is a combination of the resonance mechanism by Phillips (1957) and the positive-feedback mechanism by Miles (1957). The former varies linearly in time whereas the latter varies exponential in time. This source term is described as:

$$S_{in} = A + BE(\sigma,\theta) \tag{3.8}$$

In which A and B are coefficients that depend both on wave frequency, wave direction, wind speed and wind direction. The linear growth A is described by Cavaleri and Malanotte-Rizzoli (1981):

$$A = \frac{1.5 \cdot 10^{-3}}{2\pi g^2}\left[u_* \cos\left(\theta - \theta_{wind}\right)\right]^4 H \tag{3.9}$$

In which:

$$H = \exp\left[-\left(\frac{\sigma}{\sigma^{*}_{PM}}\right)^{-4}\right] \qquad \text{with} \quad \sigma^{*}_{PM} = 2\pi\frac{0.13g}{28u_{*}} \tag{3.10}$$

The exponential growth B is described by Komen *et al.* (1984):

$$B = 0.25\frac{\rho_{air}}{\rho_{water}}\left[28\frac{u_{*}}{c}\cos\left(\theta-\theta_{wind}\right)-1\right]\sigma \tag{3.11}$$

It can be seen from equation 3.11 that the ratio between the wind speed u_{*} and the phase speed c is important. In shallow water the phase speed becomes less and therefore increases this ratio. This means more energy transfer from the wind to the waves.

3.3.2 Quadruplet wave-wave interactions

The quadruplet wave-wave interactions are a deep water non-linear redistribution source term. During this process no energy is lost or gained but instead redistributed over the spectrum from the mid-frequencies to the lower and higher frequencies. The physical meaning of the quadruplet wave-wave interactions is four wave components resonate and in that process exchange energy, redistributing the wave energy. The expression for this source term, given by Hasselmann (1962), can be written in a Boltzmann integral:

$$\begin{aligned} S_{nl4}\left(\vec{k}_4\right) = &\int\int\int\int T_1\left(\vec{k}_1,\vec{k}_2,\vec{k}_3\right)E\left(\vec{k}_1\right)E\left(\vec{k}_2\right)E\left(\vec{k}_3\right)d\vec{k}_1 d\vec{k}_2 \\ &-E\left(\vec{k}_4\right)\int\int\int\int T_2\left(\vec{k}_1,\vec{k}_2,\vec{k}_4\right)E\left(\vec{k}_1\right)E\left(\vec{k}_2\right)d\vec{k}_1 d\vec{k}_2 \end{aligned} \tag{3.12}$$

Where $\vec{k}_3 = \vec{k}_1 + \vec{k}_2 - \vec{k}_4$ and $\vec{k}_4$ the vector wave number considered in the source term.
The Discrete Interaction Approximation (DIA) proposed by Hasselmann *et al.* (1985) is a simplification of the quadruplet wave-wave interactions and reduces the computational time considerably. The DIA is described as:

$$S_{nl4}(\sigma,\theta) = S^{*}_{nl4}(\sigma,\theta) + S^{**}_{nl4}(\sigma,\theta) \tag{3.13}$$

In which S^{*}_{nl4} is the first quadruplet configuration and is identical, but mirrored in directions to S^{**}_{nl4}. S^{*}_{nl4} is described as:

$$S^{*}_{nl4}(\sigma,\theta) = 2\delta S_{nl4}(\alpha_1\sigma,\theta) - \delta S_{nl4}(\alpha_2\sigma,\theta) - \delta S_{nl4}(\alpha_3\sigma,\theta) \tag{3.14}$$

In which $\alpha_1 = 1, \alpha_2 = 1+\lambda$ and $\alpha_3 = 1-\lambda$, $\lambda = 0.25$.
With each term (for $i = 1, 2, 3$) :

$$\begin{aligned}\delta S_{nl4}(\alpha_i\sigma,\theta) = C_{nl4}(2\pi)^2 g^{-4}\left(\frac{\sigma}{2\pi}\right)^{11}\cdot\ldots \\ \ldots\cdot\left\{E^2(\alpha_i\sigma,\theta)\left[\frac{E(\alpha_i\sigma^{+},\theta)}{(1+\lambda)^4}+\frac{E(\alpha_i\sigma^{-},\theta)}{(1-\lambda)^4}\right]\right\}-\ldots \\ \ldots-2\frac{E(\alpha_i\sigma,\theta)E(\alpha_i\sigma^{+},\theta)E(\alpha_i\sigma^{-},\theta)}{\left(1-\lambda^2\right)^4}\end{aligned} \tag{3.15}$$

In shallow water the same description is used but multiplied with a scaling factor $R(k_p d)$.

$$S_{nl4,\textit{finite depth}} = R(k_p d) S_{nl4,\textit{deep water}} \tag{3.16}$$

The scaling factor is given by:

$$R\left(k_p d\right) = 1 + \frac{C_{sh,1}}{k_p d}\left(1 - C_{sh,2} k_p d\right) e^{C_{sh,3} k_p d} \tag{3.17}$$

The scaling factor has a maximum value of 4.43 to avoid unrealistic values.

3.3.3 White capping

White capping is the breaking of waves on deep water and thus a dissipative source term. White capping is strongly related to the wave steepness. The expression for the white capping source term is (WAMDI 1988):

$$S_{wc}(\sigma,\theta) = -\Gamma \tilde{\sigma} \frac{k}{\tilde{k}} E(\sigma,\theta) \tag{3.18}$$

In which $\tilde{\sigma}$ and $\tilde{k}$ are the mean frequency and mean wave number respectively and are defined as (WAMDI 1988):

$$\tilde{\sigma} = \left[\frac{1}{m_0}\int_0^{2\pi}\int_0^{\infty}\frac{1}{\sigma}E(\sigma,\theta)\,d\sigma d\theta\right]^{-1} \tag{3.19}$$

and

$$\tilde{k} = \left[\frac{1}{m_0}\int_0^{2\pi}\int_0^{\infty}\frac{1}{\sqrt{k}}E(\sigma,\theta)\,d\sigma d\theta\right]^{-2} \tag{3.20}$$

Γ is a coefficient that depends on the overall wave steepness and is described as (Janssen 1991a):

$$\Gamma = C_{wc}\left(\left(1-\delta_{wc}\right) + \delta_{wc}\frac{k}{\tilde{k}}\right)\left(\frac{\tilde{s}}{\tilde{s}_{PM}}\right)^p \tag{3.21}$$

In which $\tilde{s}$ and $\tilde{s}_{PM}$ are the overall wave steepness and the overall wave steepness for the Pierson-Moskowitz spectrum respectively. The coefficients C_{wc}, δ_{wc} and p are tuneable.

3.3.4 Bottom friction

The bottom friction is a dissipative shallow water source term. The dissipation is proportional to the orbital velocity at the bottom and the source term may generally be represented by (Hasselmann 1973) :

$$S_{bfr}(\sigma,\theta) = -\frac{C_{bfr}}{g}\left[\frac{\sigma}{\sinh(kd)}\right]^2 E(\sigma,\theta)\, u_{rms,bottom} \tag{3.22}$$

In which C_{bfr} is a bottom friction coefficient. From equation 3.22 it can be seen that the dissipation due to bottom friction is quite larger in very shallow water (flats) than in deeper water (channels). The sand bars and sand waves might affect this wave process. The source term is expected to be larger on the top of the bars and waves than in the troughs.

3.3.5 Triad wave-wave interactions

The triad wave-wave interactions term is a shallow water non-linear redistribution term. This means that no energy is lost in this wave process, but redistributed, to the lower and higher frequencies. The triad wave-wave interactions are known to transfer energy from a wave component with frequency *f/2* to a wave component with double its frequency, thus *f*, and from that wave component to another wave component with double its frequency 2*f*.
The resonance conditions for three wave components are an analogy of the resonance conditions for four wave components. The conditions

are that the sum of frequencies and wave numbers of two wave components are equal to the frequency and wave number of the third wave component. The resonance conditions can are given by:

$$\begin{aligned} f_1 + f_2 &= f_3 \\ \vec{k}_1 + \vec{k}_2 &= \vec{k}_3 \end{aligned} \tag{3.23}$$

These resonance conditions cannot satisfy in deep water because a combination of wave components cannot be created with the dispersion relation of the linear wave theory. Therefore triad wave-wave interactions are only relevant in very shallow water. In slightly deeper water the resonance conditions nearly satisfy, resulting in energy transfer and phase coupling between the wave components involved. The amount of energy transfer depends on the phase differences of the wave components. This is quantified with the biphase:

$$\beta_{1,2} = \varphi_1 + \varphi_2 - \varphi_{1+2} \tag{3.24}$$

In which φ_1, φ_2 and φ_{1+2} are the phases of the wave components involved.
The biphase of self-self interaction at the peak frequency, which is used in SWAN can be roughly approximated with: (Holthuijsen 2007, p. 274):

$$\beta_{f_{peak}} = -\frac{\pi}{2} + \frac{\pi}{2}\tanh\left(\frac{\delta}{N_{Ursell}}\right) \tag{3.25}$$

In which δ is a coefficient that varies between 0.2 – 0.6 and N_{Ursell} is the Ursell number, which is defined as the ratio between the wave steepness and the relative water depth to the third power. The biphase varies from 0 to $-\pi/2$. The shape of the waves evolve from

roughly symmetrical to a sawtooth shape when the biphase progresses from 0 to $-\pi/2$.

The source term S_{nl3} is described as (Eldeberky 1996):

$$S_{nl3}(\sigma,\theta) = S^{+}_{nl3}(\sigma,\theta) + S^{-}_{nl3}(\sigma,\theta) \tag{3.26}$$

With:

$$S^{+}_{nl3}(\sigma,\theta) = C_{nl3} c c_g |\sin\beta| \left[E^2\left(\sigma/2,\theta\right) - 2E\left(\sigma/2,\theta\right) E(\sigma,\theta) \right] \tag{3.27}$$

and

$$S^{-}_{nl3}(\sigma,\theta) = -2E(2\sigma,\theta) \tag{3.28}$$

In which C_{nl3} is a coefficient that depends on the wave number, local depth, frequency and phase speed. From this it can be seen that when the Ursell number is large, the biphase progresses to $-\pi/2$. Therefore the triad wave-wave interactions are the strongest.

Since the triad wave-wave interactions depend on the local water depth it is affected by the sand bars and sand waves addressed in Chapter 2. The Ursell number will become larger on the top of the bars and waves and thus increase the value for the biphase, consequently increasing the source term.

3.3.6 Depth-induced breaking

Depth-induced breaking is a dissipative shallow water source term. The dissipation is proportional to the maximum wave height squared and the fraction of broken waves. The source term may be represented by (Battjes and Janssen 1978, Holthuijsen 2007, p. 281-283):

$$S_{surf}(\sigma,\theta) = \frac{\overline{D}_{surf}}{m_0} E(\sigma,\theta) \tag{3.29}$$

In which:

$$\overline{D}_{surf} = -\frac{1}{4}\alpha_{BJ} Q_b \overline{f}_0 H_{\max}^2 \tag{3.30}$$

In shallow water $H_{\max} = \gamma_{BJ} d$. In which γ_{BJ} is a model coefficient, often interpreted as a breaker index.
The sand bars and sand waves previously mentioned might affect this wave process. Depth-induced breaking is expected to be more active on the top of the sand bars and sand waves than in the troughs between these sand bars and sand waves.

3.4 Work done by the currents against the radiation stresses

Besides energy waves also transfer momentum. The transfer of wave-induced momentum is called the radiation stress (Longuet-Higgins and Stewart, 1960). In situations of non-uniform wave motion gradients in the radiation stress arise, which can result in a gradient in the mean water surface and it can result in currents through which the wave motion occurs. These effects are important in areas where the local wave properties vary greatly (i.e. the surf zone).

From Longuet-Higgins and Stewart (1964) the energy balance equation is:

$$\frac{\partial E}{\partial t} + \frac{\partial}{\partial x_\alpha}\left[E\left(U + c_g\right)\right] + \Phi_{\alpha\beta}\frac{\partial U_\beta}{\partial x_\alpha} = 0 \tag{3.31}$$

The last term represents the work done by the ambient currents against the radiation stresses. In which $\Phi_{\alpha\beta}$ is the radiation stress tensor.
This term can be determined by calculating all the velocity gradients.

$$\Phi_{\alpha\beta}\frac{\partial U_\beta}{\partial x_\alpha} = \Phi_{xx}\frac{\partial U_x}{\partial x} + \Phi_{xy}\frac{\partial U_y}{\partial x} + \Phi_{yx}\frac{\partial U_x}{\partial y} + \Phi_{yy}\frac{\partial U_y}{\partial y} \tag{3.32}$$

An alternative, simpler approach is to describe this term as a residual term of the spectral energy balance equation. To compute this term from SWAN output, the terms of the spectral action balance equation can be rewritten in terms of wave energy, so that the residual term follows directly from the model simulations.

$$\begin{aligned}\Phi_{\alpha\beta}\frac{\partial U_\beta}{\partial x_\alpha} = S(\sigma,\theta;x,y,t) - \frac{\partial F(\sigma,\theta;x,y,t)}{\partial t} - \frac{\partial\, c_{g,x}F(\sigma,\theta;x,y,t)}{\partial x} - \ldots \\ \ldots - \frac{\partial\, c_{g,y}F(\sigma,\theta;x,y,t)}{\partial y} - \frac{\partial\, c_\theta F(\sigma,\theta;x,y,t)}{\partial \theta} - \frac{\partial\, c_\sigma F(\sigma,\theta;x,y,t)}{\partial \sigma}\end{aligned} \tag{3.33}$$

For the WAM *Cycle_4* model, the work done by the ambient currents against the radiation stresses is derived from the term in the spectral energy balance equation that accounts for the interaction between the waves and the currents (Osuna and Monbaliu, 2004)[2]. A similar derivation is given in paragraph 3.5.

[2] This derivation is a factor 2 smaller than the derivation presented in equation 3.33 and Section 3.5

3.5 Derivation of the Radiation stress term.

This section gives a derivation of the radiation stress term, to verify the approach of using a rest term to describe the work done by the ambient currents against the radiation stresses.

The action balance is written as a material derivative.

$$\frac{dN}{dt} = \frac{S}{\sigma} \tag{3.34}$$

Equation 3.34 can be rewritten in terms of energy

$$\frac{d\sigma N}{dt} = N\frac{d\sigma}{dt} + \sigma\frac{dN}{dt} = N\frac{d\sigma}{dt} + S = \frac{dE}{dt} \tag{3.35}$$

As a result:

$$N\frac{d\sigma}{dt} = \frac{dE}{dt} - S \tag{3.36}$$

In the term $N \cdot d\sigma/dt$ lies our interest. The derivative of the radian frequency can be written as (Holthuijsen p. 220)

$$\frac{d\sigma}{dt} = \left[\frac{\partial\sigma}{\partial d}\left(\frac{\partial d}{\partial t} + U\nabla d\right) - c_g k\frac{\partial U}{\partial s}\right] \tag{3.37}$$

Multiplying equation 3.37 with wave action

$$N\frac{d\sigma}{dt} = \frac{E}{\sigma}\left[\frac{\partial\sigma}{\partial d}\left(\frac{\partial d}{\partial t} + U\nabla d\right) - c_g k\frac{\partial U}{\partial s}\right] \tag{3.38}$$

According to Phillips (1977, p. 69) equation 3.38 can be rewritten as

$$N\frac{d\sigma}{dt} = \frac{E}{\sigma}k_\alpha\left(c_{\ g}\right)_\beta\frac{\partial U_\alpha}{\partial x_\beta} + \frac{1}{2}E\left(\frac{2c_g}{c} - 1\right)\frac{\partial U_\beta}{\partial x_\beta} \tag{3.39}$$

Equation 3.39 can be rewritten as

$$N\frac{d\sigma}{dt} = E\left[l_\alpha l_\beta\frac{c_g}{c} + \frac{1}{2}\left(\frac{2c_g}{c} - 1\right)\delta_{\alpha\beta}\right]\frac{\partial U_\alpha}{\partial x_\beta} \tag{3.40}$$

In which $l_\alpha = k_\alpha/k$ and $l_\beta = k_\beta/k$ (Phillips 1977, p. 68)
The part between the right brackets corresponds with the general expression for the radiation stress, which is (Phillips, 1977, p. 68, Longuet-Higgins and Stewart, 1964):

$$\Phi_{\alpha\beta} = \left(n - \frac{1}{2}\right)E\delta_{\alpha\beta} + nE\frac{k_\alpha k_\beta}{k^2} = E\left[\left(n - \frac{1}{2}\right)\delta_{\alpha\beta} + n\frac{k_\alpha k_\beta}{k^2}\right] \tag{3.41}$$

Substituting this into equation 3.40 it can be concluded that

$$N\frac{d\sigma}{dt} = \Phi_{\alpha\beta}\frac{\partial U_\beta}{\partial x_\alpha} \tag{3.42}$$

Thus the radiation stress term is the same as the residual term used in equation 3.33.

4 Model setup

4.1 Introduction

All terms in the energy balance equation can be calculated in a numerical wave model. In this case the SWAN model is used, which is a third generation wave model. As previously mentioned a third generation wave model is a model in which a wave spectrum is free to develop without a specific shape imposed beforehand. Furthermore, the non-linear wave-wave interactions are calculated explicitly.

Before SWAN could be used slight modifications to the code had to be made, since additional output was required to study the terms presented in Chapter 3. Firstly, the propagation terms had to be made into output parameters. Secondly, the radiation stress term had to be realised. The output of all propagation term and source terms individually can improve the insight of the wave processes significantly. Another small modification is that the output of the shoaling terms (in x and y-direction) is made into one term to represent the magnitude of the shoaling:

$$\sqrt{\left(\frac{\partial\, c_{g,x} E(\sigma,\theta;x,y,t)}{\partial x}\right)^2 + \left(\frac{\partial\, c_{g,y} E(\sigma,\theta;x,y,t)}{\partial y}\right)^2}$$

4.2 Grids and boundary conditions

Two different grids were used for the calculations of the wave processes. Both grids are curvi-linear. These grids were created and used in a sensitivity study by WL & Alkyon (2007) and are given in Figure 4-1. The larger of the two grids covers the entire Waddenzee area and is called the NS 2 grid. This grid is derived from the Kuststrook model. The NS 2 grid is used to determine the wave conditions for the entire Waddenzee. The boundary conditions for this calculation were $H_s = 6$ m, $T_p = 12$ s, $U_{10} = 15$ m/s from the north. In addition to the determination of the wave conditions in the Waddenzee, the boundary conditions for the nested AZG3A grid were calculated. These boundary conditions consist of two-dimensional spectra and $U_{10} = 15$ m/s from the North. The AZG3A grid is 3 times denser than the NS2 grid.

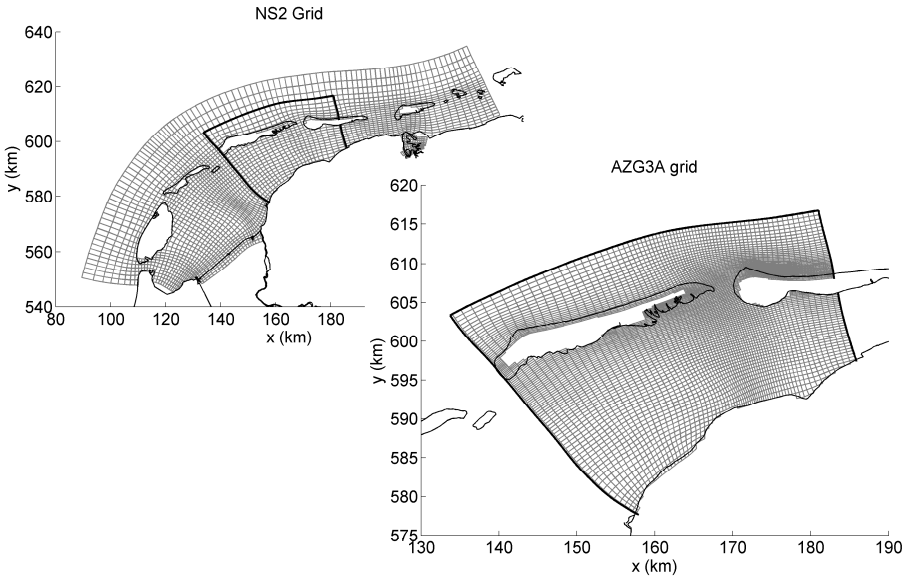

Figure 4-1 Computational grids NS2 and AZG3A. The AZG3A grid is 3 times denser than the NS 2 grid.

4.3 Model settings

The computations were made using the SWAN cycle III 40.72. Van der Westhuysen (2007) proposed, for deep water wave processes, a combination for wind input and non-linear saturated-based white capping. For the Amerlander Zeegat this combination worked better than the standard option in SWAN (Alkyon report A2085, 2008). The quadruplet wave-wave interactions were modelled using the Discrete Interaction Approximation (DIA) proposed by Hasselmann *et al.* (1985). The shallow water non-linear triad wave-wave interactions are included in the calculations according to the Lumped Triad Approximation (LTA) proposed by Eldeberky (1996). The bottom friction is calculated according to Hasselmann *et al.* (1973), with its default settings in SWAN. The dissipation of the depth-induced breaking is calculated according to the bore-based model of Battjes and Janssen (1978) with its default settings.

For this study the selected convergence criteria are based on the curvature criteria (Zijlema and Van der Westhuysen 2005). The curvature criteria represent the stopping criterion for the iteration process. This process is stopped when the curvature of the successive computed value of the significant wave height, regarded as a continuous series, reduces below a certain normalised value. In this study this normalised value was set at 0.001.

5 Normalisation

The total wave energy m_0 is proportional to H_{m0}^2. This can be described as:

$$m_0 = \iint F(\sigma,\theta)\, d\sigma d\theta \approx 1/16\, H_{m_0}^2 \tag{5.1}$$

The geographical distribution of H_{m0} is given in Figure 5-1.

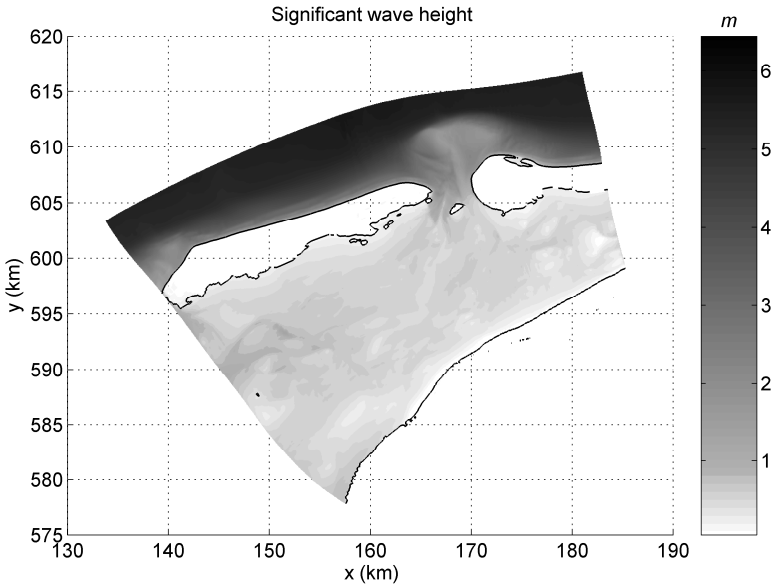

Figure 5-1 Geographical distribution of the significant wave height

Looking at Figure 5-1 it can be seen that H_{m0} is lower behind the barrier islands than in the North Sea. The barrier islands shield the Waddenzee interior from waves approaching from the North Sea. Since H_{m0} is lower behind the barrier islands the wave energy is also lower. For this reason the wave processes would only show up outside the Waddenzee. The aim of this study is to understand more about

the wave processes and their geographical distribution in the Waddenzee interior.
To interpret the various processes, the spatial variation of the intensity of each term of the energy balance is considered. The intensity is defined as the integral over the spectral domain of the absolute value of the term under consideration. The basic reason to take the absolute value here is to include the wave-wave interactions. These are in principle conservative and the integral of the term itself over the spectral domain would be zero. In addition these integrated terms will be normalised with the total energy m_0 to arrive at the time scales of the processes.

5.1 Time scales

All output terms of the spectral energy balance equation have the dimension m^2/s. The dimension of m_0 is m^2, therefore when dividing all the output terms by m_0 the result is an inverse time scale ($1/s$).

A common definition of time scale τ for the total wave energy is based on the absolute rate of change of total wave energy.

$$\frac{1}{m_0}\iint\left|\frac{\partial F(\sigma,\theta)}{\partial t}\right|d\sigma d\theta \tag{5.2}$$

According to Leibniz integration rule for differentiation under the integral sign equation 5.2 can be rewritten as:

$$\frac{1}{m_0}\frac{\partial}{\partial t}\int_0^{2\pi}\int_0^{\infty}F(\sigma,\theta)d\sigma d\theta \tag{5.3}$$

The derivative can simply be written before the integration signs because the integration is done over a fixed domain. Substituting equation 5.1 into equation 5.3

$$\frac{1}{m_0}\left|\frac{\partial m_0}{\partial t}\right| \tag{5.4}$$

Because we look at the terms individually, it is possible to say that

$$\left|\frac{\partial m_0}{\partial t}\right| = \frac{1}{\tau_t} m_0 \tag{5.5}$$

The result is an inverse time scale.

$$\tau_t = \left[\frac{1}{m_0}\left|\frac{\partial m_0}{\partial t}\right|\right]^{-1} \tag{5.6}$$

Applying this on the other terms in the spectral energy balance equation, results in similar time scales for all the other terms individually.
A different approach to demonstrate this is by considering each term in the spectral energy balance equation individually. For example, when considering only the frequency shifting term, all the other terms, except the rate of change of wave energy over time, are considered to be zero. This results in:

$$\frac{\partial E(\sigma,\theta)}{\partial t} = -\frac{\partial c_\sigma E(\sigma,\theta)}{\partial \sigma} \tag{5.7}$$

When integrating the absolute value of both sides over the spectral domain and normalise with m_0 this results in:

$$\frac{1}{m_0}\int_0^{2\pi}\int_0^{\infty}\left|\frac{\partial F(\sigma,\theta)}{\partial t}\right|d\sigma d\theta = \frac{1}{m_0}\int_0^{2\pi}\int_0^{\infty}\left|\frac{\partial c_\sigma F(\sigma,\theta)}{\partial \sigma}\right|d\sigma d\theta \tag{5.8}$$

For the left hand side equation 5.2 to equation 5.6 can be applied, which results in the inverse time scale. The right hand side consequently must also become an inverse time scale.

$$\tau_\sigma = \left[\frac{1}{m_0}\iint\left|\frac{\partial c_\sigma F(\sigma,\theta)}{\partial \sigma}\right|d\sigma d\theta\right]^{-1} \tag{5.9}$$

The shortest time scales indicate the highest intensity of the wave process considered. Every wave process, and with that, every term in the energy balance equation has its individual time scale.

6 Wave characteristics

To understand the geographical distribution of the different wave processes it can be useful to look at other wave characteristics first. The wave characteristics that can be useful are wave steepness and the Ursell number and are shown in Figure 6-1 and Figure 6-2 respectively. The wave steepness is the ratio between the wave height and wave length ($s = H/L$) and is a wave characteristic that determines the intensity of wave processes like white capping and quadruplet wave-wave interactions. The Ursell number is the ratio between the wave steepness and the relative depth to third power. $N_{Ursell} = \left(H/L\right)/(kd)^3 \sim HL^2/d^3$. In which $k = 2\pi/L$. As described in Section 3.3.5 the Ursell number determines the non-linearity of the wave field and the biphase. When the Ursell number is large the triad wave-wave interactions become most active. In SWAN the Ursell number is defined as:

$$U_r = \frac{g}{8\sqrt{2}\pi^2}\frac{H_s T_{m01}^2}{d^2} \tag{6.1}$$

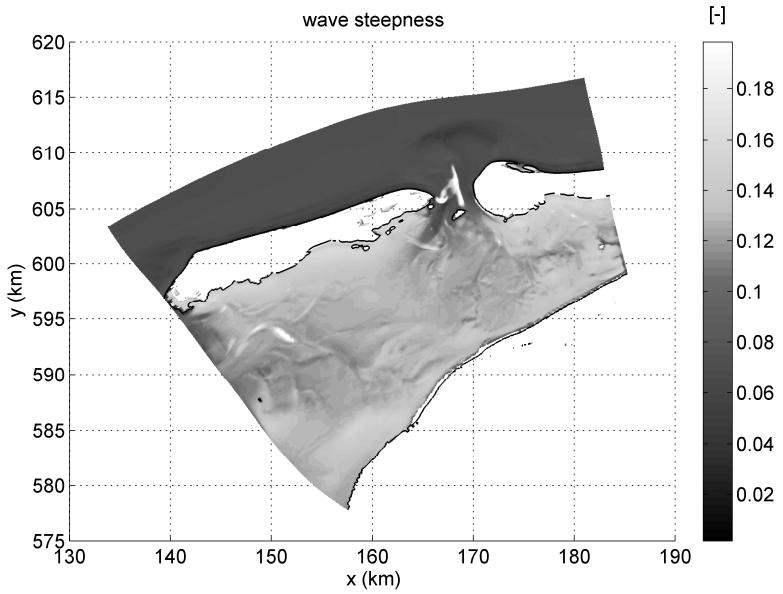

Figure 6-1 Geographical distribution of the wave steepness

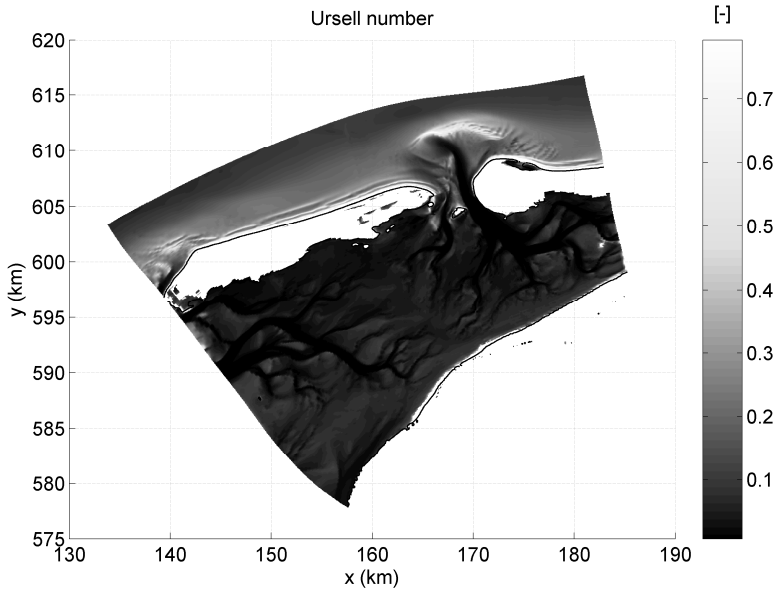

Figure 6-2 Geographical distribution of the Ursell Number.

7 Results and discussion

The results are presented in a number of geographical maps. First the propagation terms are presented, then the source terms and finally the radiation stress term. As stated before the output dimensions are inverse timescales (*1/s*). In all figures the coastlines of the barrier islands and the Frisian coast are drawn.

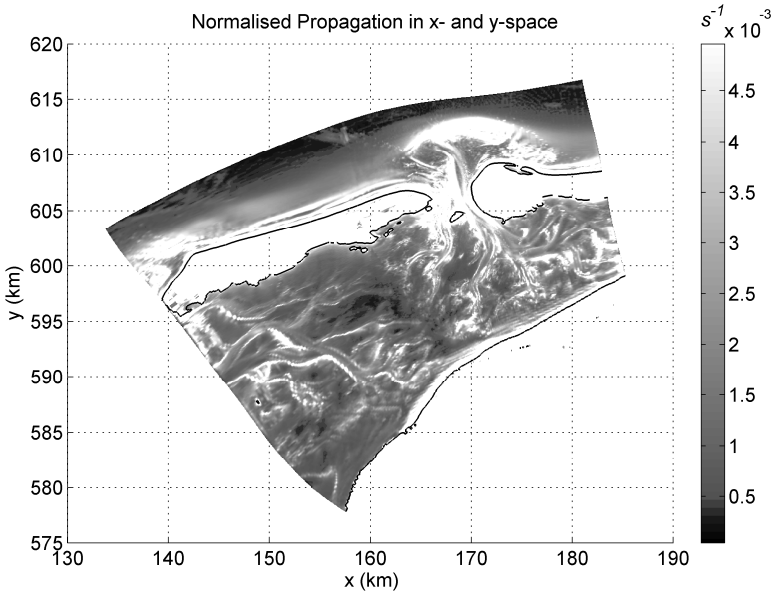

Figure 7-1 Geographical distribution of the time scale of the shoaling term

The propagation in x and y-direction or shoaling term (Figure 7-1) is most active in the surf zone. The surf zone is where the most shoaling occurs. The sand bars and sand waves, presented in Figure 2-4, are recognisable. In between the long banks and in between the sand waves the opposite effect occurs (de-shoaling). The shortest timescales are of the order of 200 *s.*

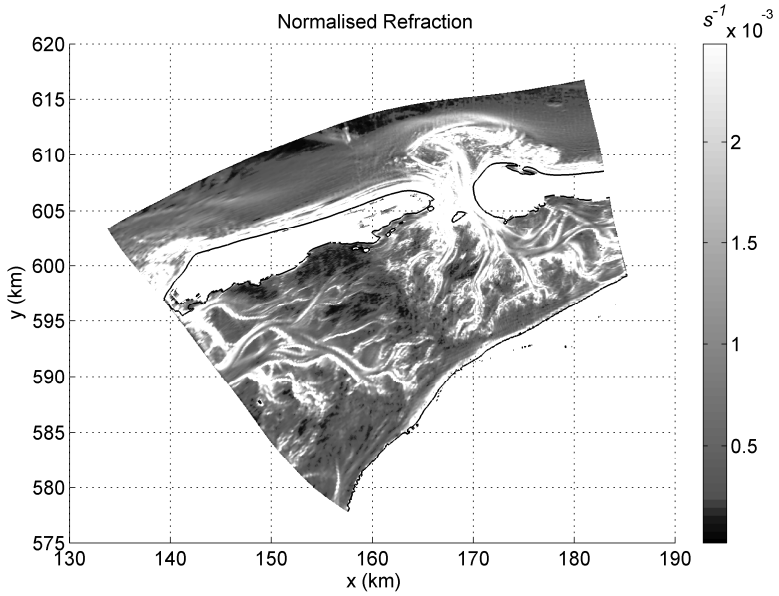

Figure 7-2 Geographical distribution of the time scale of the refraction term

The pattern of the refraction term (Figure 7-2) is quite similar to that of the shoaling term (Figure 7-1). The refraction term shows to be most active on the banks of the channels and in the surf zone. Refraction is determined by the propagation speed in directional space c_θ which is given by equation 3.5. It states that waves refract when there are gradients in the depth and currents perpendicular to the wave direction. There are many gradients in the depth and currents in the interior of the Waddenzee. The steepest gradients are on the banks of the channels, consequently the refraction term is the most intense on the banks of the channels.

Since the currents on the North Sea pass the outer delta heading eastward the steepest gradients in the depth and currents are on the North Sea coasts of the barrier islands and the outer delta.

The shortest timescales, which are of the order 400 *s,* are on the banks of the channels and in the surf zone.

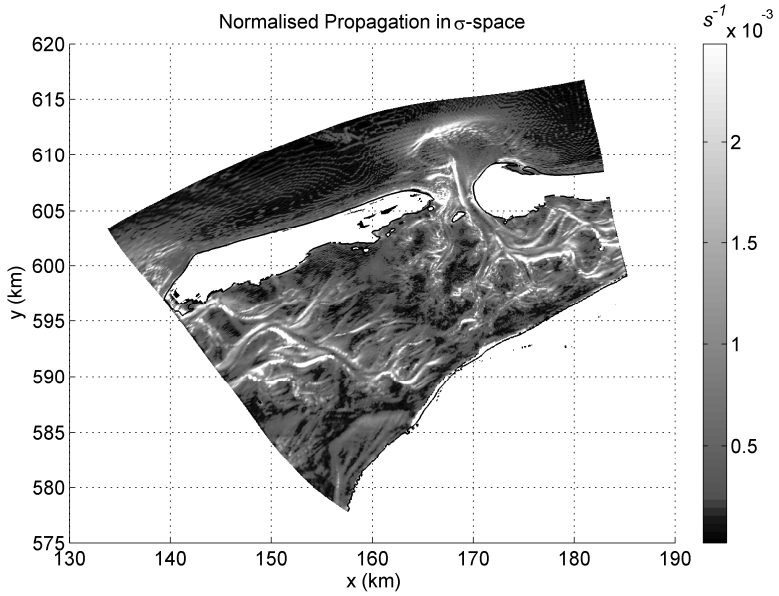

Figure 7-3 Geographical distribution of the time scale of the Doppler term

The propagation in frequency space (Figure 7-3) (Doppler term) is most effective on the banks of the channels in the inlet and on the bank of the outer delta. Equation 3.6 describes the propagation speed in frequency space c_σ which partly determines this term. Equation 3.6 states that frequency shifting occurs when there are gradients in the depth and currents in the propagation direction of the waves. The wave direction is mainly from the north, therefore the largest gradients in the depth and currents are on the banks of the channels in the west-east or east-west direction. The same holds for the outer delta.

The timescales there are of the order of 400 s.

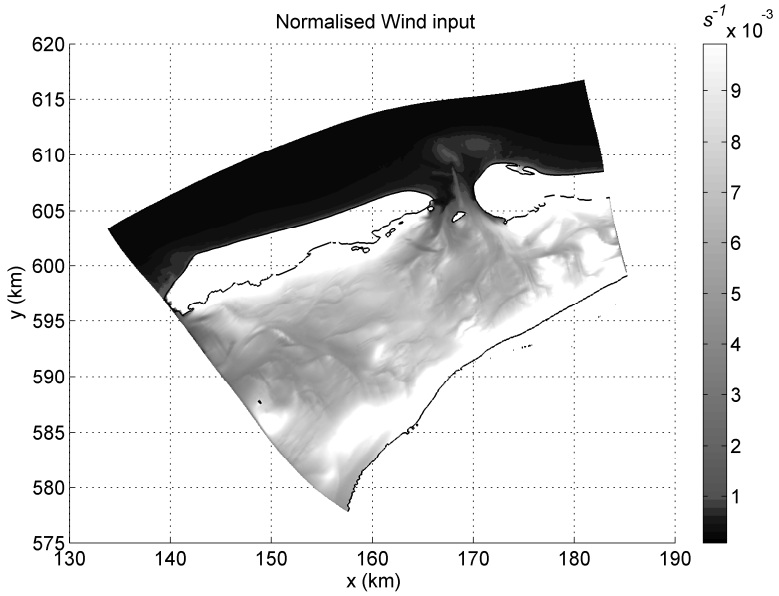

Figure 7-4 Geographical distribution of the time scale of the wind input

The wind input (Figure 7-4) is the most effective at the Frisian coast and at the leeside of the barrier islands. The shortest timescales are of the order 100 *s*. The wind input is most effective behind the barrier islands, because of a young sea state, which means that the waves grow fairly rapidly. The intensity of the wind input at the Frisian coast may be explained by the fact that the phase speed becomes less. The phase speed depends on the local water depth, which gets less near the Frisian coast. This means that the ratio of wind speed over phase speed of the waves gets larger, consequently, increasing the transfer of energy to the waves (see equation 3.11).

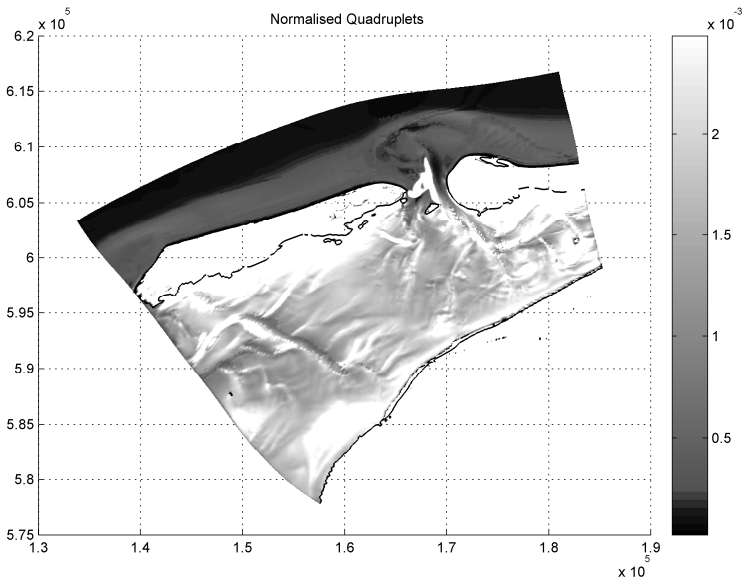

Figure 7-5 Geographical distribution of the time scale of the quadruplet wave-wave interactions

The quadruplet wave-wave interactions (Figure 7-5) are most effective on the leeside of the barrier islands and at the West side of the Frisian coastline. This can be explained with the wave steepness. The pattern of the quadruplet wave-wave interactions is very similar to that of the wave steepness (see Figure 6-1). At areas where the waves are steep the quadruplet wave-wave interactions are also strong. The reason why the quadruplet wave-wave interactions are strong at the leeside of the barrier islands can be explained with equation 3.15. Behind the barrier islands is a young sea state, which means that there are short waves and therefore high frequency waves. The frequency is taken to the 11^{th} power, which makes the wave frequency important. The shortest timescales are of the order of 400 *s.*

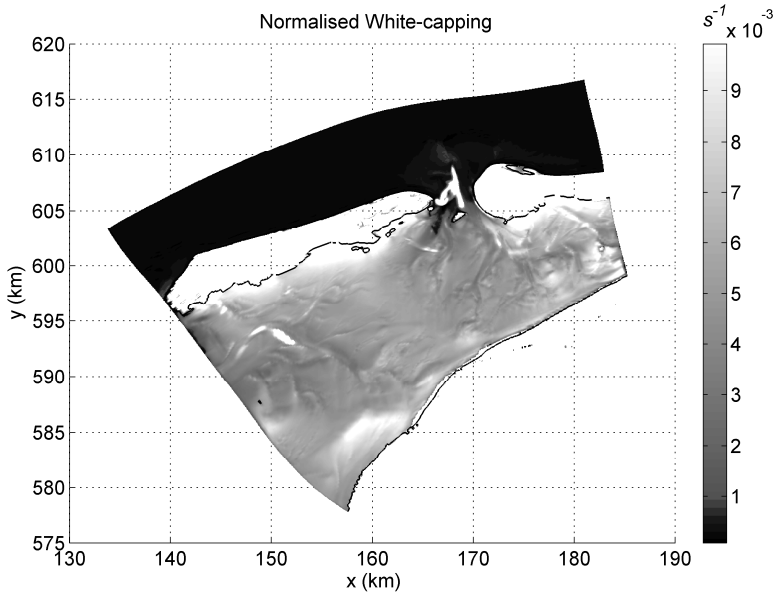

Figure 7-6 Geographical distribution of the time scale of the white-capping

For white capping (Figure 7-6), the smallest time scales at which dissipation occurs are behind the barrier islands. It looks very similar to the wind input and also shows similarities with the quadruplet wave-wave interactions and the wave steepness. White capping depends strongly on the steepness parameter Γ, which is described by equation 3.21 and depends on the overall wave steepness. Therefore the pattern in the wave steepness (Figure 6-1) is easily recognisable in the figure representing the normalised white capping.
The high frequency waves generated by the quadruplet wave-wave interactions are dissipated behind the barrier islands.
The smallest time scales for white capping are of the order of 100 *s*.

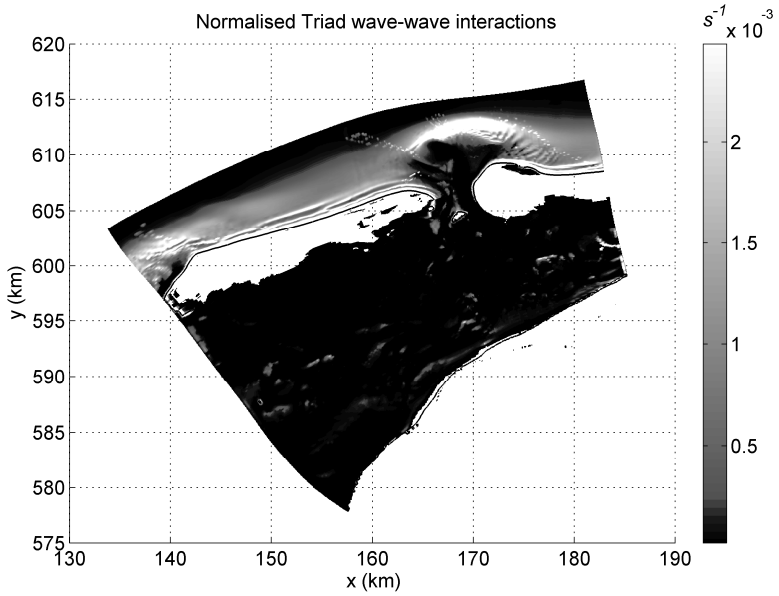

Figure 7-7 Geographical distribution of the time scale of the traid wave-wave interactions

The area where the triad wave-wave interactions (Figure 7-7) are the strongest is on the ebb tidal delta and on the long sand banks in front of the barrier islands. The Ursell number is also large there. (see Figure 6-2) When the Ursell number is large the biphase progresses to $-\pi/2$, which means that the waves tend to form a saw-tooth shape with steep wave fronts. In this particular form and in very shallow water the triad wave-wave interactions are at their strongest. This situation occurs on the locations mentioned previously.

The shortest timescales are of the order of 400 *s*. In the areas where these timescales occur, the most energy is redistributed to higher frequency waves.

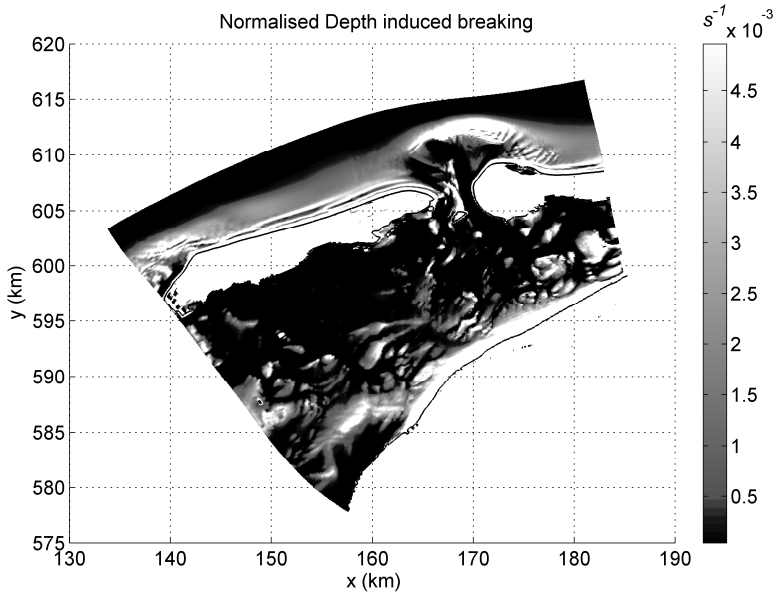

Figure 7-8 Geographical distribution of the time scale of the depth induced breaking

The depth-induced breaking (Figure 7-8) is most effective at the Frisian coast, along the barrier island's North Sea coast and on the ebb tidal delta. In these zones the time scales of the energy dissipation are of the order of 200 *s*. A noticeable feature is that there is an "on-off"-character. That is comparable with waves breaking or not.

This wave process is strongly affected by the sand waves and long sand banks. The energy dissipation occurs the fastest on the sand banks and on the sand waves. In between the banks and waves the effect is less.

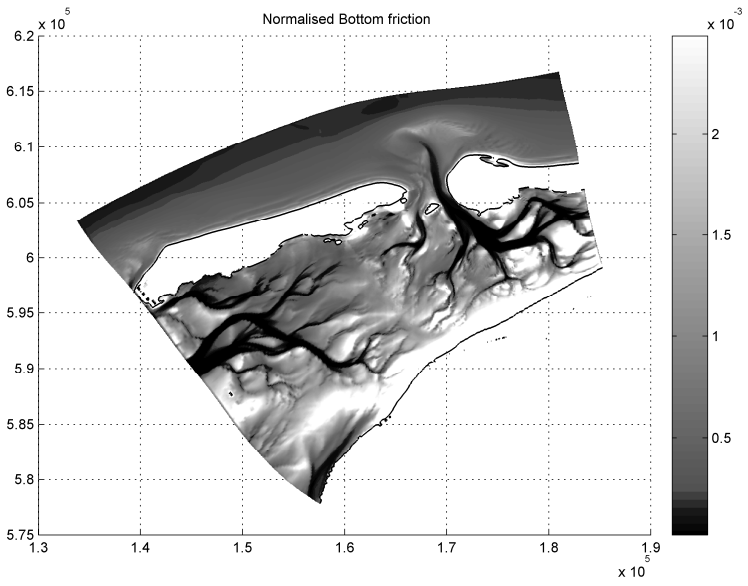

Figure 7-9 Geographical distribution of the time scale of the bottom friction

The bottom friction term (Figure 7-9) is most effective at the Frisian coast, on the flats and along the North Sea coast of the barrier islands and is absent in the channels. The description of the bottom friction is presented by equation 3.22 and from that it can be seen that there is a strong relation with the relative water depth kd. Equation 3.22 states that the larger kd the smaller the source term and thus the larger the time scales.

The smallest timescales are of the order 400 s.

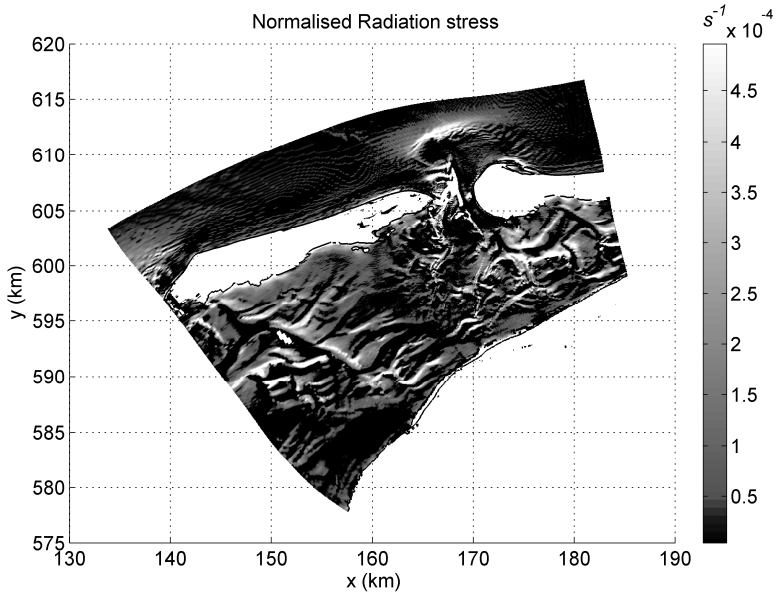

Figure 7-10 Geographical distribution of the time scale of the radiation stress term

The pattern of the work done by the ambient currents against the radiation stresses (Figure 7-10) is very similar to that of the propagation in frequency space. This can be explained with equation 3.37. The derivative $d\sigma/dt$ is the same as the propagation speed c_σ (see equation 3.6), which also determines the propagation in frequency space. Therefore the pattern in Figure 7-3 and Figure 7-10 is due to the propagation speed c_σ. This term is most intense where the gradients in the current are the steepest.

The shortest time scales are in the order of 2500 s, which is one order larger than the time scales of the other terms. For this reason it can be assumed that this term is of lesser importance to the wave field.

It must be noted that Figure 7-10 is a result of the calculation of the radiation stress term as a residual term. Hence, all the possible numerical errors are in this result. The numerical errors of all the terms individually might be of the same order as the result of the work done by the ambient currents against the radiation stresses.

In overview the results can be summarised by the following. The output dimension of the output terms is s^{-1} and the timescales of the different wave processes vary from 100-1000 s. However, the work done by the ambient current against the radiation stresses has a representative timescale that is one order larger than all the other terms (2500-10000 s).

The geographical maps show that the shortest time scales of the propagation terms are mostly located on the banks of the channels and on the outer delta, while for the deep-water source terms the shortest time scales are mainly behind the barrier islands. For the shallow-water source terms the shortest time scales of the triad wave-wave interactions and the depth induced wave breaking are on the North Sea side of the barrier islands, while the shortest time scales of bottom friction dissipation are closely related to the local water depth.

8 Conclusion

The results of this study revealed that the time scales can be used for understanding of, and insight in the wave processes. The time scales indicate the time in which energy is gained, redistributed or dissipated.

The geographical distributions of the different terms in the spectral action balance equation are very useful in seeing which wave process is strong on any location.

The analysis of the time scales, or source term magnitudes, pointed out that the deep water wave processes are stronger on the interior of the Waddenzee than the shallow water wave processes, whereas the shallow water wave processes are strongest on the outer delta and barrier island coasts. Bottom friction and depth-induced breaking proved to be dominant locally on the flats and Frisian coastline. The reason why the deep water wave processes are stronger can be due to the shielding of the interior by the barrier islands. This means that the wave conditions from the North Sea hardly penetrate the Waddenzee area and that the wave conditions in the Waddenzee are locally generated. The wave field can therefore be denoted as a young sea state.

The wave processes that were expected to be affected by the sand bars and sand waves, shoaling, bottom friction, triad wave-wave interactions and depth-induced breaking, were indeed affected.

The radiation stress term implemented in the SWAN model turned out to be significantly smaller than all other terms considered. Since the radiation stress term was calculated as a residual term numerical errors of the other wave processes were included in this result.

The geographical distributions of the wave processes give great insight in where which wave processes are most active and which are not.

What can be done with this knowledge? Knowing the geographical distribution of certain wave processes under certain wave conditions can be very useful for improving the locations where measurement buoys need to be placed.

Measurement records are very useful for verification in hind cast studies. Through comparing the measurements with the results from the SWAN model, possible errors in the SWAN model can be found. Here again the geographical distributions can prove their value. With the geographical distributions it can be seen which wave processes are of importance at this location and thus which processes contribute the most to the possible prediction errors. By this an efficient method of finding and fixing possible errors is presented.

9 References

- Alkyon (2008). Analysis of SWAN hindcasts Wadden Sea, Oosterschelde and Slotermeer. Alkyon, Report A2085, May 2008.
- Battjes, J.A., and J.P.F.M. Janssen, 1978, Energy loss and set-up due to breaking of random waves, *Proc. 16th Int. Conf. on Coastal Engineering. ASCE, New York,* pp. 570 – 587.
- Booij, N., R.C. Ris and L.H. Holthuijsen, 1999, A third-generation wave model for coastal regions, Part I, Model description and validation, *J. Geophys. Res.,* 104, C4, 7649 – 7666.
- Eldeberky, Y., 1996, Nonlinear transformation of wave spectra in the nearshore zone, Ph.D. theses, published as *Communications on Hydraulic and Geotechnical Engineering,* Delft Unifversity of Technology, Faculty of Civil Engineering, Report No. 96 - 4, 203 pp.
- Gelci, R., H. Cazalé, J. Vassal, 1957, Prévision de la houle. La méthode des densités spectroangulaires. *Bulletin d'information du Comité central d'Océanographie et d'Etude de Côtes,* 9, 416 – 435.
- Hasselmann, K., 1962, On the nonlinear energy tranfer in a gravity-wave spectrum. Part 1: General theory, *J. Fluid. Mech.*, 12, 481 – 500.
- Hasselmann, K., T.P. Barnett, E. Bouws, H. Carlson, D.E. Cartwright, K. Enke, J.A. Ewing, H. Gienapp, D.E. Hasselmann, P. Kruseman, A. Meerburg, O. Müller, D.J. Olbers, K. Richter, W. Sell and H. Walden, 1973, Measurements of wind-wave growth and swell decay during

the JOint North Sea WAve Project (JONSWAP), *Deutsch. Hydrogr. Z.,* Suppl., A8, 12, 95 pp.

- Hasselmann, K., 1974, On the spectral dissipation of ocean waves due to white capping, *Boundary-layer Meteorol.*, 6, 1 – 2, 107 – 127.
- Hasselmann, S., K. Hasselmann, J.H. Allender and T.P. Barnett, 1985a, Computations and parameterizations of the nonlinear energy transfer in a gravity wave spectrum. Part II: parameterizations of the nonlinear transfer for applications in wave models, *J. phys. Oceanogr.,* 15, 11, 1378 – 1391.
- Holthuijsen, L.H., 2007, *Waves in oceanic and coastal waters*. 1st edition: Cambridge university press, pp. 387.
- Janssen P.A.E.M., 1991, Quasi-linear theory of wind-wave generation applied to wave forecasting, *J. Phys. Oceanogr.,* 21, 11, 1631 – 1642.
- Janssen P.A.E.M., and J.-R. Bidlot, 2003, Part VII: ECMWF Wave-model documentation, *IFS Documentation Cycle,* CY23r4.
- Komen, G.J., and S. Hasselmann, 1984, On the existence of a fully developed wind-sea spectrum, *J. Phys. Oceanogr.*, 14, 8, 1271 – 1285.
- Komen, G.J., 2004, The wave modelling (WAM) group, a historical perspective, *16th BMRC modelling workshop: Past, present and future of numerical modelling.*
- Longuet-Higgins, M.S., and R.W. Stewart, 1960, Changes in the form of short gravity waves on lang waves and tidal currents, *J. Fluid Mech.*, 8, 4, 565 – 583.
- Longuet-Higgins, M.S., and R.W. Stewart, 1964, Radiation stresses in water waves; a physical discussion, with applications. *Deep-sea Res.*, 11, 4, 529 – 562.
- Osuna, P., and J. Monbaliu, 2004, Wave-current interactions in the Southern North Sea, *J. Mar. Syst.* 52, 65 – 87.

- Phillips, O.M., 1958, The equilibrium range in the spectrum of wind-generated waves, *J. Fluid Mech.,* 4, 426 – 434.
- Phillips, O.M., 1977, *The dynamics of the upper ocean.* 2nd edition: Cambridge university press.
- SWAMP group: J.H. Allender, T.P. Barnett, L. Bertotti, J. Bruinsma, V.J. Cardone, L. Cavaleri, J. Ephraums, B. Golding, A. Greenwood, J. Guddal, H. Günther, K. Hasselmann, S. Hasselmann, P. Joseph, S. Kawai, G.J. Komen, L. Lawson, H. Linné, R.B. Long, M. Lybanon, E. Maeland, W. Rosenthal, Y. Toba, T. Uji and W.J.P. de Voogt, 1985. Sea wave modeling project (SWAMP). An intercomparison study of wind wave predictions models, part 1: Principal results and conclusions, in: Ocean wave modeling; Plenum, New York, 256p.
- Van der Westhuysen, A.J., M. Zijlema, J.A. Battjes, 2007, Nonlinear saturationbased whitecapping dissipation in SWAN for deep and shallow water, *Coastal Eng.,* 54, 151 – 170.
- WAMDI group: S. Hasselmann, K. Hasselmann, E. Bauer, P.A.E.M. Janssen, G.J. Komen, L. Bertotti, P. Lionello, A. Guillaume, V.C. Cardone, J.A. Greenwood, M. Reistad, L. Zambresky and J.A. Ewing, 1988, The WAM model – a third generation ocean wave prediction model, *J. Phys. Oceanogr.,* 18, 1775 – 1810.
- WL & Alkyon, 2007, *Sensitivity analysis of SWAN for the Amelander Zeegat,* Alkyon, WL Delft Hydraulics Report H4918.41 pp. 211.
- Zijlema, M., and A.J. van der Westhuysen, 2005, On convergence behaviour and numerical accuracy in stationary SWAN simulations of nearshore wind wave spectra, *Coastal Eng.* 52, 237 – 256.

Part II:

Depth-induced breaking:

A comparison on the performance of three models

Contents

Abstract

Depth-induced breaking is a subject that has been widely studied, resulting in many scalings on the Battjes and Janssen model. The Battjes and Janssen model, the biphase scaling and the Nelson scaling were selected to compare results in terms of significant wave height. The parameter of interest is the model coefficient γ_{BJ}. The models were tested with the SWAN model on three different test cases; two reef cases and one sloping bottom profile. The wave period appeared to have a strong influence on the prediction of the significant wave height, in particular on the biphase scaling. The best model over the three test cases statistically is the Nelson scaling.

List of symbols

Symbol	Description	Units
B	Proportionality coefficient (O (1))	-
D_{tot}	Total energy dissipation	m^2/s
d	Water depth	m
$\tilde{d}$	Dimensionless water depth	-
E	Wave variance	m^2/s
E_{tot}	Total energy	m^2
$\tilde{E}$	Dimensionless total energy	-
F	Fetch	m
$\tilde{F}$	Dimensionless fetch	-
f_0	Zero-crossing wave frequency	Hz
$\overline{f}_0$	Mean zero-crossing wave frequency	Hz
f_{m01}	Mean wave frequency	Hz
f_p	Peak wave frequency	Hz
$\tilde{f}_p$	Dimensionless peak wave frequency	-
g	Gravitational acceleration (= 9.81)	m/s^2
H_{br}	Critical height of the breaking wave	m
$H_{\max}$	Maximum wave height	m
H_{m0}	Significant wave height; determined from wave spectrum	m
$H_{m0,obs,i}$	Observed significant wave height of component i	m
$H_{m0,SWAN,i}$	Computed significant wave height of component i	m
H_{rms}	Root-mean-squared wave height	m
$H_{s,i}$	Incoming significant wave height	m
h_t	Water depth on reef-plateau	m
n	Calibration parameter in biphase scaling	-

	$(= 2.4)$	
Q_b	Fraction of broken waves	-
T_{m01}	Mean wave period	s
$T_{p,i}$	Incoming wave peak period	s
U_{10}	Wind speed at 10 m altitude	m/s
U_r	Ursell number	-
$W_i(H)$	Weighting function (for $i = 1,2,3$)	-
α_{BJ}	Proportionality coefficient	-
β	biphase	-
β_{ref}	Biphase at which all waves are considered to be broken$\left(= -\pi/2\right)$	-
γ_{BJ}	Model coefficient (Battjes & Janssen)	-
γ_N	Model coefficient (Nelson)	-
γ_{TG}	Model coefficient (Thornton & Guza)	-
φ_n	Phase of wave component n	-
ψ	Bottom slope	-

1 Introduction

The SWAN model (Booij *et al.* 1999) is based on the spectral wave action balance equation.

$$\frac{\partial N(\sigma,\theta;x,y,t)}{\partial t}+\frac{\partial c_{g,x}N(\sigma,\theta;x,y,t)}{\partial x}+\frac{\partial c_{g,y}N(\sigma,\theta;x,y,t)}{\partial y}+\ldots$$
$$\ldots\frac{\partial c_{\theta}N(\sigma,\theta;x,y,t)}{\partial \theta}+\frac{\partial c_{\sigma}N(\sigma,\theta;x,y,t)}{\partial \sigma}=\frac{S(\sigma,\theta;x,y,t)}{\sigma} \qquad (1.1)$$

The terms on the left hand side in the equation represent, respectively, the rate of change of action density in time, the propagation in x-direction, y-direction, directional space (θ) and frequency space (σ). On the right hand side in the equation are the different source terms that represent the generation by wind (S_{in}), quadruplet wave-wave interactions (S_{nl4}), white capping (S_{wc}), bottom friction (S_{bfr}), triad wave-wave interactions (S_{nl3}) and depth-induced breaking (S_{surf}). This part of the study will aim on depth-induced breaking, and in particular the model coefficient γ_{BJ}.

Part I was about the time scales of the different wave processes in a tidal inlet. The area of interest was the Amelander Zeegat. Part II is about one wave process in particular: Depth-induced wave breaking. Depth-induced breaking of waves is a complex phenomenon, which despite being extensively studied, is still poorly understood. This complicates the prediction of the significant wave height at finite depths.

Since 2003, the Dutch ministry of Transport and Public Works has set up a wave observation programme to gain insight in the

performance of the SWAN model. Hind cast studies on the Waddenzee area based on data obtained from this programme (Groeneweg *et al.* 2008; Van Vledder *et al.* 2008) have shown that the SWAN model underestimates wave heights and wave periods in the Waddenzee interior. From these studies it also follows that the ratio between the significant wave height and the water depth H_{m0}/d appears to have an upper limit of about 0.38, whereas observations indicate values as high as 0.43.
Further analysis of the observations and model results show that the Waddenzee interior is shielded against the waves approaching from the North Sea by the barrier islands and the ebb tidal deltas in front of the tidal inlets. These waves hardly penetrate the Waddenzee interior. Therefore, waves in the Waddenzee interior are mostly generated locally.

The underestimation of the prediction of the significant wave height and wave period in the SWAN model is addressed in Van der Westhuysen (2009).

The model for depth-induced breaking proposed by Battjes and Janssen (1978) is implemented in the SWAN model and has been very successful in a variety of cases. In the Battjes and Janssen model the total dissipation of energy is proportional to the fraction of broken waves Q_b, which is difficult to estimate. To estimate the Q_b a cumulative Rayleigh distribution, truncated at $H = H_{\max}$, is used. In shallow water the maximum wave height depends on the water depth and the breaker index γ_{BJ}.
Thornton and Guza (1983) proposed another scaling on the fraction of broken waves. They determined the distribution of breaking waves. This distribution can be expressed as the distribution of all waves (non-broken and broken) multiplied with a weighting function.

The area under the distribution of breaking waves is equal to the fraction of broken waves.

Various scalings of coefficients in the Battjes and Janssen model were proposed, mostly for sloping bottom profiles. scalings for (nearly) horizontal bottom profiles are very limited in number.
The main parameter of interest in the scalings was the model coefficient γ_{BJ}. Battjes and Janssen originally proposed a constant for γ_{BJ}. Subsequent studies suggested dependencies of γ_{BJ} on, for example, the offshore wave steepness s_0 (Battjes and Stive 1985; Nairn 1990), a normalised dissipation rate (Holthuijsen and Booij 2006), the offshore wave height H_0 and the inverse Iribarren parameter $1/\xi$ (Apotsos *et al.* 2008) and the dimensionless water depth kh (Ruessink *et al.* 2003).

Nelson (1987, 1994) proposed a scaling of the model coefficient γ_{BJ} that depends on the bottom slope. The breaker index varies from 0.55 to 0.81 for horizontal to near-horizontal (slope 1:100) bottom profiles, respectively. For steeper slopes the Nelson scaling is clipped at a value of 0.81, because for these steep slopes the value for the model coefficient would become to large to properly describe measurements performed earlier by Nelson (1987).

Van der Westhuysen proposed a scaling of the Thornton and Guza model (1983). This scaling is based on the shallow water non-linearity of the wave field; the biphase. This scaling is called the biphase scaling and gave promising results on finite depth cases and values for the ratio H_{m0}/d also improved.

This study will investigate whether the Battjes and Janssen model, the biphase scaling and the Nelson scaling are able to give good

results for various test cases (Jensen 2002; Smith 2004; Hardy and Young 1996), which differ from the test cases used by Van der Westhuysen (2009). This will be done by comparing results from computations with the SWAN model with measurements of the significant wave height obtained from the various test cases. The aim is to find which of the three selected models gives the best overall results.

To investigate whether the three models are able to perform well in depth-limited wave growth situations, the growth curves are compared with the observed growth curve by Young and Verhagen (1996a).

The test cases selected for this study, consist of two cases performed on reef situations (Jensen 2002; Hardy and Young 1996) and one case with a sloping bottom profile (Smith 2004).

Secondarily, this study will investigate the effect that other shallow water wave processes (triad wave-wave interactions and bottom friction) have on depth-induced breaking, and with that, on the prediction of the significant wave height. Besides the default run (all shallow water processes taken into account), three additional tests are performed, in which the triad wave-wave interactions and bottom friction are in turn ignored or taken into account.

This second part of the thesis is structured as follows: Chapter 2 presents the method used in this study, including the applied wave breaking models, the case selection, the model settings and the performed tests. Chapter 3 gives the results of the applied wave breaking models. Chapter 4 presents a discussion on the results of this study. Chapter 5 closes this thesis with conclusions.

2 Method

The aim of this study is to compare the performance of three depth-induced wave breaking models and find the one that gives the best overall results in terms of the significant wave height $\left(H_{m0}\right)$ on various test cases. The investigated models are:

- Battjes and Janssen model (1978)
- Biphase scaling (van der Westhuysen 2009)
- Nelson scaling (Nelson 1994)

These models are addressed in Section 2.1. In Section 2.2 the various test cases are presented in detail. The depth-limited wave growth of the three models is addressed in Section 2.3. The model settings are presented in Section 2.4 and this chapter closes with Section 2.5 that presents four tests with the purpose to gain some insight in the additional shallow water wave processes (bottom friction, triad wave-wave interactions).

2.1 Models for depth-induced breaking

2.1.1 Battjes and Janssen

The Battjes and Janssen model (1978) is a widely accepted model for depth-induced wave breaking. It is based on the dissipation of energy in a bore. The dissipation of a single breaking wave is analogous to that of a bore and is described as:

$$D_{wave} = -\tfrac{1}{4}\alpha_{BJ}\rho g f_0 H_{br}^2 \tag{2.1}$$

Where α_{BJ} is a proportionality coefficient of the $O(1)$, f_0 is the zero-crossing wave frequency and H_{br} is the height of the breaking wave.
This description accounts for a single breaking wave. For a random wave field this parameter becomes a random variable. The expected value can be described as:

$$\bar{D}_{wave} = E\left\{\underline{D}_{wave}\right\} = -\tfrac{1}{4}\alpha_{BJ}\rho g\int_0^\infty\int_0^\infty f_0 H_{br}^2 df_0 dH_{br} \tag{2.2}$$

The average of all breaking and non-breaking waves is:

$$\bar{D}_{surf} = Q_b\bar{D}_{wave} \tag{2.3}$$

In which Q_b is the fraction of breaking waves. Battjes and Janssen (1978) found that the $\int_0^\infty\int_0^\infty f_0 H_{br}^2 df_0 dH_{br}$ could be replaced by $\overline{f}_0 H_{\max}^2$, giving:

$$\bar{D}_{surf} = -\tfrac{1}{4}\alpha_{BJ}\rho g Q_b\overline{f}_0 H_{\max}^2 \tag{2.4}$$

To express the total dissipation in terms of variance density equation 2.4 must be divided by ρg.
The maximum wave height $H_{\max}$ is described by a modified Miche expression.

$$H_{\max} = \frac{0.88}{k_p}\tanh\left(\gamma_{BJ}\frac{k_p d}{0.88}\right) \tag{2.5}$$

In which k_p is the peak wave number of the spectrum. For this expression two limit states can be defined: For deep water $\left(k_p d \to \infty\right)$ equation 2.5 reduces to $H_{\max} = 0.88/k_p$ and for shallow

water $\left(k_p d \to 0\right)$ equation 2.5 reduces to $H_{\max} = \gamma_{BJ} d$. Since shallow water test cases are used, this expression is applied.

To determine the local fraction of broken waves Q_b, Battjes and Janssen assume that all waves can be described with a cumulative Rayleigh distribution, truncated at $H = H_{\max}$. This leads to the following implicit expression for Q_b:

$$\frac{1 - Q_b}{-\ln Q_b} = \left(\frac{H_{rms}}{H_{\max}}\right)^2 \tag{2.6}$$

In which H_{rms} is the root-mean-square wave height.

2.1.2 The biphase scaling

The biphase is a characteristic of the wave field and is also used in the description of the triad wave-wave interactions. The required triad resonance conditions can only satisfy in very shallow water since waves in shallow water are non-dispersive. The resonance conditions are:

$$\begin{aligned} f_1 + f_2 &= f_3 \\ \vec{k}_1 + \vec{k}_2 &= \vec{k}_3 \end{aligned} \tag{2.7}$$

In somewhat deeper, but still shallow water the resonance conditions are nearly satisfied, so that near-resonance occurs. This results in energy transfer and phase-coupling between the wave components involved. The magnitude of energy transfer depends on the phase differences between the three wave components involved, which are quantified with the biphase $\beta_{1,2}$:

$$\beta_{1,2} = \varphi_1 + \varphi_2 - \varphi_{1+2} \tag{2.8}$$

In which φ_1, φ_2 and $\varphi_{1+2} = \varphi_3$ are the phases of the three interacting wave components.

The philosophy behind the biphase scaling is based on phase resolving wave models. In these models the process of depth-induced breaking is a function of the slope of the front face of a wave. The wave breaks when the slope of the front face exceeds a given value. The steep slope of the front face of a wave is generated by means of shallow water and triad wave-wave interactions, which change the shape of the wave from to a saw-tooth shape. This shifting in shape of the waves is related to the biphase, when it progresses from 0 to $-\pi/2$. This observed behaviour of the biphase for the self-self interaction at the peak frequency can be roughly approximated with:

$$\beta_{f_{peak}} = -\frac{\pi}{2} + \frac{\pi}{2}\tanh\left(\frac{0.2}{U_r}\right) \tag{2.9}$$

This approximation of the biphase is used in the biphase scaling. The biphase depends on the Ursell number U_r and the latter is given as:

$$U_r = \frac{g}{8\sqrt{2}\pi^2}\frac{H_s T_{m01}^2}{d^2} \tag{2.10}$$

As described in Section 3.3.5 of Part I the saw tooth shaped waves occur in shallow water where the biphase approaches $-\pi/2$ (Eldeberky 1996).
The biphase scaling is a scaling of the model proposed by Thornton and Guza (1983), which in turn is a scaling of the model proposed by Battjes and Janssen (1978). Thornton and Guza proposed that all waves can be described with a cumulative Rayleigh distribution that

is not truncated at a certain value. The total dissipation of energy due to breaking waves can then be described as:

$$D_{tot} = -\frac{B^3 f_{m01}}{4d} \int_0^\infty H^3 p_b(H)\, dH \tag{2.11}$$

In which B is a proportionality coefficient and $p_b(H)$ the breaking wave distribution. The area under this distribution is equal to the fraction of breaking waves. The distribution $p_b(H)$ is obtained by multiplying the probability density function of the Rayleigh distribution with a weighting function.

$$p_b(H) = p(H) W(H) \tag{2.12}$$

In which *p(H)* is the probability density function of the Rayleigh distribution, given by:

$$p(H) = \frac{2H}{H_{rms}^2} \exp\left[-\left(\frac{H}{H_{rms}}\right)^2\right] \tag{2.13}$$

In Thornton and Guza (1983) two versions of the weighting function were proposed. In the first, $W_1(H)$, it is assumed that the waves break in proportion to the distribution for all waves. In the second, $W_2(H)$, based on observations, the weighting function weights more heavily on the larger waves.

$$W_1(H) = \left(\frac{H_{rms}}{\gamma_{TG} d}\right)^n \quad \text{and} \quad W_2(H) = \left(\frac{H_{rms}}{\gamma_{TG} d}\right)^n \left[1 - \exp\left(-\left(\frac{H_{rms}}{\gamma_{TG} d}\right)^2\right)\right] \tag{2.14}$$

In which n is a calibration coefficient and γ_{TG} is the breaker index from Thornton and Guza (1983).

Van der Westhuysen (2009) proposed a different weighting function, which depends on the biphase.

$$W_3(H) = \left(\frac{\beta}{\beta_{ref}}\right)^n \tag{2.15}$$

In which β_{ref} and n are calibration coefficients. The coefficient β_{ref} indicates the value at which all waves are assumed to have broken. In van der Westhuysen (2009) this coefficient was chosen to a value of $-\pi/2$.

2.1.3 Nelson scaling

Nelson (1987, 1994) proposed a scaling for the model coefficient γ_{BJ} from the Battjes and Janssen model. For horizontal bottom profiles he found an upper limit for the model coefficient of 0.55. Also, he proposed an upper limit for the model coefficient for very flat slopes. This scaling of the model coefficient is valid for bottom profiles with slopes from 0.01 to horizontal. (Note that in the work of Nelson [1994, equation (4)] the constant 0.88 is missing in the expression of R. Nelson)

$$\gamma_N = \left[\frac{H}{h}\right]_{\max} = 0.55 + 0.88\exp\left(-0.012\cot(\psi)\right) \tag{2.16}$$

In which ψ is the bottom slope. The model coefficient will vary from approximately 0.55 to 0.81 for a horizontal bottom and a slope of 0.01 respectively.
This scaling was previously studied by Ris (1997) and Booij *et al.* (1999). Ris (1997) found that for sloping bottom profiles steeper than the 1:100 the γ_N does not fit measurements performed earlier by

Nelson (1987). Therefore the Nelson expression is clipped at $\gamma_N = 0.81$ for slopes steeper than 1:100. Ris also found that for sloping bottom profiles the Nelson scaling slightly overestimates the wave height. For that reason he used a $\alpha_{BJ} = 1.5$. In this study $\alpha_{BJ} = 1.0$ is used.

2.2 Depth-limited wave growth

Depth-limited wave growth of the three wave breaking models addressed earlier is investigated in this section. Growth curves, produced by the models are compared with the formulations of Young and Verhagen (1996a) to observe whether the Battjes and Janssen model, the biphase scaling and the Nelson scaling follow the growth curve.

To compare the results from the models and the observations dimensionless parameters are used. The water depth d, total wave energy E_{tot} and peak wave frequency f_p are scaled with the wind speed U_{10}. These scaled parameters are given by equation 2.17.

$$\tilde{d} = \frac{gd}{U_{10}^2} \quad , \quad \tilde{E} = \frac{g^2 E_{tot}}{U_{10}^4} \quad ; \quad \tilde{f}_p = \frac{f_p U_{10}}{g} \tag{2.17}$$

In which $\tilde{d}, \tilde{E}$ and $\tilde{f}_p$ are the dimensionless versions of the water depth, total energy and peak frequency, respectively and g is the gravitational acceleration. These dimensionless parameters are compared with the expressions by Young and Verhagen. In their general form:

$$\tilde{E} = 3.64 \cdot 10^{-3} \left(\tanh A_1 \tanh \left[\frac{B_1}{\tanh A_1} \right] \right)^{1.74} \tag{2.18}$$

where

$$A_1 = 0.493\tilde{d}^{0.75} \tag{2.19}$$

$$B_1 = 3.13 \cdot 10^{-3}\,\tilde{F}^{0.57} \tag{2.20}$$

and

$$\tilde{f}_p = 0.133\left(\tanh A_2 \tanh\left[\frac{B_2}{\tanh A_2}\right]\right)^{-0.37} \tag{2.21}$$

where

$$A_2 = 0.331\tilde{d}^{1.01} \tag{2.22}$$

$$B_2 = 5.215 \cdot 10^{-4}\,\tilde{F}^{0.73} \tag{2.23}$$

In which $\tilde{F}$ is the dimensionless fetch, described as $\tilde{F} = gF/U_{10}^2$. For infinite fetch B_1 and B_2 become infinitely large and therefore equation 2.18 and 2.21, with substituted A_1 and A_2, reduce to:

$$\tilde{E} = 3.64 \cdot 10^{-3}\left(\tanh\left[0.493\tilde{d}^{0.75}\right]\right)^{1.74} \tag{2.24}$$

and

$$\tilde{f}_p = 0.133\left(\tanh\left[0.331\tilde{d}^{1.01}\right]\right)^{-0.37}. \tag{2.25}$$

Computations with SWAN version 40.72AB have been carried out for several depths d (0.625 m, 1.25 m, 2.5 m, 5 m, 10 m, 20 m, 40 m, 80 m, 160 m and 320 m) and a wind speed of $U_{10} = 20\,\mathrm{m/s}$ for infinite fetch. The spatial resolution was increased with every increase of the water depth with the purpose to save on calculation time. This, because of the fact that waves in larger water depths can become higher than waves in smaller water depth and therefore take longer

to grow to their maximum height. By increasing the spatial resolution a considerable amount of time is saved. Also, when looking for the growth curve at infinite fetch, only the fully grown wave height at the different water depths is of interest. It is not interesting to know how the wave growth is along the fetch and for that reason the spatial resolution at large depths can be increased.
The observed growth curve of Young and Verhagen (1996a) and the growth curves for the different models are shown in Figure 2-1.

Looking at Figure 2-1 it can be seen that from the encircled point (see left panel of Figure 2-1) in the growth curve and higher, the effect of depth-induced wave breaking on the depth-limited wave growth becomes irrelevant, because the wave height over water depth ratio becomes very small; consequently the difference between the models is non-existent.

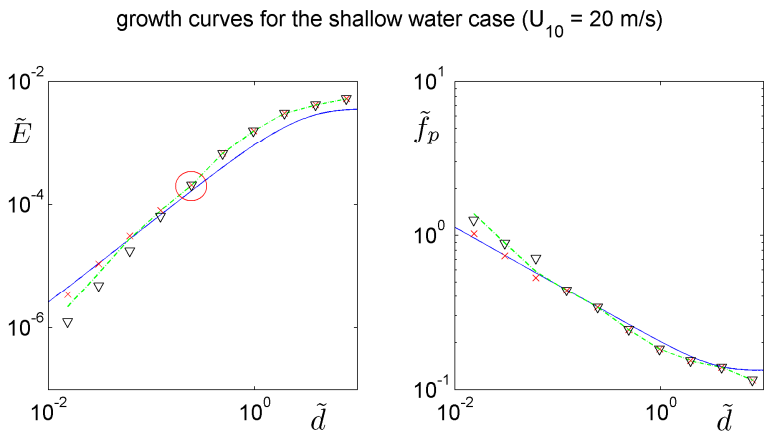

Figure 2-1: Shallow water growth curves of dimensionless total energy $\tilde{E}$ (left figure) and peak frequency $\tilde{f}_p$ (right figure) as a function of dimensionless depth $\tilde{d}$ at infinite fetch. (——) formulations of Young and Verhagen (1996a), (------) SWAN results from the Battjes Janssen, (×××) SWAN results from the biphase scaling, (▽▽▽) SWAN results from the Nelson scaling.

In shallower water the differences between the models become apparent, which is visible in Figure 2-1. Nelson predicts the lowest values whereas the biphase scaling gives the highest results, which are closest to the growth curve observed by Young and Verhagen (1996a).
The models have an influence over the range of smallest dimensionless depths. Here the biphase scaling yields the best results, the Nelson scaling the poorest.

2.3 Data setup

In this section tests of two flume cases (Smith 2004; Jensen 2002) and one field case (Hardy and Young 1996) are presented.

2.3.1 Smith

Smith (2004) performed laboratory experiments at the US Army Engineer Research and Development Center, coastal and Hydraulics Laboratory. The setup is shown in Figure 2-2.

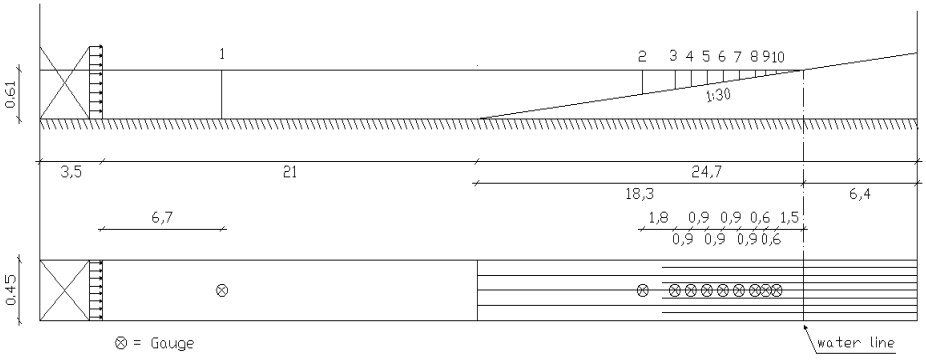

Figure 2-2: Setup experiment Smith (2004). Units are in meters.

The flume was 45.7 m long and 0.45 m wide. The flume had a slope of 1:30 that began at 21 m from the wave paddle. In the flume 10 gauges were placed. The water depths at these gauges 1 to 10 are 0.61 m, 0.30 m, 0.24 m, 0.21 m, 0.18 m, 0.15 m, 0.12 m, 0.09 m and 0.05 m respectively. The generated irregular waves were of the TMA spectral shape (Bouws *et al.*), for both single-peak spectra and the linear combination of two TMA spectra for double-peak spectra. The TMA spectrum is an alteration of the JONSWAP spectrum and can be used from deep water to arbitrary depth situations. This alteration means that as waves move from deep water to shallow water the spectral f^{-5}-shape is being slowly replaced by the f^{-3}-shape, which better describes the high-frequency tail in shallow water.

The peak periods $\left(T_p\right)$ varied from 1 s to 2.5 s and the significant wave height $\left(H_{m0}\right)$ were 0.06 m or 0.09 m. In the double-peaked spectra the peak period was 1.0 s and contained 2/3 of the total energy. The widths of the spectra were also varied by using 3 different values for the spectral peakedness parameter (γ). For a broad spectrum $\gamma = 3.3$, for a narrow spectrum $\gamma = 100$ and for a spectrum with an intermediate shape $\gamma = 20$ was used.

In total there were 31 runs which are presented in Table 2-1.

Runs	Peak 1 $\left(T_p\right)$ $[s]$	Peak 2 $\left(T_p\right)$ $[s]$	H_{m0} $[m]$	γ
1	2.5	1.0	0.09	20
2	2.0	1.0	0.09	20
3	1.75	1.0	0.09	20
4	1.5	1.0	0.09	20
5	1.25	1.0	0.09	20
6	2.0	-	0.09	20
7	1.5	-	0.09	20
8	1.0	-	0.09	20
9	1.25	1.0	0.06	20
10	1.5	1.0	0.06	20
11	1.75	1.0	0.06	20
12	2.0	1.0	0.06	20
13	2.5	1.0	0.06	20
14	1.25	1.0	0.09	3.3
15	1.75	1.0	0.09	3.3
16	2.5	1.0	0.09	3.3
17	1.25	1.0	0.09	100
18	1.75	1.0	0.09	100
19	2.5	1.0	0.09	100
20	1.0	-	0.09	3.3
21	1.0	-	0.09	20
22	1.0	-	0.09	100
23	1.25	-	0.09	3.3
24	1.25	-	0.09	20
25	1.25	-	0.09	100
26	1.75	-	0.09	3.3
27	1.75	-	0.09	20
28	1.75	-	0.09	100
29	2.5	-	0.09	3.3
30	2.5	-	0.09	20
31	2.5	-	0.09	100

Table 2-1: 31 runs from the experiment from Jane Mckee Smith (2004)

2.3.2 Jensen

The setup for this experiment, which was performed by Jensen (2002), is presented in Figure 2-3. The experiment focussed on wave predictions on a reef.

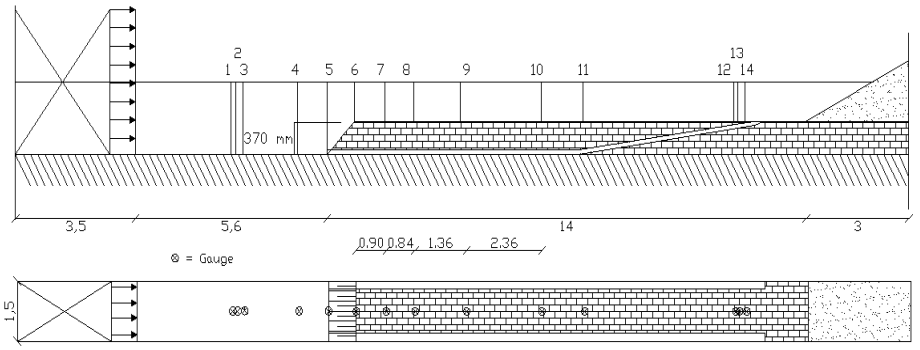

Figure 2-3: Setup experiment Jensen (2002) with a 1:1 slope. Units are in meters.

The flume was 1.5 m wide and approximately 26 m long including the wave paddle and the absorption area. The wave paddle is situated on the far left of the flume and is drawn as the cross with the arrows pointing to the right, whereas the absorption area is situated on the far right of the flume. The bottom of the reef slope is situated 5.6 m from the wave paddle. Jensen used four different slopes for his experiment, 1:1, 1:2, 1:0.5 and 1:1-S. This 1:1-S slope is a 1:1 slope but with a rounded base and top, resulting in an S-shape bottom profile. The slopes used to test the three models are the 1:1 and 1:2 slopes.

In the flume 14 gauges were placed, five in front of the slope and nine behind it (see Figure 2-3). Presented are the observations from gauge 6 to gauge 10, because energy dissipation due to depth-induced breaking occurs here. In front of the reef (gauges 1 to 5) the waves are not affected by the reef and after gauge 10 the waves have become stable again but are much lower due to the energy dissipation of the breaking waves.

Gauge 6 is situated on the reef-crest and gauge 7, 8, 9 and 10 lie on the reef-plateau at 0.90 m, 1.74 m, 3.10 m and 5.46 m from the reef-crest respectively.

The water depth on the reef-plateau $\left(h_t\right)$ for all slopes was 0.205 m or 0.275 m. In the experiments a JONSWAP spectrum was used with an incoming significant wave height $\left(H_{s,i}\right)$ and incoming wave peak period $\left(T_{p,i}\right)$ varying from 0.13 m to 0.21 m and from 1.4 s to 2.4 s respectively. This resulted in a total of 110 tests.

From these 110 tests a selection of tests was made to use in this study. The philosophy behind this selection is to have a sufficiently wide variation of $H_{s,i}$ and $T_{p,i}$. The maximum and minimum $H_{s,i}$ with the median of $T_{p,i}$ were selected. Also the maximum and minimum $T_{p,i}$ with the median of $H_{s,i}$ were selected. This selection was done per different slope and different water depth on the reef-plateau. For example: for a slope of 1:1 and a $h_t = 0.205\,\mathrm{m}$, the value for the median of $H_{s,i}$ and $T_{p,i}$ are 0.16 m and 1.8 s respectively. First, the minimum and maximum wave height for this slope and h_t are 0.13 m and 0.21 m, respectively, while the wave period is kept constant at 1.8 s. Secondly, the wave height is kept constant and the minimum and maximum wave period are 1.4 s and 2.2 s, respectively. This selection process results in 5 tests per slope and h_t.

For a 1:2 slope and a $h_t = 0.275\,\mathrm{m}$ only 5 tests were done by Jensen (2002) and were therefore all selected.

Table 2-2 presents the selection of tests described above and the corresponding observations performed by Jensen.

					G. 6	G. 7	G. 8	G. 9	G. 10
Experiment	slope	h_t (m)	$H_{s,i}$ (m)	$T_{p,i}$ (s)	H_{m0} (m)	H_{m0} (m)	H_{m0} (m)	H_{m0} (m)	H_{m0} (m)
Test 1	1:1	0.205	0.13	1.8	0.142	0.104	0.086	0.075	0.068
Test 2	1:1	0.205	0.16	1.4	0.140	0.097	0.082	0.074	0.072
Test 3	1:1	0.205	0.16	1.8	0.164	0.111	0.090	0.077	0.070
Test 4	1:1	0.205	0.16	2.2	0.188	0.127	0.103	0.081	0.069
Test 5	1:1	0.205	0.21	1.8	0.210	0.126	0.098	0.079	0.070
Test 6	1:1	0.275	0.13	1.8	0.138	0.122	0.110	0.100	0.093
Test 7	1:1	0.275	0.16	1.8	0.166	0.137	0.121	0.106	0.098
Test 8	1:1	0.275	0.16	2.2	0.168	0.143	0.126	0.108	0.097
Test 9	1:1	0.275	0.19	1.8	0.194	0.150	0.128	0.107	0.096
Test 10	1:2	0.205	0.13	1.8	0.161	0.113	0.092	0.084	0.075
Test 11	1:2	0.205	0.16	1.4	0.155	0.107	0.090	0.085	0.077
Test 12	1:2	0.205	0.16	1.8	0.198	0.125	0.098	0.088	0.076
Test 13	1:2	0.205	0.16	2.2	0.204	0.133	0.107	0.089	0.075
Test 14	1:2	0.205	0.21	1.8	0.230	0.134	0.107	0.088	0.076
Test 15	1:2	0.275	0.13	2.4	0.148	0.130	0.119	0.103	0.098
Test 16	1:2	0.275	0.16	1.4	0.134	0.118	0.106	0.097	0.098
Test 17	1:2	0.275	0.16	2.4	0.190	0.157	0.133	0.113	0.104
Test 18	1:2	0.275	0.19	1.8	0.191	0.147	0.123	0.107	0.102
Test 19	1:2	0.275	0.19	2.4	0.213	0.172	0.142	0.117	0.105

Table 2-2: Selection of tests from the reef-experiment from Morten Sand Jensen (2002)

2.3.3 Hardy and Young

The measurement site used in the study by Hardy and Young (1996) is the John Brewer Reef, which is located 70 km northeast of Townsville, Queensland, Australia. It is situated in the central section of the Great Barrier Reef. The reef has an elliptical shape and the dimensions are 6 by 3 km.

The astronomical tides nearby Townsville are semidiurnal. The highest astronomical tide (HAT) is 3.73 m Low Water Datum (LWD) and lowest astronomical tide (LAT) is -0.28 m LWD. The tidal range at John Brewer Reef is approximately 90% of that of Townsville.

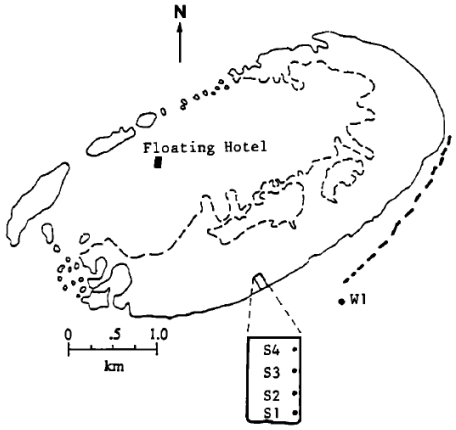

Figure 2-4: John Brewer Reef.

The differences between the highest and lowest water levels were 0.36 m. H_s ranged from 0.5 to 0.85 m. The incident waves were dominated by swell with periods between 12 to 18 s.

In this study this situation is schematised to a 1-D situation. The schematised setup of the field experiment is presented in Figure 2-5.

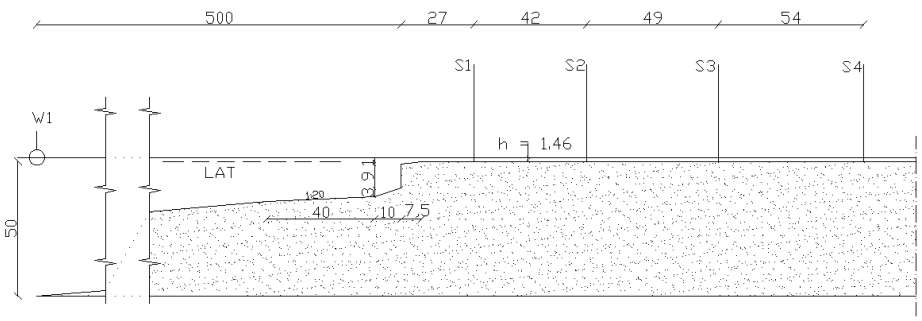

Figure 2-5: Setup field experiment Hardy and Young. Units are in meters

A Waverider buoy recording the offshore wave conditions (indicated with W1 in Figure 2-5) is located about 500 m seaward of the reef front, where the water depth is approximately 50 m. The reef front has an outward directed normal of 135 degrees (North = 0 degrees clockwise). On the reef flat four so-called "Zwarts" poles were placed normally to the reef front. The first one S1 was located 27 m from the reef front. S2, S3 and S4 were located at intervals of 42, 49 and 54 m respectively.

The recorded data set dates from 1 – 22 September 1988. Presented data are the wind speed, wind direction, water depth and the significant wave height at W1, S1, S2, S3 and S4. Also 4 wave spectra measured at W1 are presented.

The spectra measured by the wave rider buoy are presented in Figure 2-6:

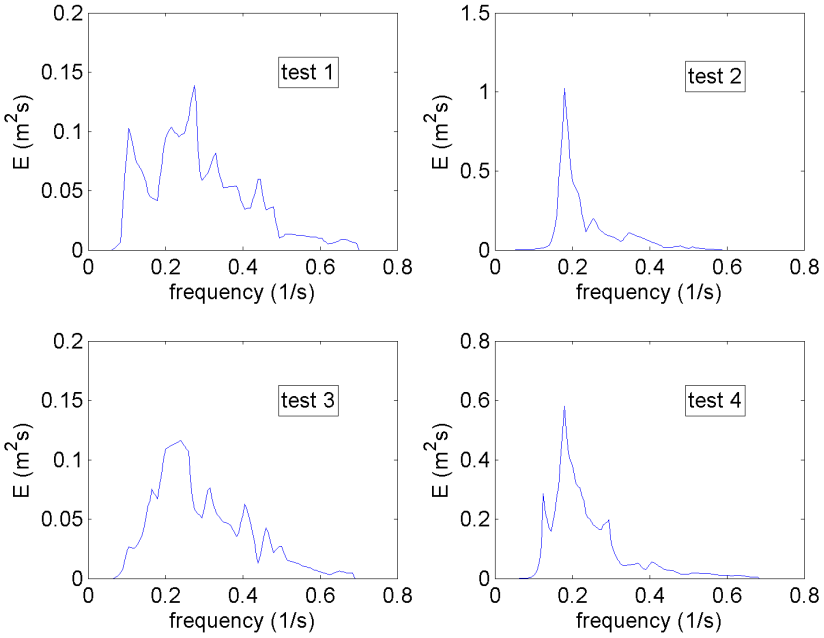

Figure 2-6: Wave spectra at the wave rider buoy for the 4 tests.

The corresponding wind speed and direction and h_t for the test cases are presented in Table 2-3:

	U_{10} [m/s]	θ_{wind} [° North]	h_t [m]
Test case 1	7.9	97	2.48
Test case 2	9.1	154	1.48
Test case 3	7.6	115	0.98
Test case 4	8.5	103	0.45

Table 2-3: 4 tests from the Hardy and Young test case

2.4 Model settings

For all 3 test cases the computational grid had to be constructed. The optimal grid sizes in x-direction and frequency-space had to be determined. Numerous computations were done in which the step

sizes in x-space were systematically reduced until the relative error between the SWAN output of succeeding computations was less than 1%. An identical process was used for the number of frequencies used in the calculations. The number of frequencies $\left(N_f\right)$ was increased until the relative error between the SWAN output of succeeding computations was less than 1%. This was possible since the quadruplet wave-wave interactions were de-activated. The quadruplet wave-wave interactions were de-activated, because the calculations were performed on a limited directional sector. The following grid sizes (dx) and number of frequencies $\left(N_f\right)$ were obtained:

- Jensen (2002): $dx = 0.01$ m; $N_f = 30$,
- Smith (2004): $dx = 0.1$ m; $N_f = 50$,
- Hardy and Young (1996): $dx = 0.1$ m; $N_f = 50$.

The computations were carried out using the SWAN model 40.72AB. Van der Westhuysen (2009) implemented his biphase scaling in an earlier version of SWAN but with a numerical incorrect technique. This scaling was subsequently implemented by Zijlema in the SWAN version mentioned here. In the test cases provided by Jensen and Smith no deep water wave processes as wind input, quadruplet wave-wave interactions and whitecapping were used. For the test cases provided by Hardy and Young, the combination of wind input and saturation-based whitecapping proposed by Van der Westhuysen *et al.* (2007) was used. This choice was arbitrary. As mentioned before the quadruplet wave-wave interactions were de-activated.

The shallow water wave processes used were the bottom friction according to Hasselmann *et al.* (1973) with $c_{f,JON} = 0.067\,\mathrm{m^2 s^{-3}}$ and triad wave-wave interactions according to Eldeberky (1996) both with their default settings in SWAN. For depth-induced wave

breaking the 3 different formulations and their settings were used, which are:

- Battjes and Janssen: $\alpha_{BJ} = 1 \quad ; \quad \gamma_{BJ} = 0.73\,,$
- Biphase scaling: $\beta_{ref} = -\pi/2 \quad ; \quad n = 2.4\,,$
- Nelson: $\alpha_{BJ} = 1 \quad ; \quad \gamma_N = 0.55 + 0.88\exp(-0.012\cot\psi)\,.$

The selected convergence criteria are based on the curvature criteria (Zijlema and Van der Westhuysen 2005). The curvature criteria represent the stopping criterion for the iteration process. This process is stopped when the curvature of the successive computed value of the significant wave height, regarded as a continuous series, reduces below a certain normalised value. In this study this normalised value was set at 0.001. In appendix B three plots are presented in which the convergence behaviour is plotted against the number of iterations; one for each of the three test cases.

2.5 Statistical analysis

As mentioned at the beginning of this chapter, model results are compared with measurements for each test of the test cases mentioned in Section 2.3. Additionally, the predictive ability of the three models is determined with two statistical error measures; the scatter index and the relative bias. The former describes the random + the systematic error and the latter the systematic error. Both measures are determined for the significant wave height and are defined as:

$$SCI_{H_{m0}} = \frac{\sqrt{\frac{1}{N}\sum_{i=1}^{N}\left(H_{m0,obs,i} - H_{m0,SWAN,i}\right)^2}}{\frac{1}{N}\sum_{i=1}^{N} H_{m0,obs,i}} \tag{2.26}$$

and

$$\text{Rel.Bias}_{H_{m0}} = \frac{\sum_{i=1}^{N}\left(H_{m0,SWAN,i} - H_{m0,obs,i}\right)}{\sum_{i=1}^{N} H_{m0,obs,i}} \tag{2.27}$$

2.6 Additional tests

As a small additional study four calculation tests are done with the SWAN model. The purpose of these tests is to see how two shallow water wave processes (bottom friction and triad wave-wave interactions) influence the prediction of the significant wave height.

Bottom friction, according to Hasselmann (1973) with $c_{f,JON} = 0.067\,\text{m}^2\text{s}^{-3}$ is included since in shallow water conditions this wave process can be dominant. According to Nelson (1994) and Hardy and Young (1996), bottom friction on the reef plateau is very important. However, it is expected that in the provided test cases (see Section 2.3.1 to 2.3.3) bottom friction is not the most dominant wave process.

Triad wave-wave interactions, according to Eldeberky (1996), are included because it is expected that they have influence on the biphase scaling, since the biphase is used in this model. This is also the characteristic of the triad wave-wave interactions. It is expected to have influence on the biphase scaling because this model uses the Ursell number, which depends on the mean wave period (T_{m01}).

The tests can be summarised as follows:

- Depth-induced wave breaking
  - with triad wave-wave interactions
  - with bottom friction,
- Depth-induced wave breaking
  - with triad wave-wave interactions
  - without bottom friction,
- Depth-induced wave breaking
  - without triad wave-wave interactions
  - with bottom friction,
- Depth-induced wave breaking
  - without triad wave-wave interactions
  - without bottom friction

These tests are performed on the 19 test cases provided by Jensen (2002), 4 characteristic test cases from Smith (2004) and 4 test cases provided in Hardy and Young (1996).

3 Results

In this chapter an overview will be given of the results of the test cases obtained from the SWAN computations. The results of the test cases will be presented in different sections, starting with Smith (2004) in Section 3.1, followed by Jensen (2002) in Section 3.2 and lastly Hardy and Young (1996) in Section 3.3.
All results will be given in the appendices. Only the figures that show clear differences from the general appearance are given in the sections below.

3.1 Results Smith test case

In the Smith test case (2004) the effect of the incoming significant wave height on the prediction of H_{m0} is not noticeable. Also the shape of the incoming TMA spectra (unimodal or bimodal) is not of importance. The parameters that do have an influence on the prediction of H_{m0} are T_p and the spectral peakedness parameter γ (see Figure 3-1). When T_p increases the prediction of H_{m0} generally gets better. The biphase scaling appears to be very sensitive to T_p. For $T_p = 1.75\,\text{s}$ the results of the biphase scaling are very good. However, when $T_p \geq 1.75$ the biphase scaling appears to dissipate too much energy, whereas when $T_p \leq 1.75\,\text{s}$ too little energy is dissipated. This effect is not visible for the Battjes and Janssen model and the Nelson scaling. In Figure 3-1 the effect of T_p and the spectral peakedness parameter γ is shown. Tests 20, 22, 29 and 31 are shown in Figure 3-1, because these include the minimum and maximum T_p as well as the minimum and maximum spectral peakedness parameter γ.

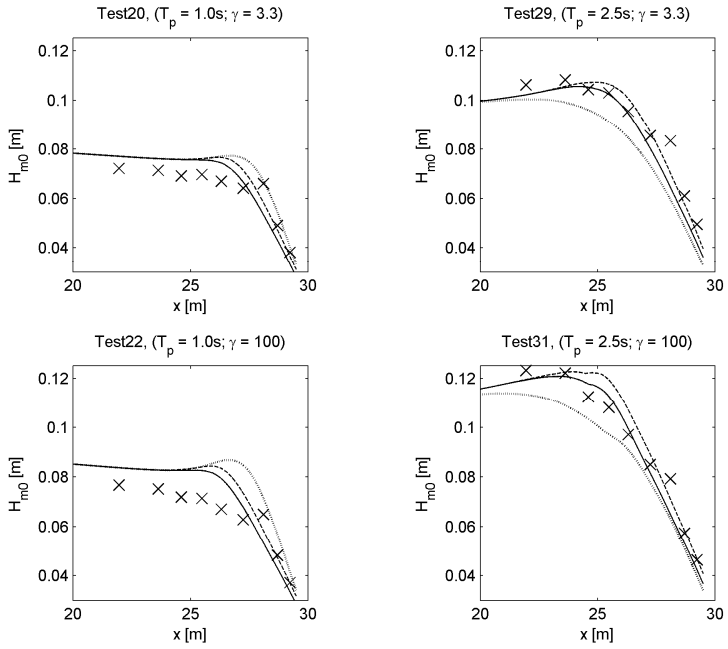

Figure 3-1: Results from tests 20, 22, 29 and 31 from the Smith (2004) test case. (——) SWAN results from the Battjes Janssen, (·····) SWAN results from the biphase scaling, (------) SWAN results from the Nelson scaling. In this figure the effect of the peak period and the spectral peakedness parameter γ is shown.

The spectral peakedness parameter is another point of interest. There is a noticeable increase of the predicted wave height with an increasing γ at approximately 26 - 27 m (see Figure 3-1). This does not affect the prediction of the wave heights for larger T_p.

3.2 Results Jensen test case

For most of the tests selected from Jensen (2002) the results of the biphase scaling differ the most from the measurements followed by the results of the Battjes and Janssen model, whereas the Nelson scaling gives the best results (see Figure 3-2).

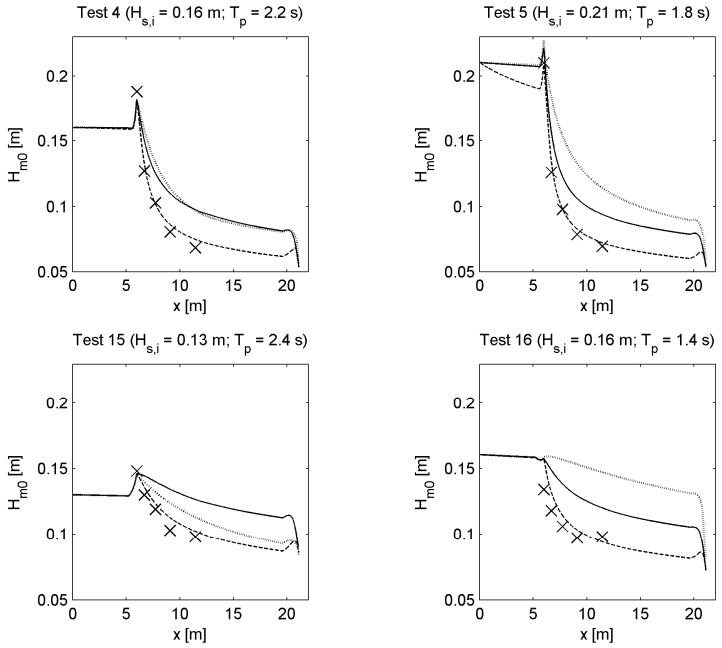

Figure 3-2: Results from tests 4, 5, 15 and 16 from the Jensen (2003) test case. (——) SWAN results from the Battjes Janssen, (·····) SWAN results from the biphase scaling, (------) SWAN results from the Nelson scaling.

However, in tests 15 and 17 the biphase scaling gives better results than the Battjes and Janssen model (see lower left panel of Figure 3-2) and in tests 4, 8 and 19 the lines, representing the results of the biphase scaling and the Battjes and Janssen model, cross each other (see upper left panel of Figure 3-2). These are all tests with a T_p larger than 2.2 s.

In tests 2, 11 and 16, there is a very small reduction in H_{m0} before H_{m0} peaks on the front of the reef (see lower right panel of Figure 3-2). This only occurs in the tests with $T_p = 1.4\,\mathrm{s}$. The Nelson scaling shows a reduction in the prediction of H_{m0} before the reef in tests 5 and 14 (see upper right panel of Figure 3-2), whereas the other two models do not.

For the biphase scaling the effect of T_p on the prediction of H_{m0} is clearly visible in Figure 3-2, especially in the lower right panel.

3.3 Results Hardy and Young test case

The results of the tests in this test case are somewhat divergent. Some tests give reasonable results whereas others do not. The results of test 1 (see Figure 3-3) show no strong reaction to the reef front. The computed wave heights are much higher than the measurements and show no rapid dissipation.

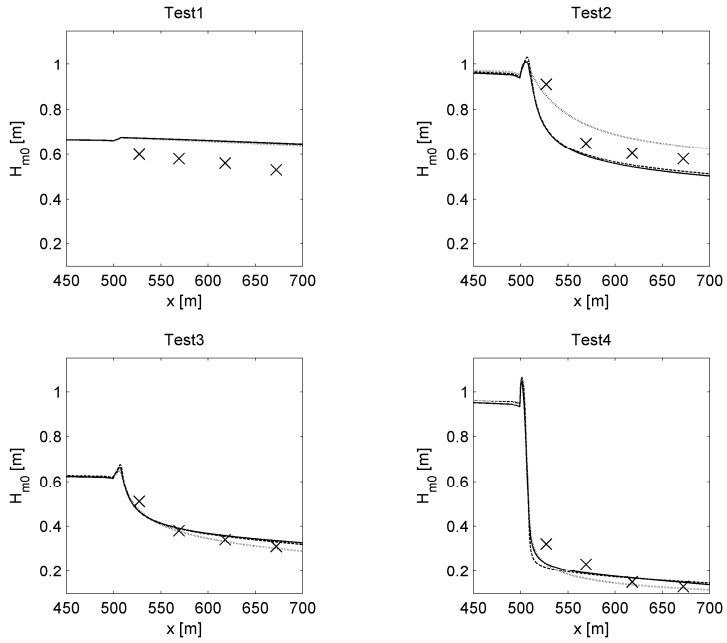

Figure 3-3: Results from the tests of the Hardy and Young (1996) test case. (——) SWAN results from the Battjes Janssen, (·····) SWAN results from the biphase scaling, (-----) SWAN results from the Nelson scaling.

In contrast to the results of test 1, the results of tests 2, 3 and 4 do show a strong reaction to the reef front. H_{m0} increases rapidly once it

hits the reef front and decreases rapidly right after. For this reason the results are more realistic and therefore better. However, in test 2 there is a very noticeable difference between the models (see Figure 3-3). The biphase scaling gives results that are approximately 10 cm ($\approx 15\%$) higher than the measurements, whereas the Battjes and Janssen model and the Nelson scaling give results that are approximately 10 cm lower than the measurements.
The results of the three models are very close to each other and to the measurements in both test 3 and 4 (see Figure 3-3). In test 3 the biphase scaling gives the best results whereas in test 4 the best results are given by the Battjes and Janssen model.

3.4 Results additional tests

Looking at Figure 3-4, the effect on the prediction of H_{m0} by de-activating the bottom friction and triad wave-wave interactions is most evident for the biphase scaling. Considering the results from Jensen (upper panel in Figure 3-4) and Hardy and Young (lower panel in Figure 3-4), the predicted H_{m0} is much lower with the triad wave-wave interactions de-activated than when they are active. For the Battjes and Janssen model and the Nelson scaling the effect of the triad wave-wave interactions is much less.
The effect of the bottom friction is similar for all models. When the bottom friction is active the predicted H_{m0} is a little lower than when de-activated.
Since the effect is the same on all the tests only one test for each test case is presented.

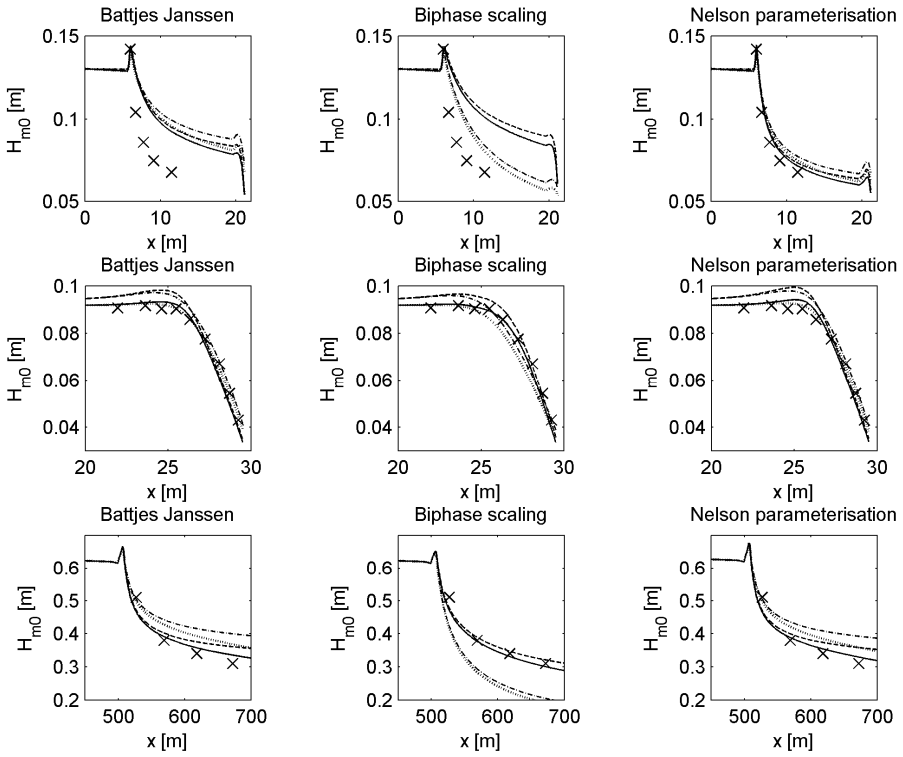

Figure 3-4: Results from the additional tests. The top panels represent test 1 from Jensen (2002), the middle panels represent test 1 from Smith (2004) and the lower panels represent test 3 from Hardy and Young (1996). (——) Bottom friction and triad wave-wave interactions active, (-----) triad wave-wave interactions active; bottom friction de-activated. (·····), bottom friction active; triad wave-wave interactions de-activated, (-·-·-) bottom friction and triad wave-wave interactions de-activated.

4 Discussion

From the Jensen (2002) test case it can be seen that the breaker index as proposed by Nelson (1994), gives the best results. The Battjes and Janssen model and the biphase scaling both overestimate the significant wave height. The Battjes and Janssen model and the biphase scaling perform much better in the Smith (2004) test case. The Nelson scaling, despite its limitation in bottom slope (Nelson 1994), also performs rather well. In the Hardy and Young (1996) test case the influence of the model coefficient becomes less apparent.

From the results of the Jensen (2002) and Smith (2004) test cases presented in Chapter 3 it is clear that T_p has much influence on the biphase scaling. This can be readily explained with the Ursell number and the biphase. With an increasing T_p, U_r increases quadratically. This means that the biphase progresses gradually towards $-\pi/2$. More waves will break resulting in more energy dissipation and thus a lower prediction of the significant wave heights.

Another way of presenting the results of the three models is by showing them in scatter plots that help portray the overall performance of these models. A scatter comparison of the results from the three models to the observations of the three test cases is given in Figure 4-1.

In the legend in the upper left panel of Figure 4-1 the abbreviations H&Y, MSJ and JMS stand for Hardy and Young (1996), Jensen (2002) and Smith (2004), respectively. The results from the Jensen (2002) and Smith (2004) test cases are scaled for presentation purposes. From all results a random selection was made for the

presentation in Figure 4-1. For the calculation of the error measures all results are taken into account.

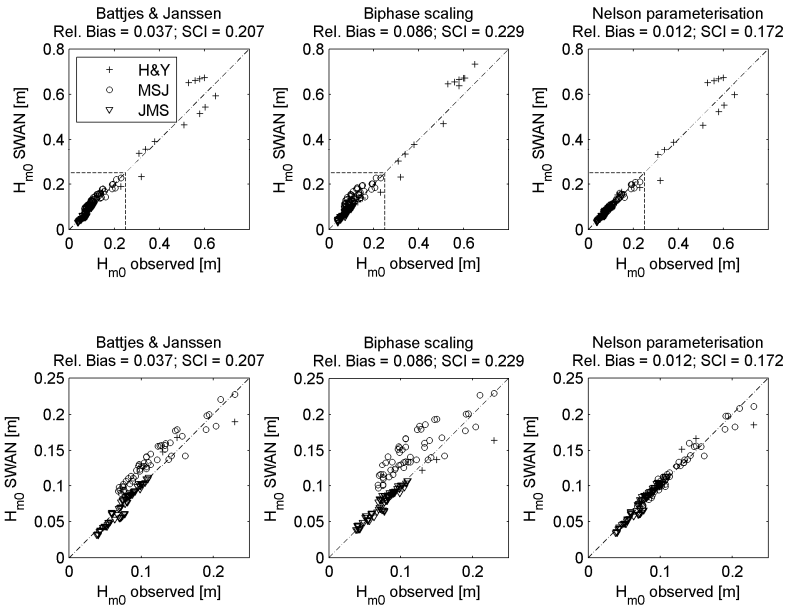

Figure 4-1: Scatter plot comparison of the results from the three models to the observations of the three test cases. Wave height data of the Jensen (2002) test case is scaled by 2 and the wave height data of the Smith (2004) test case is scaled by 4 for presentation purposes. Lower 3 panels are magnifications of the dashed rectangles drawn in the upper 3 panels.

The upper left panel shows the model results against the observations, the upper middle panel that of the biphase scaling and the upper right panel that of the Nelson scaling. The lower three panels are magnifications of the dashed rectangles in the lower left corners of the upper panels. Looking at Figure 4-1 it is clear that the Nelson scaling shows the best overall results. This becomes evident when looking at the lower panels of Figure 4-1. The statistical measures for the systematic and random error (Relative Bias and Scatter Index respectively) addressed in Section 2.5, support this conclusion. The lower the values of the relative bias and scatter index

the better the model. The lowest values are generated by the Nelson scaling.

The effect of the de-activation of the triad wave-wave interactions and bottom friction was anticipated. De-activating the triad wave-wave interactions had a much greater influence on the biphase scaling than on the Battjes and Janssen model and the Nelson scaling. The reason for this lies in the fact that the biphase scaling depends on the Ursell number. The Ursell number is the ratio of the wave steepness over the relative depth to the third power. This relative depth is described as $k_p d$, in which k_p is the peak wave number. When triad wave-wave interactions are active, energy is transferred from the spectral peak to the higher harmonics, resulting in a lowering of the spectral peak and generation of high frequency peaks. One of the high frequency peaks may become the highest peak of the spectrum which results in a different $k_p d$. When the triad wave-wave interactions are de-activated no energy transfer occurs. In SWAN the Ursell number is based on T_{m01}.
Another striking feature of the de-activation of the triad wave-wave interactions is that T_{m01} increases on the reef, whereas T_{m01} decreases when triad wave-wave interactions are active. This increase in T_{m01} results in a higher Ursell number, and with that, a biphase that is closer to $-\pi/2$. For the biphase scaling this means more energy dissipation.

5 Conclusions and recommendations

This study aimed at finding one depth-induced wave breaking model that was able to give the best overall results in terms of the significant wave height (H_{m0}) over various test cases. This was achieved by investigating three models separately on three test cases. Subsequently, a comparison of these model results was made for every separate test of the three test cases. Lastly, scatter plots were used to show the overall performance of the three models. The Nelson scaling (1994) gave the best overall results.
The value of 0.55 for the model coefficient on horizontal bottoms in the Nelson scaling is supported by the results of the Jensen (2002) test case. The description for sloping bottom profiles proves to give good results also, despite its limitation in bottom slope of 0.01 (Nelson 1987, 1994). However, there is still room for improvement on the Nelson scaling. For instance, by adding a dependency on the water depth or wind speed to the scaling.
Since only a limited number of test cases was used, it is recommended to keep testing the current Nelson scaling on more data sets to get a more general view of its performance.

The biphase scaling proposed by Van der Westhuysen (2009) did not perform as well as expected after its promising results. From this it may be concluded that the biphase as sole parameter determining the depth-induced breaking is not sufficient to describe a wide variety of bottom profiles. More testing of the biphase scaling on reef situations is recommended.

As a final remark it must be noted that the Nelson scaling indicates the model coefficient as an upper boundary for the maximum wave

height whereas the biphase scaling and the Battjes and Janssen model apply the model coefficient as a model parameter that is an average of many tests.

6 Acknowledgements

I thank Jane Mckee Smith for providing the data of the measured wave spectra at the 10 gauges for all her 31 tests. Also, I thank Thomas A. Hardy and Ian R. Young for providing the wind conditions for the four spectra presented in their publication: *Wave attenuation on an offshore coral reef* in 1996. I thank Andre van der Westhuysen for releasing his SWAN code of the biphase scaling for this study.

7 References

- Apotsos, A., B. Raubenheimer, S. Elgar, and R.T. Guza, 2008, Testing and calibrating parametric wave transformation models on natural beaches, *Coastal Eng.,* 55, 224 – 235.
- Battjes, J.A., and J.P.F.M. Janssen, 1978, Energy loss and set-up due to breaking of random waves, *Proc. 16th Int. Conf. on Coastal Engineering. ASCE, New York,* pp. 570 – 587.
- Battjes, J.A., and M.J.F. Stive, 1985, Calibration and verification of a dissipation model for random breaking waves, *J. Geophys. Res.*, 90, C5, 9159 – 9167.
- Booij, N., R.C. Ris, and L.H. Holthuijsen, 1999, A third-generation wave model for coastal regions, Part I, Model description and validation, *J. Geophys. Res.,* 104, C4, 7649 – 7666.
- Bouws, E., H. Günther, W. Rosenthal and C.L. Vincent, 1985, Similarity of the wind wave spectrum in finite depth water. 1. Spectral form, *J. Geophys. Res.,* 90, C1, 975 - 986
- Eldeberky, Y., 1996, Nonlinear transformation of wave spectra in the nearshore zone, Ph.D. thesis, published as *Communications on Hydraulic and Geotechnical Engineering,* Delft University of Technology, Faculty of Civil Engineering, Report No. 96 - 4, 203 pp.
- Hardy T.A., and I.R. Young, 1996, Wave attenuation on an offshore coral reef, *J. Geophys. Res.*, 101, C6, 14311 – 14326.
- Holthuijsen, L.H., 2007, *Waves in oceanic and coastal waters.* 1st edition: Cambridge university press, pp. 387.

- Holthuijsen, L.H., and N. Booij, 2006, Experimental wave breaking in SWAN, *Proc. 30th Int. Conf. on Coastal Engineering*, 392 – 402.
- Jensen, M.S., 2002, Breaking of waves over a steep bottom slope, Ph.D. thesis, Published by Hydraulic & Coastal Engineering Laboratory, Aalborg University, Series paper No. 22.
- Nairn, R.B., 1990, Prediction of cross-shore sediment transport and beach profile evolution, Ph.D thesis, Imperial College, London, 391 pp.
- Nelson, R.C., 1987, Design wave heights on very mild slopes, *Civil Eng. Trans., Inst. Eng. Aust.* 29, 157 – 161.
- Nelson, R.C., 1994, Depth limited design wave height in very flat regions, *Coastal Eng.,* 23, 43 – 59.
- Nelson, R.C., 1997, Height limits in top down and bottom up wave environments, *Coastal Eng.,* 32, 247 – 254.
- Ris, R.C., 1997, Communications on Hydraulic and Geotechnical Engineering: Spectral modeling of wind waves in coastal areas, Ph.D.-dissertation, Delft University of Technology, Department of Civil Engineering, The Netherlands, Report No. 97 – 4.
- Ruessink B.G., D.J.R. Walstra, and H.N. Southgate, (2003), Calibration and verification of a parametric wave model on barred beaches. *Coastal Eng.*, 48, 139-149.
- Smith, J.M., 2004, Shallow-water spectral shapes, *Proc. 29th Int. Conf. on Coastal Engineering* (Lisbon), Singapore, World Scientific, pp. 206 – 217.
- Van der Westhuysen, A.J., M. Zijlema, and J.A. Battjes, 2007, Nonlinear saturation-based whitecapping dissipation in SWAN for deep and shallow water, *Coastal Eng.,* 54, 151 – 170.

- Van der Westhuysen, A.J., 2009, Spectral modelling of depth-induced wave breaking under finite depth wave growth conditions, *J. Geophys. Res. Under Review*
- Young, I.R., and L.A. Verhagen, 1996a, The growth of fetch limited waves in water of finite depth. Part 1. Total energy and peak frequency, *Coastal Eng.*, 29, 47 – 78.
- Zijlema, M., and A.J. van der Westhuysen, 2005, On convergence behaviour and numerical accuracy in stationary SWAN simulations of nearshore wind wave spectra, *Coastal Eng.* 52, 237 – 256.

Appendices

Part I:
On the time scales of wave processes

&

Part II:
Depth-induced breaking:
A comparison on the performance of three models

Contents Appendices

1 Appendix A – ICCE 2008 publication

Here the publication of the ICCE 2008 is presented.

Wave physics in a tidal inlet

Leo H. Holthuijsen[1], Marcel Zijlema[1] and Paul J. van der Ham[1]

Time scales of all processes, except diffraction, that affect waves penetrating a tidal inlet under flood conditions and propagating over the tidal flats have been computed with the third-generation spectral wave model SWAN. The processes are those of propagation (shoaling, bunching, refraction and frequency-shifting), generation (wind), dissipation (whitecapping, depth-induced breaking and bottom friction), wave-wave interactions (quadruplet and triad interactions) and work done by the radiation stresses against the currents. These time scales are of the order 100 s – 1000 s, except the time scale of the work done by the radiation stresses, which is of the order of 10,000 s and except in deeper water where the time scales are much longer (channels and the open sea side of the islands).

Introduction

Waves entering a tidal inlet and subsequently propagating over tidal flats, will shoal, refract and eventually break on a beach. In addition, they may receive some energy from the wind and from wave-current interactions (through work done by the radiation stresses) and they will also loose energy due to white-capping and bottom friction. These processes may be affected by tidal currents, which will also induce frequency shifting of the waves. All these processes can be represented as terms in the spectral energy (or action) balance equation of the waves. In a generic sense these terms are fairly well understood. However, their relative importance in a real situation is not well known, e.g. the time scales of the various processes have not been computed earlier. We compute these time scales, including those of propagation in geographic space (shoaling) and spectral space (bottom- and current-induced refraction and frequency-shifting), and the work done by radiation stresses against the current for a tidal inlet in the Netherlands in a flood case.

The wave model

The wave model that we use for the computations is the SWAN model (Booij et al., 1999). This model is formulated in terms of the action balance:

$$\frac{\partial N(\sigma,\theta;x,y,t)}{\partial t}+\frac{\partial c_{g,x}N(\sigma,\theta;x,y,t)}{\partial x}+\frac{\partial c_{g,y}N(\sigma,\theta;x,y,t)}{\partial y}+$$

$$+\frac{\partial c_{\theta}N(\sigma,\theta;x,y,t)}{\partial \theta}+\frac{\partial c_{\sigma}N(\sigma,\theta;x,y,t)}{\partial \sigma}=\frac{S(\sigma,\theta;x,y,t)}{\sigma}$$

where $N(\sigma,\theta)$ is the action density spectrum defined as $E(\sigma,\theta)/\sigma$ where $E(\sigma,\theta)$ is the energy density and σ is the relative frequency. The first term in the left-hand side of this equation represents the local rate of change of action density in time, the second and third terms represent propagation of action in geographical space (with propagation velocities

[1] Faculty of Civil Engineering and Geosciences, Delft University of Technology, Stevinweg 1, 2628CN, Delft, the Netherlands

$c_{g,x}$ and $c_{g,y}$ in *x*- and *y*-space, respectively, thus accounting for shoaling and energy bunching in the presence of currents). The fourth term represents depth-induced and current-induced refraction (with propagation velocity c_θ in θ-space). The fifth term represents shifting of the relative frequency due to variations in depth and currents (with propagation velocity c_σ in σ-space). The term $S(\sigma,\theta)$ is the source term in terms of energy density (the division by σ makes $S(\sigma,\theta)/\sigma$ the source term for action density). It represents the effects of generation, nonlinear wave-wave interactions and dissipation. In this study we will use the formulations as given by Booij et al. (1999) as upgraded by v.d. Westhuysen et al (2007). The propagation is computed with the linear wave theory (excluding diffraction).

The formulation in terms of action density instead of energy density has been chosen to avoid an explicit representation of the work done by wave radiation stresses against ambient currents. To inspect the role of this work, the action balance equation should be re-written in terms of the energy balance. This equation is identical to the above equation with $N(\sigma,\theta)$ replaced by $E(\sigma,\theta)$, $S(\sigma,\theta)/\sigma$ replaced by $S(\sigma,\theta)$ and one term added to the left-hand side: $+\Phi_{\alpha\beta}\,\partial U_\beta/\partial x_\alpha$ (using the summation convention) representing the work done by the radiation stresses with $\Phi_{\alpha\beta}$ as the radiation stress tensor and U_β as the current velocity (Phillips, 1977, p. 66).

To interpret the various processes, we will consider the spatial variation of the intensity of each term of the energy balance. We define this intensity as the integral over the spectral domain of the absolute value of the term under consideration. The basic reason to take the absolute value here is to include the wave-wave interactions. These are in principle conservative and the integral of the term itself over the spectral domain ($\sigma \geq 0, 0 \leq \theta \leq 2\pi$) would be zero. In addition we will normalise these integrated terms to arrive at the time scales of the processes. A common definition of time scale τ for the total wave energy $m_0 = \iint E(\sigma,\theta)\,d\theta d\sigma$ is based on the absolute rate of change: $\left|\frac{\partial m_0}{\partial t}\right| = \frac{1}{\tau} m_0$, so that the time scale $\tau = \left[\frac{1}{m_0}\left|\frac{\partial m_0}{\partial t}\right|\right]^{-1}$. The time scales of the other terms (processes) can be defined similarly as follows. The energy balance for one process (ignoring all others), for instance refraction, would be $\frac{\partial E(\sigma,\theta)}{\partial t} = -\frac{\partial c_\theta E(\sigma,\theta)}{\partial \theta}$. Integrating the absolute value of this equation over the spectral domain and normalising as above gives $\frac{1}{m_0}\left|\frac{\partial m_0}{\partial t}\right| = \frac{1}{m_0}\iint\left|\frac{\partial c_\theta E(\sigma,\theta)}{\partial \theta}\right| d\theta d\sigma$. In other words, the time scale of refraction τ_θ is equal to $\tau_\theta = \frac{1}{m_0}\iint\left|\frac{\partial c_\theta E(\sigma,\theta)}{\partial \theta}\right| d\theta d\sigma$. Since the smallest time scale indicates the highest intensity, we show the inverse of the time scale in the illustrations of our results below.

The work done by the radiation stresses can be computed explicitly based on the full expression, which contains four terms ($\alpha, \beta \in \{x, y\}$):

$$\Phi_{\alpha\beta}\frac{\partial U_\beta}{\partial x_\alpha} = \Phi_{xx}\frac{\partial U_x}{\partial x} + \Phi_{xy}\frac{\partial U_y}{\partial x} + \Phi_{yy}\frac{\partial U_y}{\partial y} + \Phi_{yx}\frac{\partial U_x}{\partial y}$$

which involves computing all radiation stress terms. The alternative, which avoids this, is to consider this term as the rest term of the energy balance when all other terms have been computed:

$$\Phi_{\alpha\beta}\frac{\partial U_\beta}{\partial x_\alpha} = S(\sigma,\theta;x,y,t) - \frac{\partial E(\sigma,\theta;x,y,t)}{\partial t} - \frac{\partial c_{g,x}E(\sigma,\theta;x,y,t)}{\partial x} - \frac{\partial c_{g,y}E(\sigma,\theta;x,y,t)}{\partial y} - \frac{\partial c_\theta E(\sigma,\theta;x,y,t)}{\partial \theta} - \frac{\partial c_\sigma E(\sigma,\theta;x,y,t)}{\partial \sigma}$$

The wave model provides us with all these terms so that we use this alternative. We normalise this estimate of the work done by the radiation stresses like all the other terms.

Conditions

We consider the tidal inlet between the islands of Terschelling and Ameland in the north of the Netherlands (Fig. 1) during flood conditions, under wave conditions with a significant wave height of 6 m and a peak period of 12 s from northerly directions (JONSWAP spectrum with $\cos^2\theta$ directional distribution). The wind speed is 15 m/s from the same direction. The bathymetry and the curvilinear computational grid are shown in Fig. 2. The computations are carried out for a stationary condition.

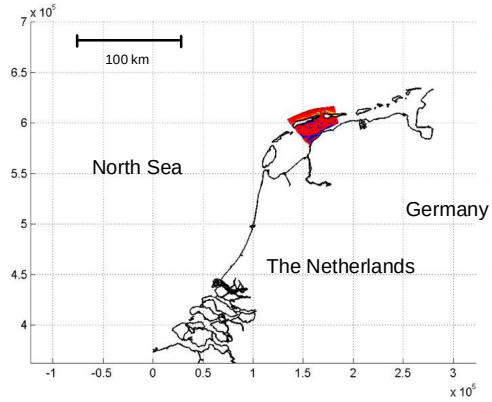

Fig. 1 The area of computation in the north of The Netherlands.

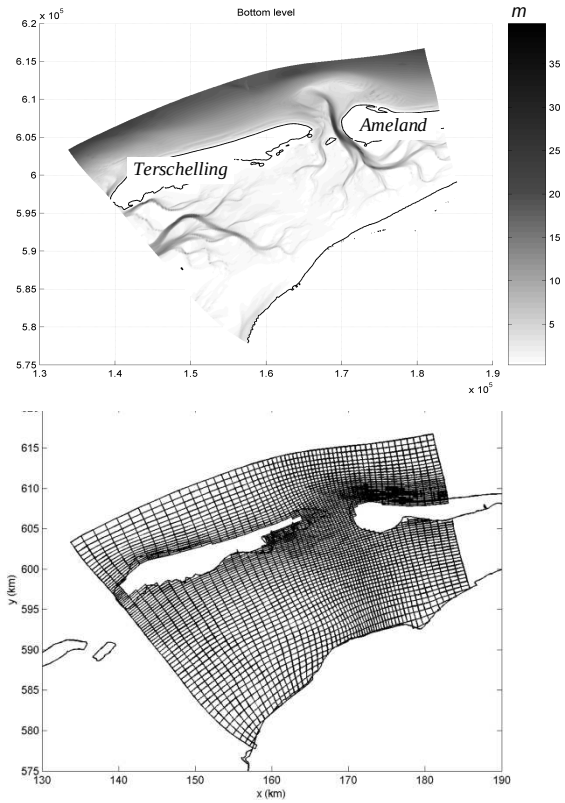

Fig. 2 The bathymetry of the study area (top panel) and the computational curvi-linear grid (bottom panel; every 5th grid line shown).

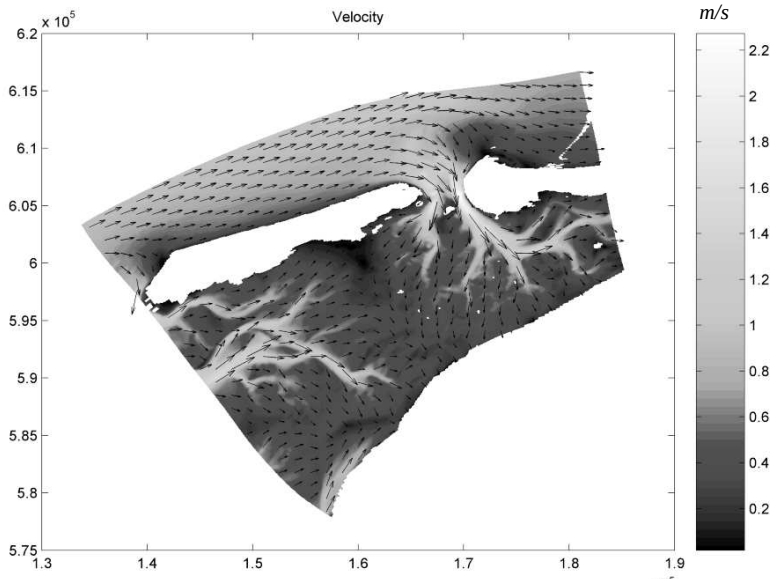

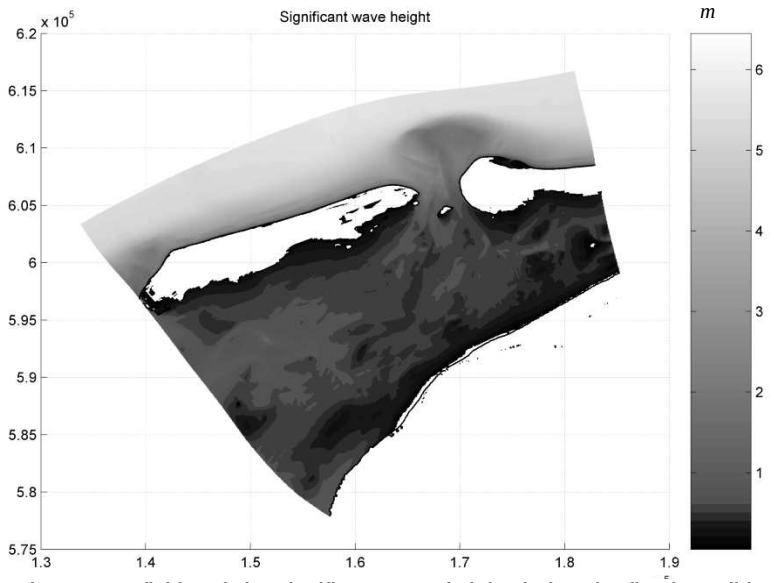

Fig. 3 The current field and the significant wave height during the flood conditions of the computations.

Results

Qualitatively the results for the source terms are essentially as expected. They are given in Figs. 4-6 for the generation and dissipation processes that dominate in deep water (wind input, quadruplet wave-wave interactions and white-capping). It is obvious from these results that these processes are relatively more active in the shallow region behind the islands than in the deeper water in front of the islands. That is not so much because the processes are most intense in the shallow region – but rather that they are relatively most active there, i.e., relative to the local conditions. For instance, the wind is most effective at the lee side of the islands because the waves are small there and grow relatively fast. Remarkably, the wind input is also very active in the shallowest parts near the main land (possibly because the ratio of wind speed over phase speed increases there). The quadruplet wave-wave interactions follow this pattern closely but with a somewhat longer time scale. Apparently these interactions are modifying the waves not only in response to the wind but also in response to (all) other processes. The white-capping follows the wind input closely with practically the same time scale as the wind input.

The time scales of the generation and dissipation processes that are typical for shallow water are given in Figs. 7-9. The depth-induced breaking and the triad wave-wave interactions have an almost on-off character: they are active in the surf zone, which extends across the tidal delta) and practically inactive outside the surf zone although the triad wave-wave interactions are active in a narrower zone (closer to shore) than depth-induced breaking. The coast-parallel

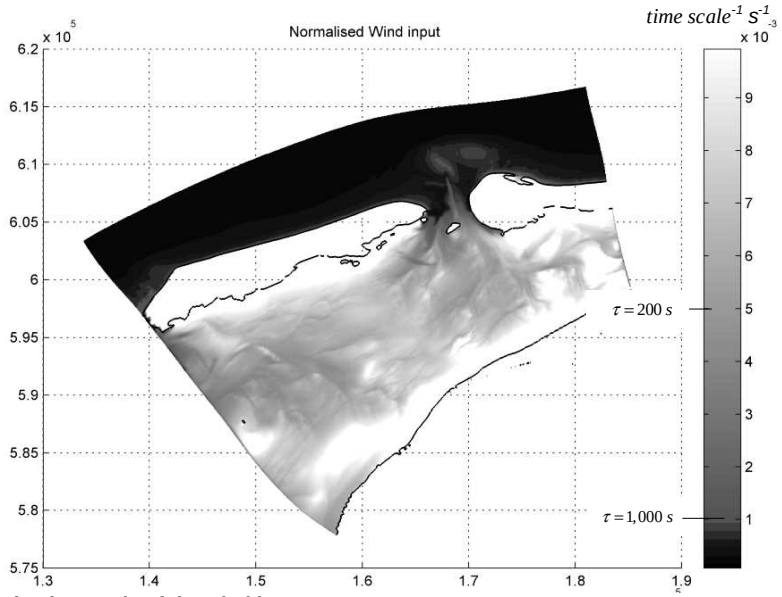

Fig. 4 The time scale of the wind input.

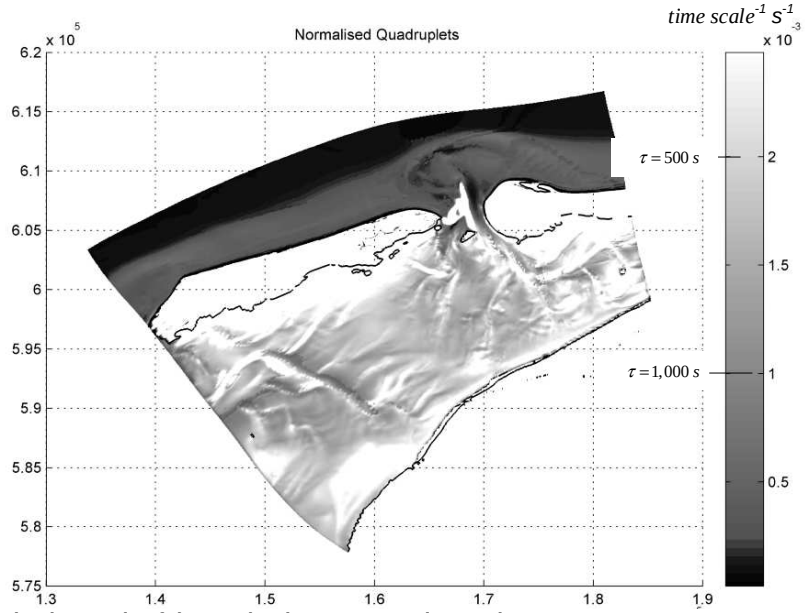

Fig. 5 The time scale of the quadruplet wave-wave interactions.

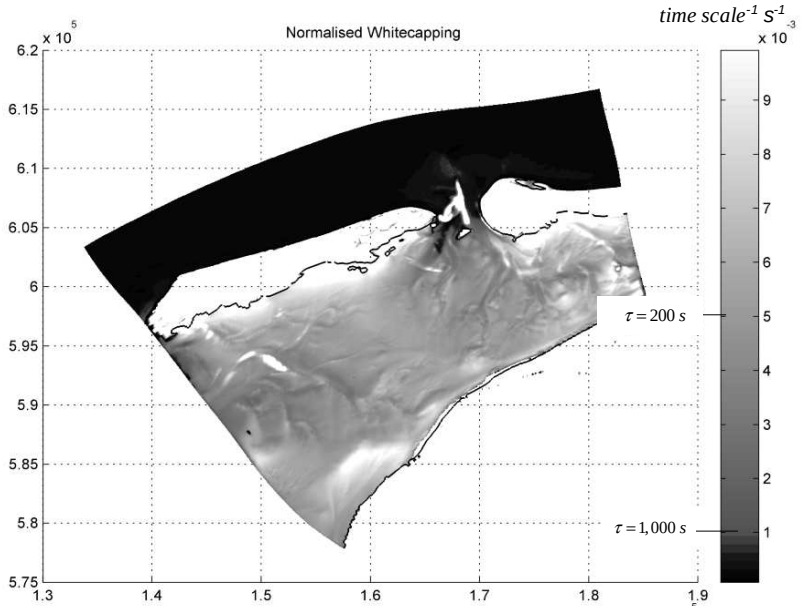

Fig. 6 The time scale of the white-capping.

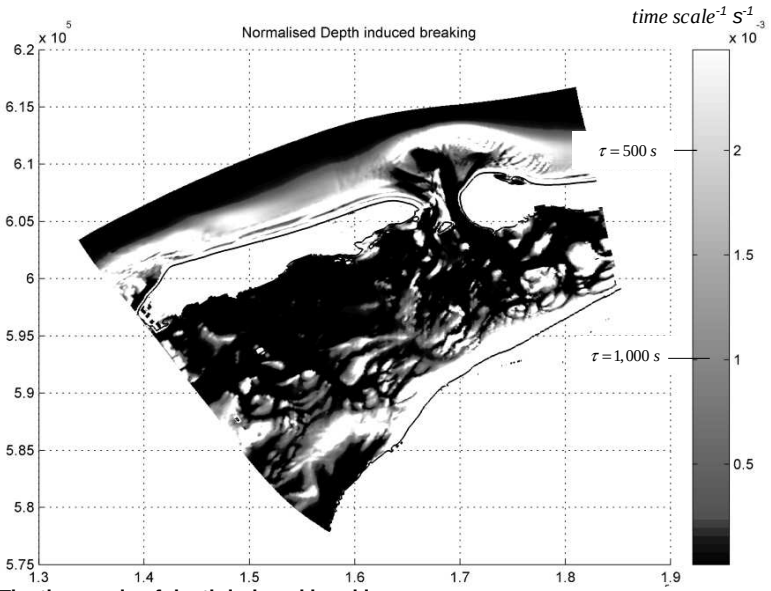

Fig. 7 The time scale of depth-induced breaking.

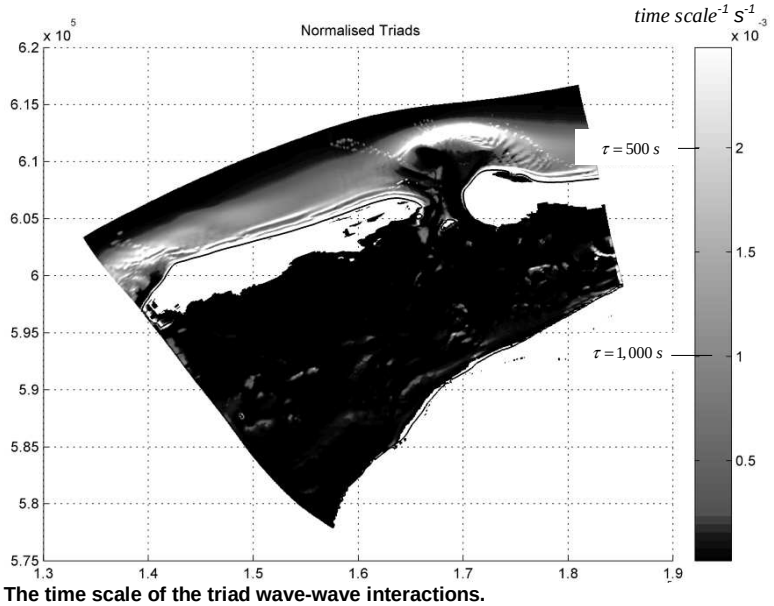

Fig. 8 The time scale of the triad wave-wave interactions.

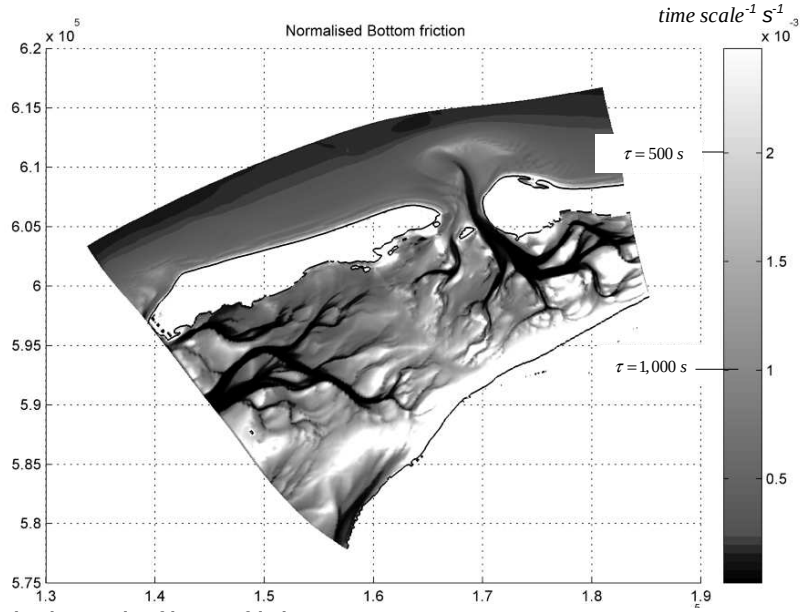

Fig. 9 The time scale of bottom friction.

streaks just north of Terschelling (the western island) and the feathery pattern just north-east of the tidal delta (in the north-east corner) is a direct imprint of the local bathymetry. The pattern of bottom friction closely follows the bathymetry (Fig. 9) with fairly intense effects in the shallowest regions (the tidal flats) and an obvious absence in the channels.

The intensity of the propagation processes in geographic space (shoaling and current-induced bunching) and in spectral space (refraction and frequency-shifting) are given in Figs. 10-12. The two terms for the propagation in geographic space have been combined to present not the two transport components separately but rather, the magnitude of the transport:

$$\left\{\left[\frac{\partial c_{g,x} N(\sigma,\theta;x,y,t)}{\partial x}\right]^2+\left[\frac{\partial c_{g,y} N(\sigma,\theta;x,y,t)}{\partial y}\right]^2\right\}^{1/2}$$

(integrated and normalized as all the other terms). The pattern of the time scale of this process closely follows the pattern of the bathymetry, with some emphasis on the shoulders of the channels (see Fig. 10).

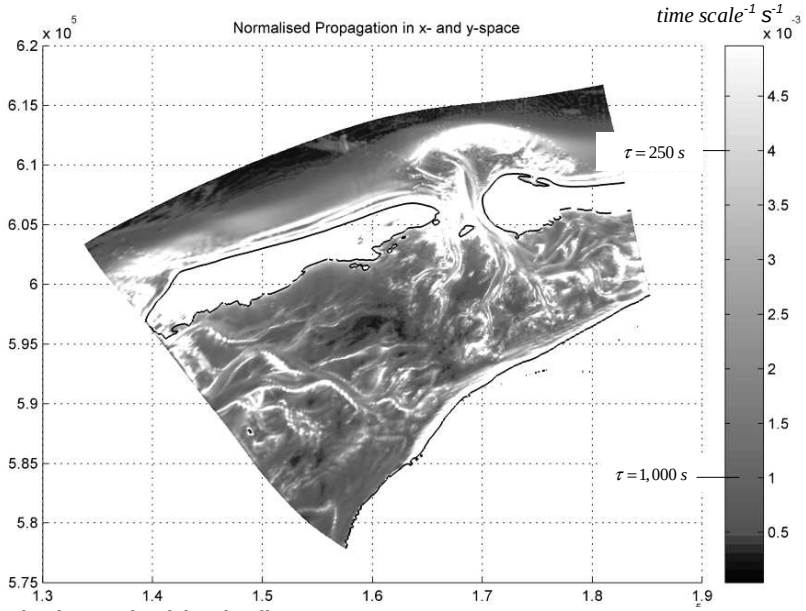

Fig. 10 The time scale of the shoaling process.

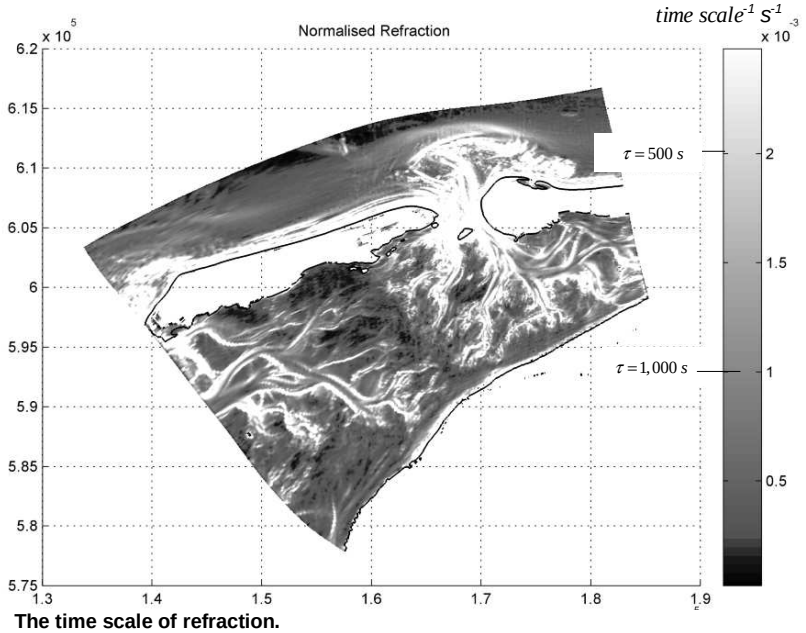

Fig. 11 The time scale of refraction.

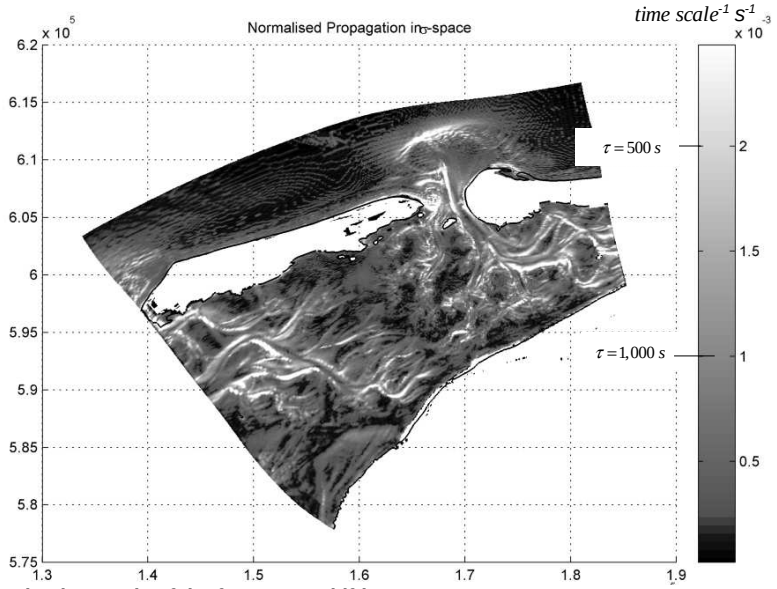

Fig. 12 The time scale of the frequency-shifting.

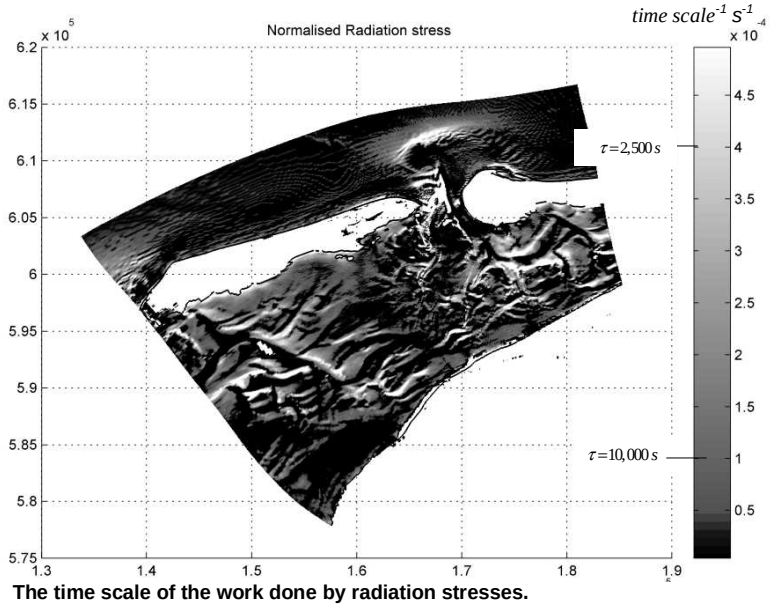

Fig. 13 The time scale of the work done by radiation stresses.

The pattern of the time scale of refraction is very similar to that of shoaling, with the same concentration on the shoulders of the channels but with slightly longer time scales. This concentration of shoaling and refraction on the shoulders of the channels may not only be due to steep bottom gradients there but also due to large gradients in the currents. This is confirmed by the similar pattern of frequency-shifting (Fig. 12) which also tends to concentrate on the shoulders of the channels.

The pattern of the time scale of the work done by radiation stress is given in Fig. 13. Obviously, the magnitude of this time scale is one order longer than the time scales of all the other processes.

Conclusions

Under the conditions shown here, of storm waves penetrating a tidal inlet from a shelf sea during a flood tide, and propagating over a tidal flat to the main land, the time scales of all processes of propagation, generation and dissipation are typically of the order of 100 s – 1000 s, except for the time scale of the work done by radiation stresses against the currents, which is of the order of 10,000 s. The "deep water" processes of wind generation, white-capping and quadruplet wave-wave interactions are significantly more active (relative to the local situation) over the tidal flats than in deeper water (the channels and the open sea side of the islands). The "shallow water" processes of triad wave-wave interactions and depth-induced breaking tend to concentrate in the surf zones (the triad interactions even more than the breaking). Bottom friction is more diffusely distributed with a total absence in the channels. The propagation processes (shoaling, bunching, refraction and frequency-shifting) tend to concentrate on the shoulders of the channels where the steepest gradients in depth and currents occur. This is also the case for the work done by the radiation stresses.

Acknowledgements

We wish to thank Deltares/Delft Hydraulics, in particular André van der Westhuysen, for providing us with the basic data for our computations (bathymetry and current fields).

References

- Booij, N., R.C. Ris and L.H. Holthuijsen, 1999, A third-generation wave model for coastal regions, Part I, Model description and validation, J.Geoph.Research, 104, C4, 7649-7666
- Phillips, O.M., 1977, 2nd edition, The dynamics of the upper ocean, Cambridge University Press, 336 p.
- Westhuysen, A. van der, M. Zijlema and J.A. Battjes, 2007, Nonlinear saturation-based whitecapping dissipation in SWAN for deep and shallow water, Coastal Engineering, 54, 2, 151 – 170

2 Appendix B – Convergence behaviour

Three subplots representing the convergence behaviour of H_{m0} and T_{m01} are given in this appendix. First the Smith (2004) test case is given, followed by the Jensen (2002) test case and lastly, the Hardy and Young (1996) test case.

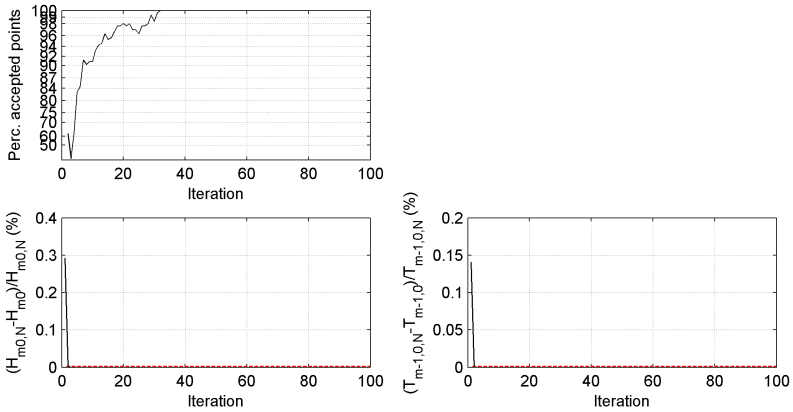

Figure 1: Convergence behaviour of the significant wave height and the peak period for the Smith (2004) test case.

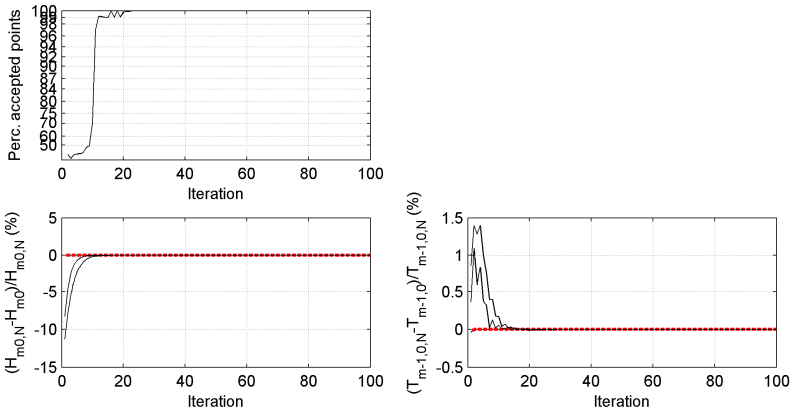

Figure 2: Convergence behaviour of the significant wave height and peak period for the Jensen (2002) test case.

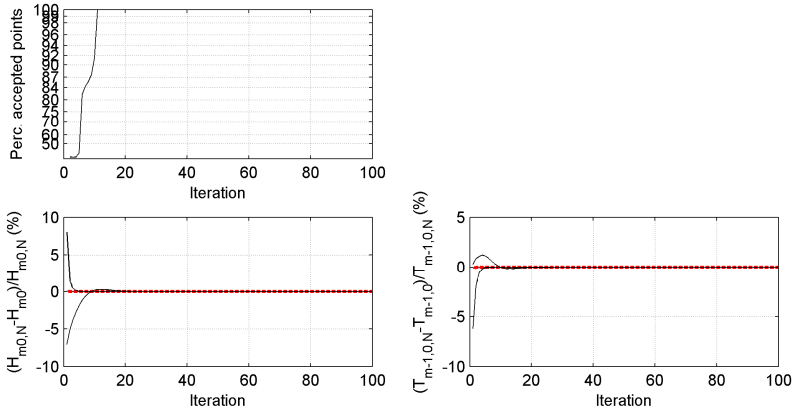

Figure 3: Convergence behaviour of the significant wave height and peak period for the Hardy and Young (1996) test case.

3 Appendix C – Results Smith

Here all results from the Smith (2004) test case are presented. The results are presented in numerical order.

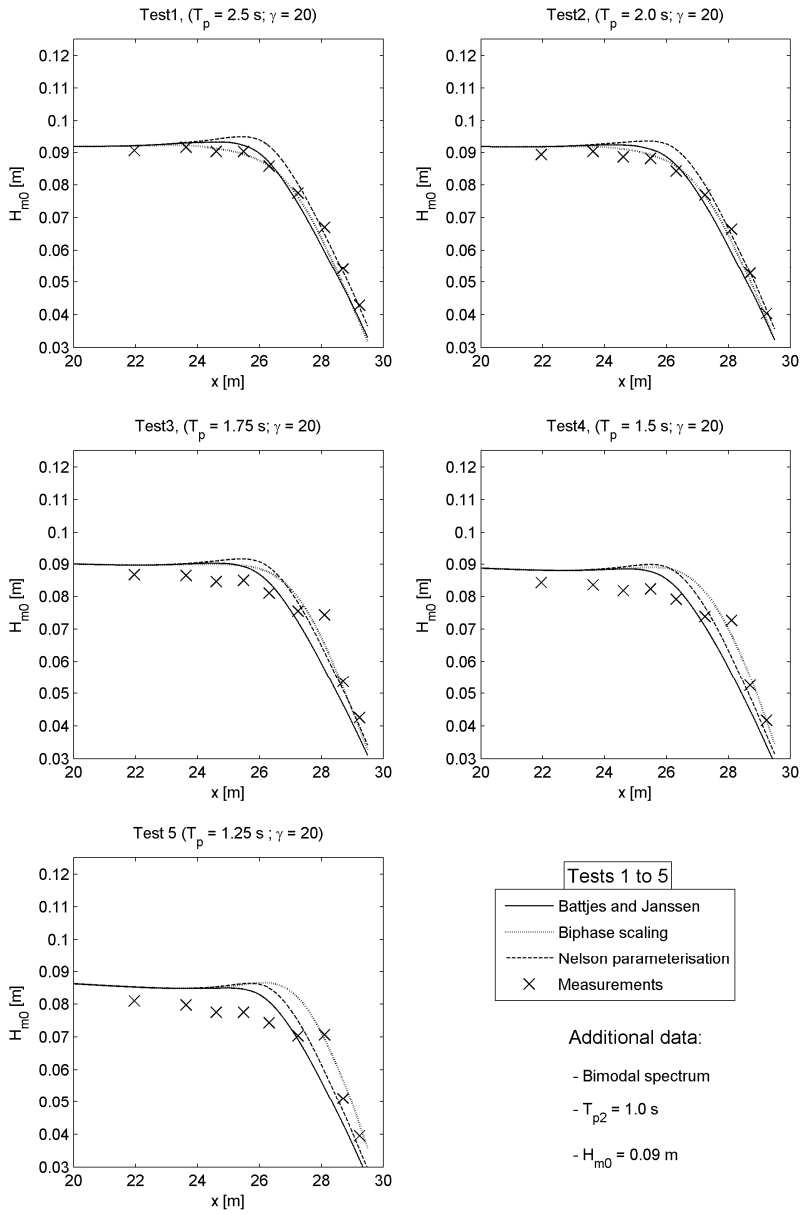

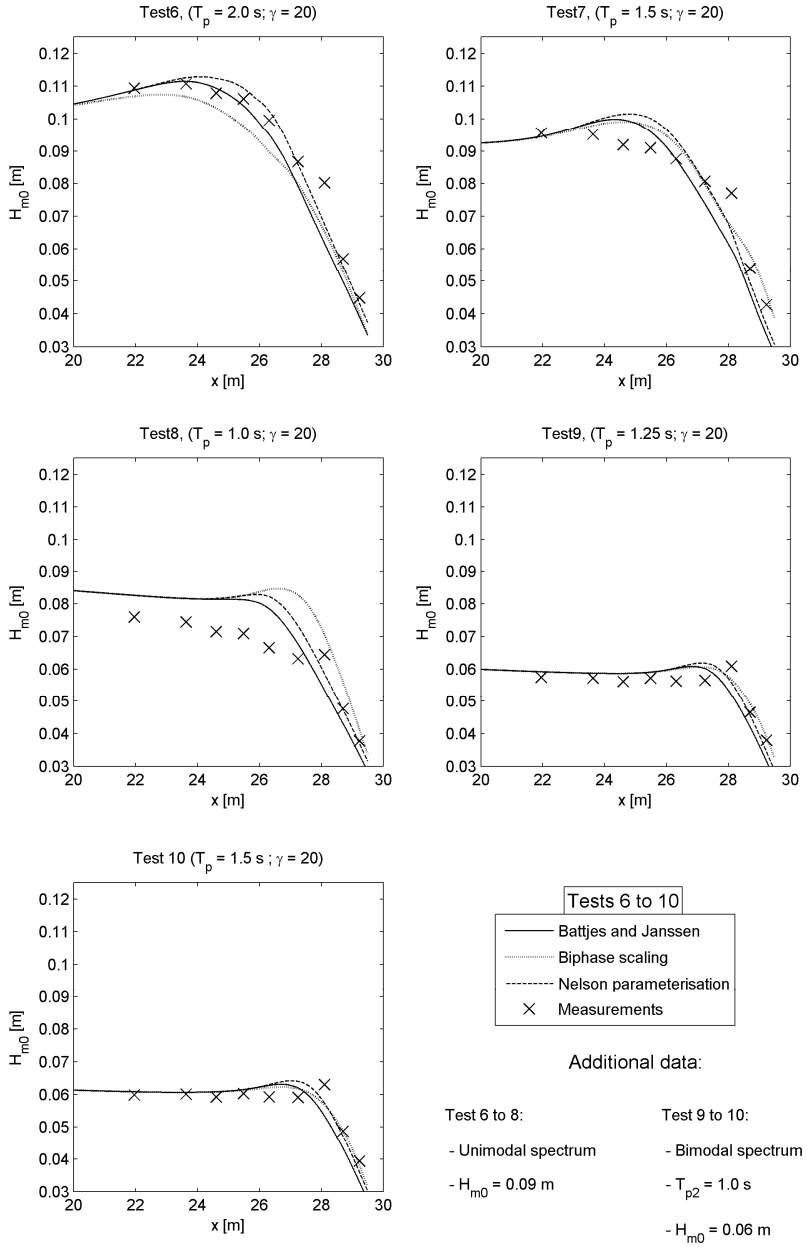
Test6, (T_p = 2.0 s; γ = 20)
Test7, (T_p = 1.5 s; γ = 20)
Test8, (T_p = 1.0 s; γ = 20)
Test9, (T_p = 1.25 s; γ = 20)
Test 10 (T_p = 1.5 s ; γ = 20)
H_{m0} [m]
x [m]
Tests 6 to 10
Battjes and Janssen
Biphase scaling
Nelson parameterisation
Measurements
Additional data:
Test 6 to 8:
- Unimodal spectrum
- H_{m0} = 0.09 m
Test 9 to 10:
- Bimodal spectrum
- T_{p2} = 1.0 s
- H_{m0} = 0.06 m

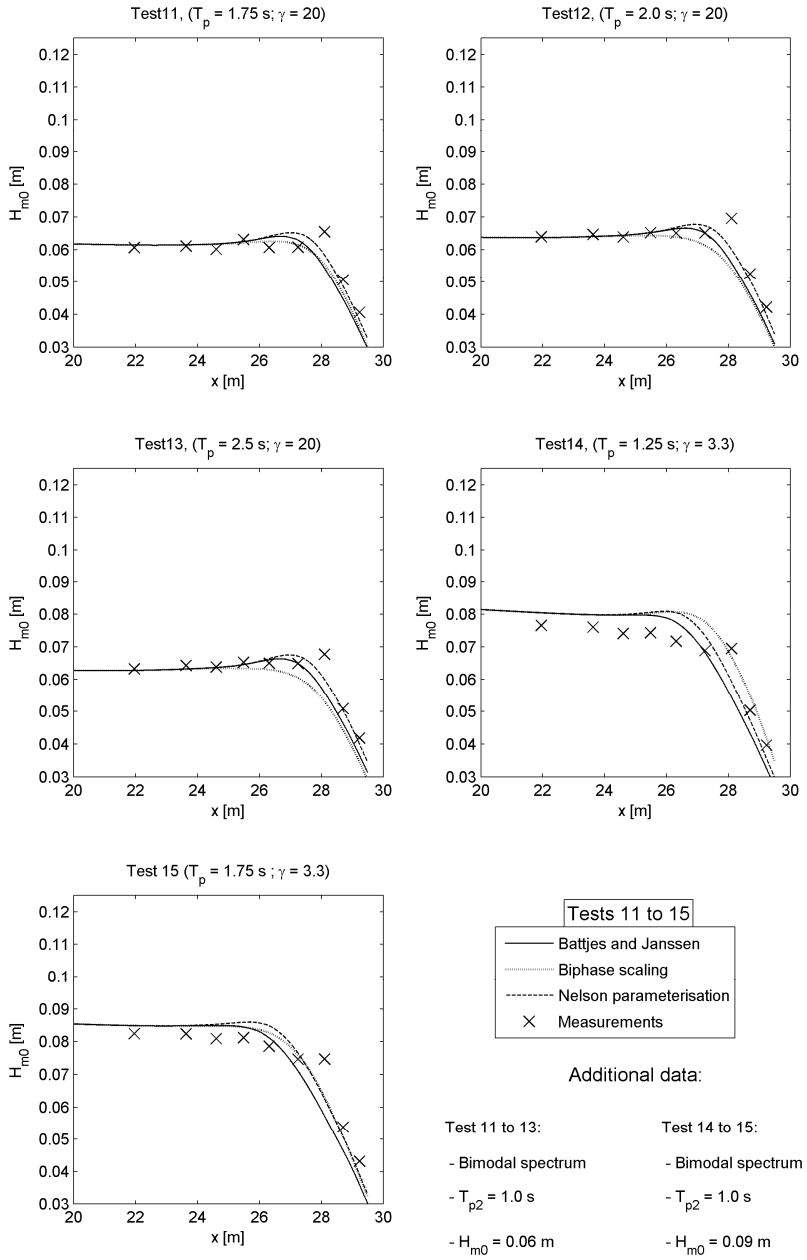
Test11, (T_p = 1.75 s; γ = 20)
Test12, (T_p = 2.0 s; γ = 20)
Test13, (T_p = 2.5 s; γ = 20)
Test14, (T_p = 1.25 s; γ = 3.3)
Test 15 (T_p = 1.75 s ; γ = 3.3)
H_m0 [m]
x [m]
Tests 11 to 15
Battjes and Janssen
Biphase scaling
Nelson parameterisation
Measurements
Additional data:
Test 11 to 13:
- Bimodal spectrum
- T_p2 = 1.0 s
- H_m0 = 0.06 m
Test 14 to 15:
- Bimodal spectrum
- T_p2 = 1.0 s
- H_m0 = 0.09 m

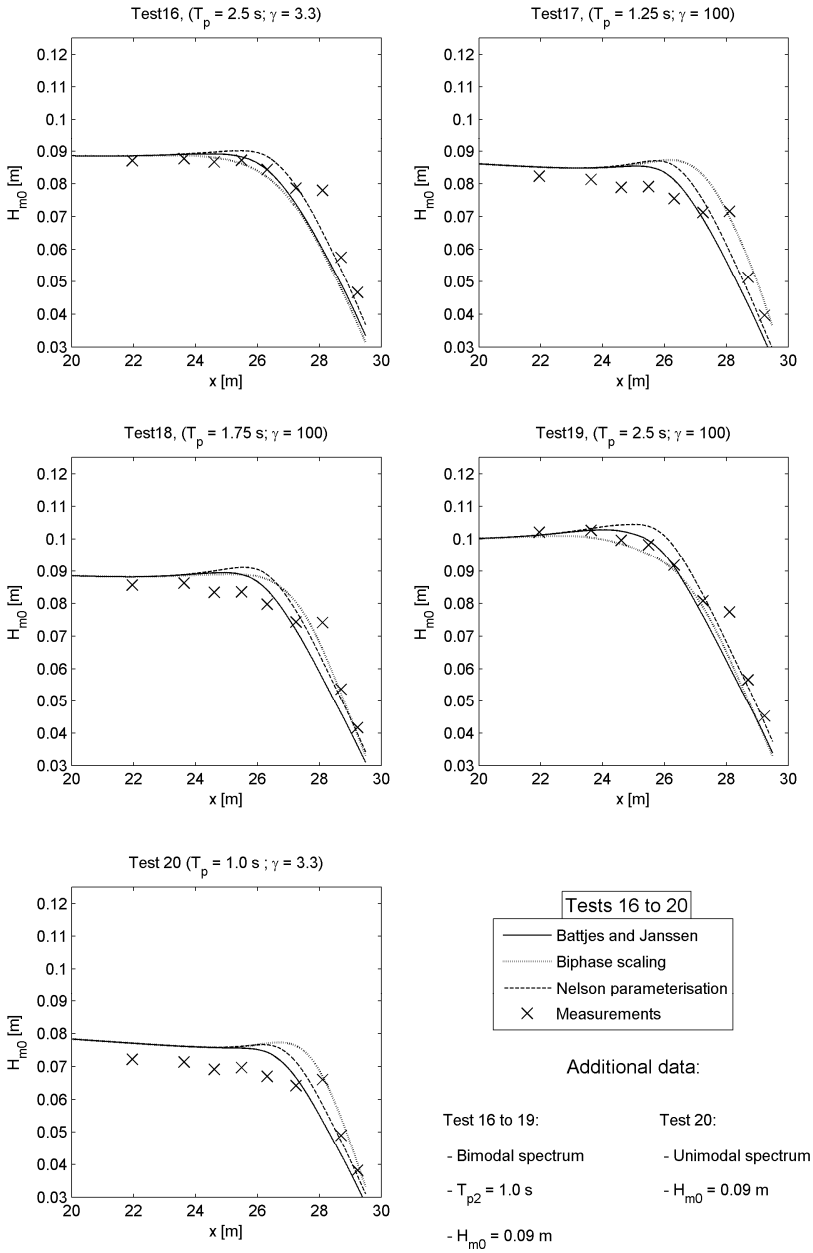
Test16, (T_p = 2.5 s; γ = 3.3)
Test17, (T_p = 1.25 s; γ = 100)
Test18, (T_p = 1.75 s; γ = 100)
Test19, (T_p = 2.5 s; γ = 100)
Test 20 (T_p = 1.0 s ; γ = 3.3)
H_m0 [m]
x [m]
Tests 16 to 20
Battjes and Janssen
Biphase scaling
Nelson parameterisation
Measurements
Additional data:
Test 16 to 19:
- Bimodal spectrum
- T_p2 = 1.0 s
- H_m0 = 0.09 m
Test 20:
- Unimodal spectrum
- H_m0 = 0.09 m

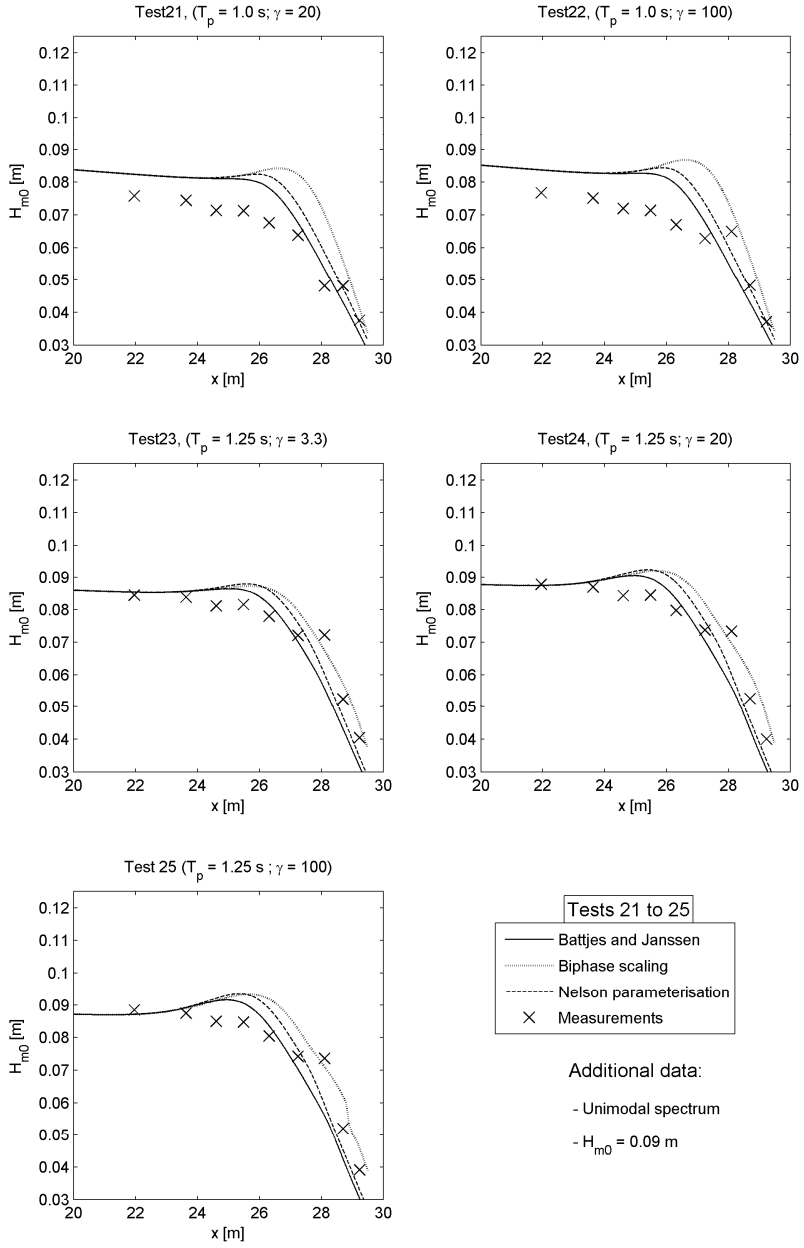
Test21, (T_p = 1.0 s; γ = 20)
Test22, (T_p = 1.0 s; γ = 100)
Test23, (T_p = 1.25 s; γ = 3.3)
Test24, (T_p = 1.25 s; γ = 20)
Test 25 (T_p = 1.25 s ; γ = 100)
H_m0 [m]
x [m]
Tests 21 to 25
Battjes and Janssen
Biphase scaling
Nelson parameterisation
Measurements
Additional data:
- Unimodal spectrum
- H_m0 = 0.09 m

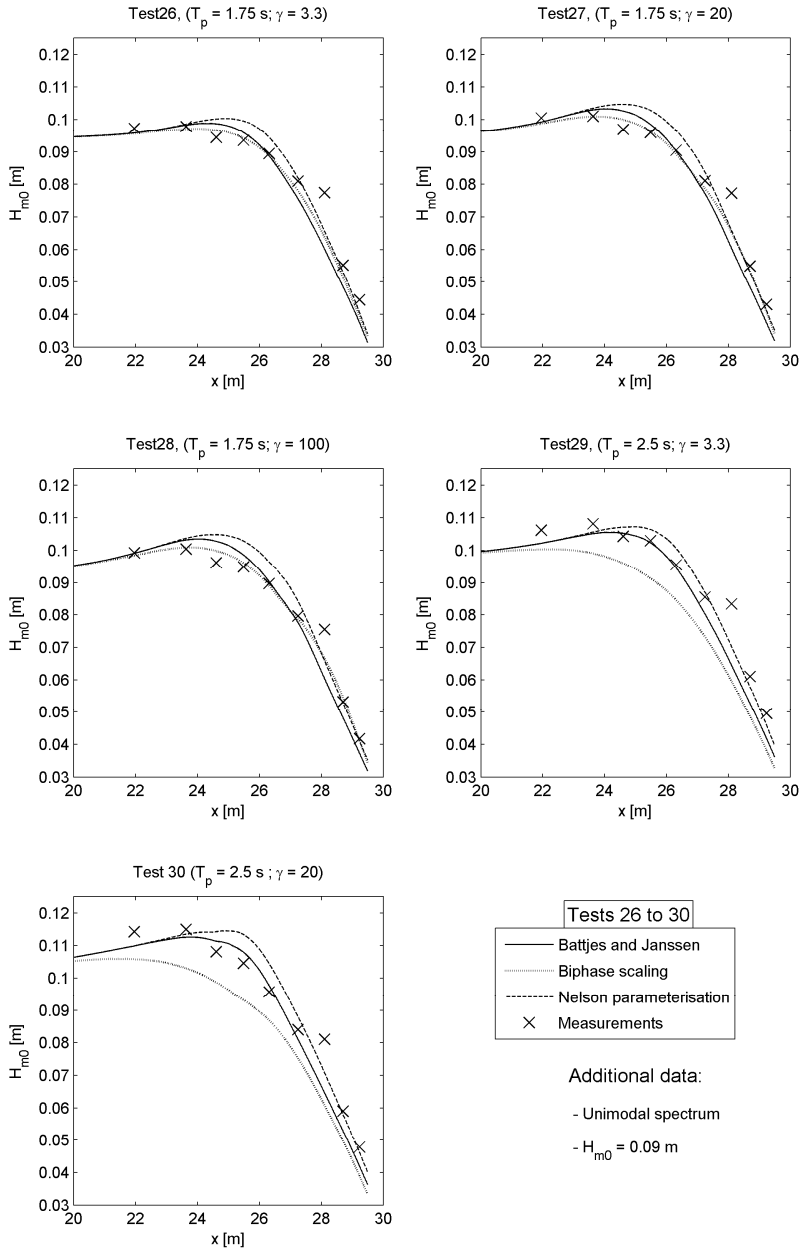
Test26, (T_p = 1.75 s; γ = 3.3)
Test27, (T_p = 1.75 s; γ = 20)
Test28, (T_p = 1.75 s; γ = 100)
Test29, (T_p = 2.5 s; γ = 3.3)
Test 30 (T_p = 2.5 s ; γ = 20)
H_{m0} [m]
x [m]
Tests 26 to 30
Battjes and Janssen
Biphase scaling
Nelson parameterisation
Measurements
Additional data:
- Unimodal spectrum
- H_{m0} = 0.09 m

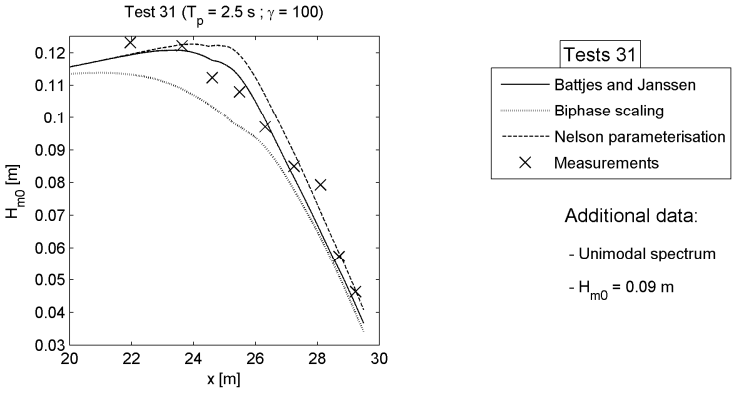
Test 31 (T_p = 2.5 s ; γ = 100)
H_{m0} [m]
x [m]
0.12
0.11
0.1
0.09
0.08
0.07
0.06
0.05
0.04
0.03
20
22
24
26
28
30
Tests 31
Battjes and Janssen
Biphase scaling
Nelson parameterisation
Measurements
Additional data:
- Unimodal spectrum
- H_{m0} = 0.09 m

4 Appendix D – Results Jensen

Here all results from the Jensen (2002) test case are presented.

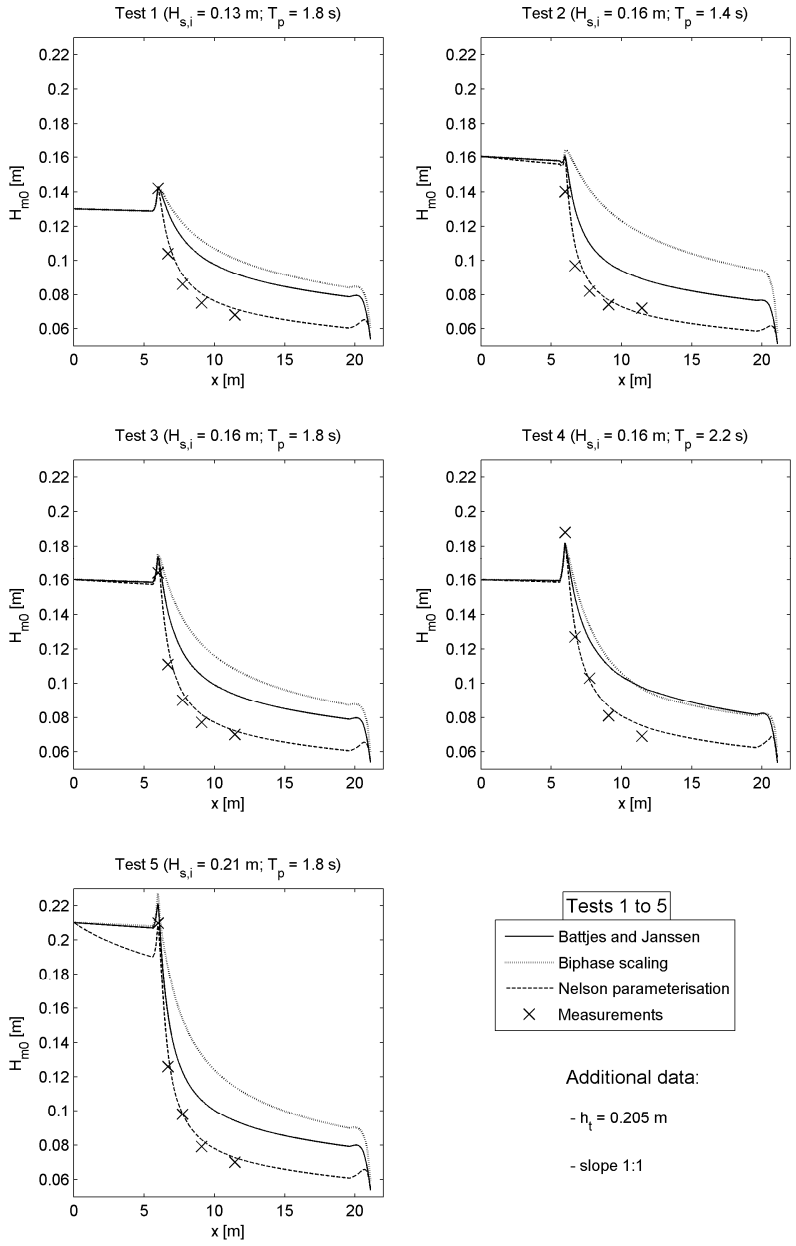

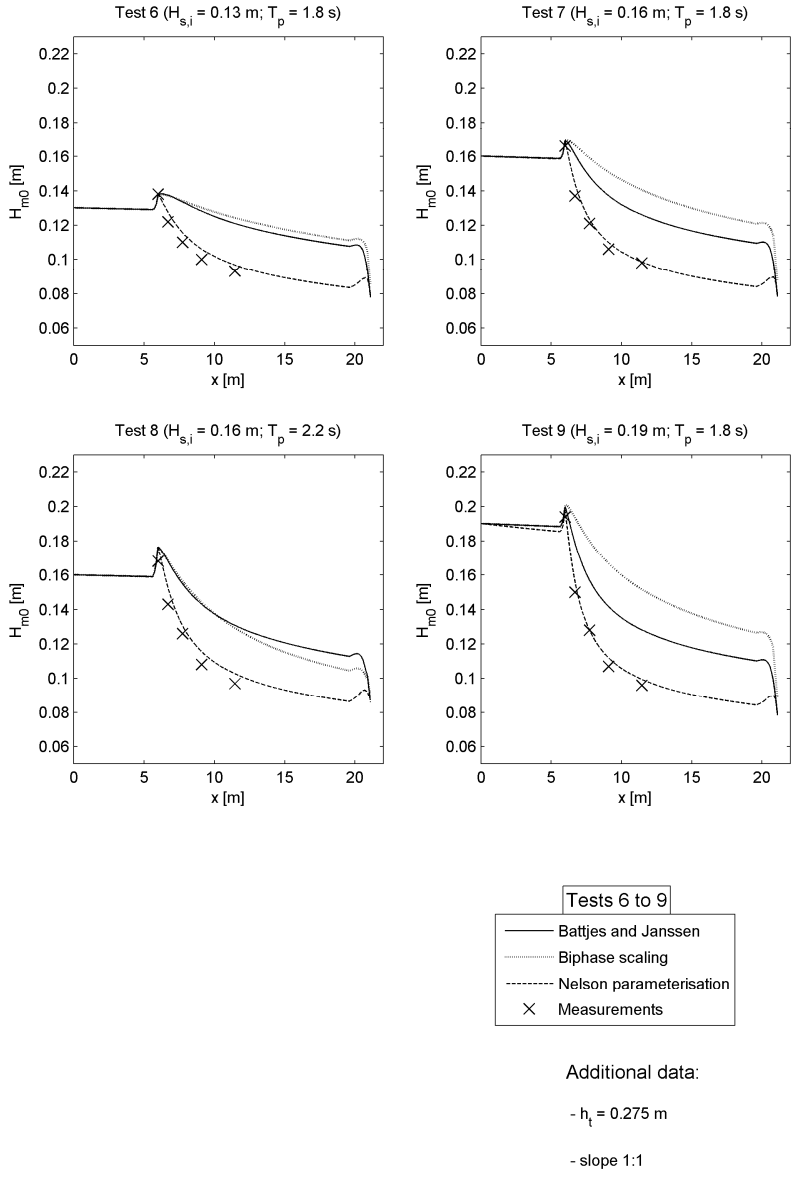
Test 6 ($H_{s,i}$ = 0.13 m; T_p = 1.8 s)
Test 7 ($H_{s,i}$ = 0.16 m; T_p = 1.8 s)
Test 8 ($H_{s,i}$ = 0.16 m; T_p = 2.2 s)
Test 9 ($H_{s,i}$ = 0.19 m; T_p = 1.8 s)
H_{m0} [m]
x [m]
Tests 6 to 9
Battjes and Janssen
Biphase scaling
Nelson parameterisation
Measurements
Additional data:
- h_t = 0.275 m
- slope 1:1

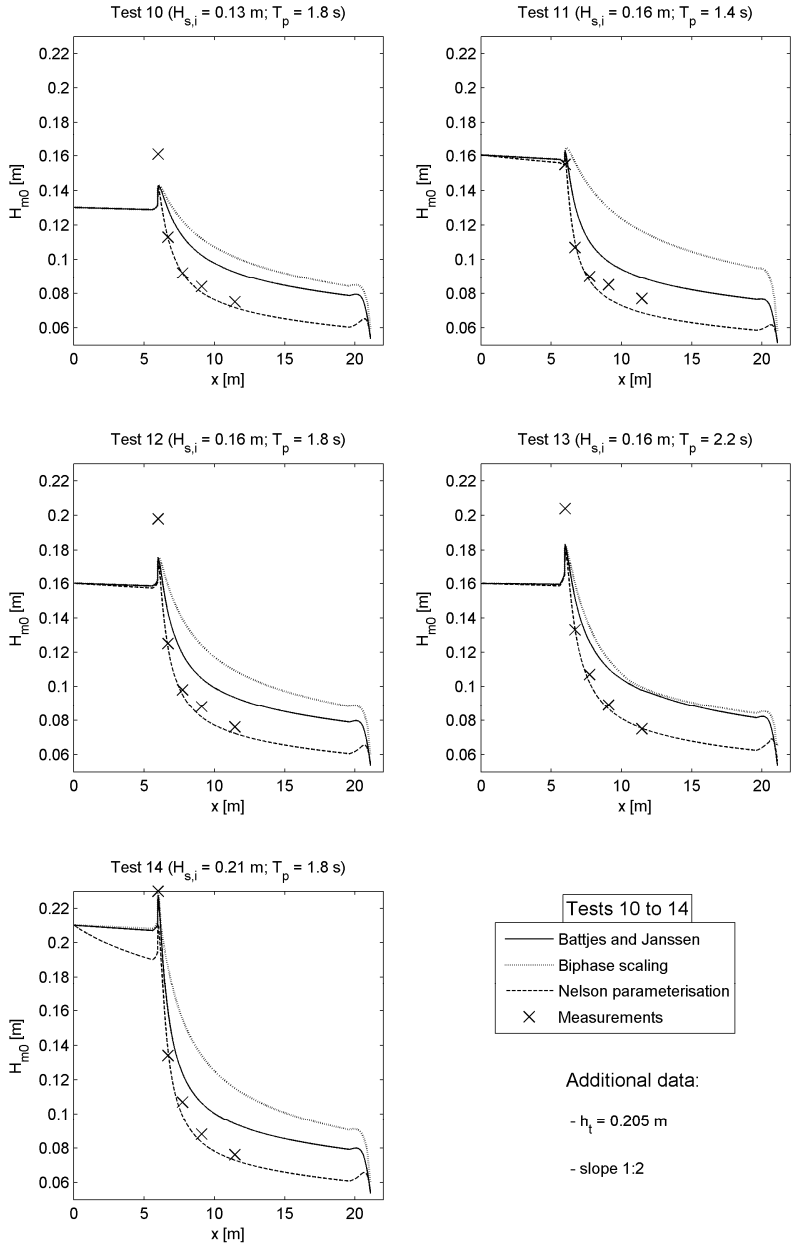
Test 10 ($H_{s,i}$ = 0.13 m; T_p = 1.8 s)
Test 11 ($H_{s,i}$ = 0.16 m; T_p = 1.4 s)
Test 12 ($H_{s,i}$ = 0.16 m; T_p = 1.8 s)
Test 13 ($H_{s,i}$ = 0.16 m; T_p = 2.2 s)
Test 14 ($H_{s,i}$ = 0.21 m; T_p = 1.8 s)
H_{m0} [m]
x [m]
Tests 10 to 14
Battjes and Janssen
Biphase scaling
Nelson parameterisation
Measurements
Additional data:
- h_t = 0.205 m
- slope 1:2

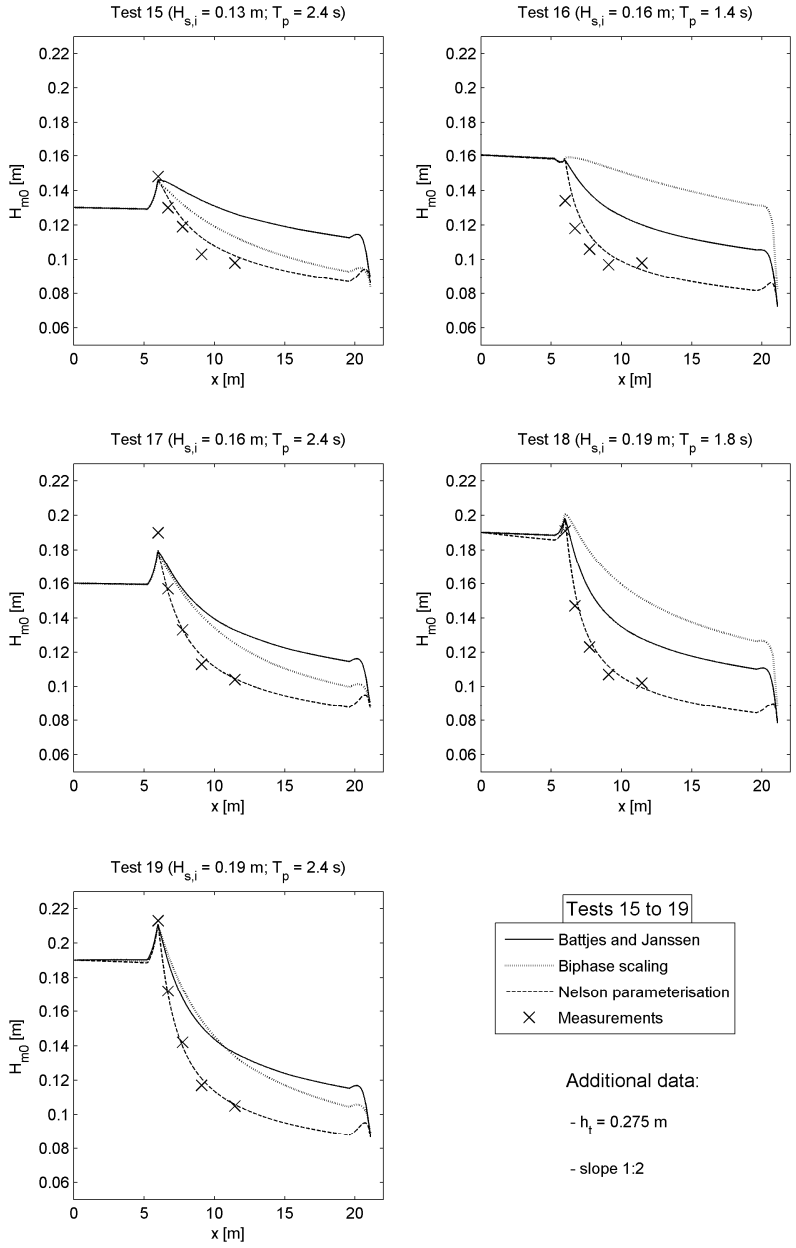
Test 15 ($H_{s,i}$ = 0.13 m; T_p = 2.4 s)
Test 16 ($H_{s,i}$ = 0.16 m; T_p = 1.4 s)
Test 17 ($H_{s,i}$ = 0.16 m; T_p = 2.4 s)
Test 18 ($H_{s,i}$ = 0.19 m; T_p = 1.8 s)
Test 19 ($H_{s,i}$ = 0.19 m; T_p = 2.4 s)
H_{m0} [m]
x [m]
Tests 15 to 19
Battjes and Janssen
Biphase scaling
Nelson parameterisation
Measurements
Additional data:
- h_t = 0.275 m
- slope 1:2

5 Appendix E – Input file part I

In this appendix an input file is given that was used for the calculations on part I: On the time scales of wave processes.

```
$********************HEADING*****************************
PROJ 'azg' 'azg'

$********************MODEL INPUT*************************
SET MAXERR = 3 NAUT
CGRID CURVI 285 411  EXC -99.00  CIRCLE  36  0.03 1 37
READ  COOR  1. 'inputs\azg3a.grd'  IDLA=3 NHEDF=3 FORMAT '(10X,5F12.3)'
INP  BOTTOM CURVI 0. 0. 285 411  EXC -99.0
READ BOTTOM 1. 'inputs\azg3a.bot'  IDLA=3 NHEDF=0 FREE
INP  WLEV  CURVI  0. 0. 285 411  EXC -99.0
READ WLEV  1. 'inputs\azg3a_20040208_2000.lev' IDLA=1 NHEDF=0 FREE
INP  CUR  CURVI  0. 0. 285 411  EXC -99.0
READ CUR  1. 'inputs\azg3a_20040208_2000.cur' IDLA=1 NHEDF=0 FREE

$********************BOUNDARY CONDITIONS*****************
BOUNDNEST1 NEST 'inputs\azg3a_20081705_0500_hc0.sp2'  OPEN

$********************PHYSICA*****************************
WIND 15 0
GEN3 WESTH
QUAD
TRIAD trfac=0.05
BREAKING 1 0.73
FRICTION JONSWAP CFJON=0.067
$********************NUMERIEKE PARAMETERS****************
NUM STOPC 0.00 0.01 0.001 101 STAT mxitst=30 alfa=0.01

$********************DEFINITIE VAN UITVOERPUNTEN*********

$********************OUTPUT******************************
FRAME 'myframe' 130000 575000 0 60000 45000 1000 1000
$********************SP2 Nest UITVOER********************
$************************BLOCK UITVOER********************
BLOCK 'myframe' NOHEAD 'azg.mat' LAY 3 XP YP HS RTM01 GENW REDQ REDT DISW
DISB DISSU PROPX PROPT PROPS RADSTR
BLOCK 'myframe' NOHEAD 'default.mat' LAY 3 XP YP BOTLEV HS RTM01 VEL DIR
WLEN DEPTH UBOT URMS HSWELL TM01
BLOCK 'myframe' NOHEAD 'Wave_characteristics.mat' LAY 3 XP YP STEEPNESS
FORCE QB
BLOCK 'myframe' NOHEAD 'Dissip.mat' LAY 3 XP YP DISSIP DISBOT DISSURF
DISWCAP

COMPUTE
STOP
```

6 Appendix F – Input file part II

In this appendix an input file for test 1 from the Jensen (2002) test case is given that was used for the calculations on part II: Depth-induced breaking: A comparison of the performance of three models. This input file describes the Nelson parameterisation. For the other test cases the input files look very similar.

```
$*************HEADING*********************************
$                            TEST 1
$
PROJ 'MSJ' 'MSJ'
$
$
$********** MODEL INPUT ******************************
$
MODE STAT ONED
$
CGRID REG 0. 0. 0. 22.6 0. 2259 0 SECTOR -10 10 40 0.25 2.00 30
$
INPGRID BOTTOM 0. 0. 0. 2259 0 0.01 1.
READINP BOTTOM 1. 'MSJ11_0205.bot' 1 1 FREE
$

$
BOUN SHAPE JON PEAK DSPR POWER
BOUN SIDE W CCW CON PAR 0.13 1.8 0.0 500
$
$************ Physics ********************************
OFF QUAD
BREaking VAR 1.0 0.55 0.81 0.73 0.88 0.012
FRIC JONSWAP 0.067
TRIAD 0.05
$************ NUMERIC PARAMETERS *********************
NUM STOPC 0.00 0.01 0.001 99.5 STAT mxitst=100 alfa=0.01
$
$************ OUTPUT REQUESTS ************************
$
QUANT   XP HEXP 10.
$
$POINTS 'MSJ' FILE 'MSJ11_0205.loc'
POINTS 'MSJ' FILE 'MSJ11_0205_HS.loc'
$TABLE 'MSJ' HEAD 'MSJ11_Test1.tbl'   XP DEP HS RTP TM01 TM02 FSPR DIR
TABLE 'MSJ' HEAD 'MSJ11_Test1.tab'   XP DEP HS RTP TM01 TM02 FSPR DIR
TABLE 'MSJ' HEAD 'MSJ11_Test1_HS.mat'   XP HS REDTRIAD DISBOT DISSURF

TEST 1,0
COMPUTE
STOP
```

7 Appendix G – A.J. v. der Westhuysen